Universitat Autònoma de Barcelona

Measurement of Z/γ^* + jets differential cross sections with the CDF detector at $\sqrt{s} = 1.96$ TeV [1]

Stefano Camarda

Supervised by
Dr. Veronica Sorin

Tutor
Prof. Mario Martínez Pérez
(ICREA/IFAE - UAB)

Universitat Autonoma de Barcelona
Facultat de Ciències
Departament de Física

IFAE - Institut de Física d'Altes Energies
July 2012

---

[1] Ph.D. dissertation

al ricordo di Alberto

Contents

Introduction

Experimental and theoretical effort of understanding the Z/γ^* + jets final state has a double reason, on one hand the motivation is to test the ability of the Standard Model theory of particle physics to make accurate predictions when electroweak and QCD physics are involved at different scales, ranging from the non perturbative evolution of hadrons to perturbative QCD and electroweak calculations at a scale $\mu \gtrsim M_Z$. On the other hand a precise modeling of Z/γ^* + jets processes is a fundamental prerequisite in the search for new physics in final states with jets and leptons or missing transverse energy. In addition the $Z/\gamma^* \to l^+l^-$ + jet final state is appropriate to calibrate jet reconstruction and reduce the experimental uncertainties related to the jet energy scale. In response to a widespread interest in jets production associated to vector bosons, many of the recently developed perturbative QCD calculations and Monte Carlo tools include Z/γ^* and W + jets production at hadron colliders [1] [2]. The approximately 10 fb^{-1} of integrated luminosity collected with the CDF detector in Tevatron Run II allows for precise measurement of inclusive and differential cross sections of Z/γ^* + jets production, and opens the possibility of testing the accuracy of state of the art theoretical predictions. Z/γ^* + jets cross sections are measured independently in the $Z/\gamma^* \to e^+e^-$ and $Z/\gamma^* \to \mu^+\mu^-$ decay channels and combined to achieve the best experimental precision. The results presented in this thesis provides an experimental feedback to the recent development in theoretical calculations and validate the new predictions through a comparison with the measured cross sections. The comparison includes a careful study of the uncertainties associated to the theoretical models, and sensible variations of parameters and settings of the predictions.

In Chapter 1 the QCD theoretical framework is briefly reviewed in the context of predictions at hadron colliders, Chapter 2 describes the Monte Carlo programs and the theoretical models used to evaluate the Z/γ^* + jets predictions. Chapter 3 is devoted to the description of the Tevatron accelerator complex and of the CDF detector. Chapter 4 describes the analysis techniques employed to measure the Z/γ^* + jets differential cross sections and in Chapter 5 a detailed comparison between measured cross sections and theoretical predictions is discussed. Chapter 6 summarizes the main results and presents conclusions.

Chapter 1

QCD Theory

Quantum Chromodynamics, QCD, is the field theory that describes the strong interactions between quarks and gluons. QCD is part of the Standard Model of particle physics, which successfully describes the measurements of high energy collider experiments. Recent reviews of QCD in the context of predictions of production rates at hadron colliders are given in [3] and [4].

1.1 Standard Model and QCD Lagrangian

The Standard Model describes the electromagnetic, weak and strong interactions in a quantum field theory based on group symmetries. It is based on the group $\mathrm{SU}(3)_\mathrm{C} \times \mathrm{SU}(2)_\mathrm{L} \times \mathrm{U}(1)_\mathrm{Y}$, where $\mathrm{SU}(3)_\mathrm{C}$ describes the strong interaction, and $\mathrm{SU}(2)_\mathrm{L} \times \mathrm{U}(1)_\mathrm{Y}$ the electromagnetic and weak interactions. These forces are mediated by carrier particles which have integer spin, obey Bose-Einstein statistics and are called gauge bosons. The electromagnetic force is mediated via the exchange of massless photons, γ, the weak force is transmitted by exchange of three massive intermediate vector bosons, the $W^\pm$ and Z, and the strong force is mediated via eight massless gluons. Table 1.1 summarizes the Standard Model forces and the carrier bosons.

Interaction	Carrier boson	Mass
Strong	gluon	0
Electromagnetic	photon	0
Weak	$W^\pm$	80.4 GeV/c^2
	Z^0	91.2 GeV/c^2

Table 1.1: Standard Model interactions and mediators.

Besides gauge bosons, the Standard Model comprises a second type of fundamental particle, which have half-integer spin and are called fermions. They follow Fermi-Dirac statistics and are constrained by the Pauli exclusion principle. There are two fundamentally different types of fermions: leptons and quarks. They both interact electroweakly, but only quarks interact through the strong force. The lepton category consists of electrons (e), muons (μ) and taus (τ) and their associated neutrinos, (ν_e), (ν_μ) and (ν_τ), respectively. There are six massive quarks, or flavours: up (u), down (d), charm (c), strange (s), top (t) and bottom (b). Out of the six quarks three of them (u,c,t) have electric charge $Q = +2/3$

Quarks			charge
$\begin{pmatrix} u \\ d \end{pmatrix}$	$\begin{pmatrix} c \\ s \end{pmatrix}$	$\begin{pmatrix} t \\ b \end{pmatrix}$	$+2/3$ $-1/3$
Leptons			charge
$\begin{pmatrix} e \\ \nu_e \end{pmatrix}$	$\begin{pmatrix} \mu \\ \nu_\mu \end{pmatrix}$	$\begin{pmatrix} \tau \\ \nu_\tau \end{pmatrix}$	-1 0

Table 1.2: Quark and lepton families in the Standard Model.

and are also known as up-type quarks. The other three quarks (d,s,b) are down-type and carry electric charge $Q = -1/3$. Quarks and leptons can be associated in three sets as shown in Table 1.2, each set is called a generation, or family.

QCD is the part of the Standard Model that describes the strong interaction of quarks and gluons, it was developed in 1973 [5] in the context of a Quantum Field Theory based on the SU(3) symmetry group [6]. It is a non-abelian theory whose Lagrangian is given by:

$$\mathcal{L}_{QCD} = -\frac{1}{4} F^A_{\mu\nu} F^{\mu\nu}_A + \sum_j^{\text{flavours}} \bar{q}_j (i\gamma^\mu D_\mu - m_j) q_j \tag{1.1}$$

$$F^A_{\mu\nu} = \partial_\mu \mathcal{A}^A_\nu - \partial_\nu \mathcal{A}^A_\mu - g f^{ABC} \mathcal{A}^B_\mu \mathcal{A}^C_\nu \tag{1.2}$$

$$D_\mu = \partial_\mu + ig A^\alpha_\mu t^\alpha \tag{1.3}$$

where the index j runs over the six different quark flavours, $F^A_{\mu\nu}$ is the field strength tensor derived from the gluon field $\mathcal{A}^A_\alpha$ and D_μ is the covariant derivative. The indices A, B, C run over the eight colour degrees of freedom of the gluon field, g is the strong coupling constant, which determines the strength of the interaction between coloured particles, t^α are the Gell-Mann matrices and f^{ABC} are the structure constants of the SU(3) colour group.

The term $g f^{ABC} \mathcal{A}^B_\mu \mathcal{A}^C_\nu$ in equation 1.2 is characteristic of the non-abelian nature of QCD, it determines the property of the interaction between gluons, resulting in a very different behavior of the strong interaction compared to the electromagnetic interaction. In fact, while $gq\bar{q}$ vertices, coming from the interaction of the gluon field with the quark fields are analogous to the $\gamma f \bar{f}$ coupling in Quantum Electrodynamics, 3-gluon and 4-gluon vertices arising from the self-interaction of the gluon field are a distinctive feature of the non-abelian nature of QCD. Self-interaction of the gluon field leads to two important characteristics of the strong interaction: asymptotic freedom and confinement.

As in Quantum Electrodynamics diagrams involving internal loops are associated with ultraviolet divergences, and in order to handle such divergences a renormalization scale μ is introduced. As a consequence the strong coupling constant $\alpha_s = \frac{g^2}{4\pi}$ depends on the renormalization scale μ which in turn is related to the physical scale Q of the involved process. The running of α_s is shown in Figure 1.1, taken from [7].

At high values of μ $\alpha_s(\mu)$ decreases, strong interactions proceed via colour fields of reduced strength and quarks and gluons behave as essentially free particles. This property is called asymptotic freedom, and is a prerequisite for the perturbative approach to QCD calculations. On the other hand the coupling strength asymptotically diverges at low values of μ and makes impossible the observation of isolated quarks: when in a bound state of quarks a quark begins to separate, the energy of the field increases, until at some point it is energetically favorable to create an additional $q\bar{q}$ pair which neutralizes the colour

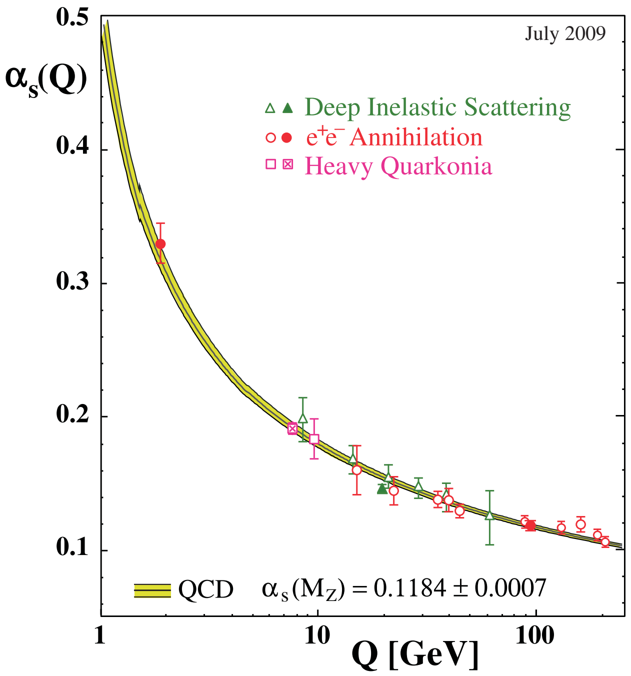

Figure 1.1: Values of the QCD coupling α_s as a function of the scale Q.

charge. Only colourless bound states, called hadrons, can be observed, such property is called confinement and is related to the process of hadronization.

1.2 QCD factorization

Deep inelastic scattering experiments played an important role in the development of QCD theory, and led to the quark "parton model". In such model nucleons are considered as bound states of three partons, each carrying a fraction x_p of the total nucleon momentum such that

$$\sum_{\text{partons}} x_p = 1 \tag{1.4}$$

In the parton model, the total cross section of a scattering involving hadrons can be expressed in terms of a partonic interaction cross section convoluted with a parton density f, also called parton distribution function or PDF. For each type of parton, a function $f_i(x)$ of the momentum fraction x represents the probability of finding inside the nucleon a parton of type i carrying a fraction x of the nucleon momentum. The concept of partonic densities of the proton is essential in QCD theory to make predictions of production rates when hadrons are present in the initial state of a scattering process. Another essential ingredient of any cross section calculation in hadron collisions is the concept of QCD factorization. The QCD factorization theorem states that a cross section can be factorized into short and long distance components delimited by a factorization scale μ_F, where the long-distance physics is included in the parton distribution functions. The factorization scale μ_F is introduced to absorb the infrared divergences that appear in the soft and collinear limit, in analogy to the introduction of the renormalization scale μ_R needed to absorb the ultraviolet divergences. According to the factorization theorem the cross section for the production of a final state X in the hard scattering initiated by a proton and an anti-proton with four-momenta P_1 and P_2 and center-of-mass energy $s = (P_1 + P_2)^2$ can be written as:

$$\sigma_{p\bar{p}\to X} = \sum_{i,j} \int dx_1 dx_2 f_i^p(x_1, \mu_F) f_j^{\bar{p}}(x_2, \mu_F) \times \hat{\sigma}_{ij\to X}(x_1, x_2, s, \alpha_s(\mu_R)) \tag{1.5}$$

where $f_i^{p,\bar{p}}$ are the PDF for the proton and the anti-proton, the indexes i, j runs over all parton types, and $\hat{\sigma}_{ij\to X}$ is the parton cross section for incoming partons with momenta $p_1 = x_1 P_1$ and $p_2 = x_2 P_2$. The perturbative expansion of $\hat{\sigma}_{i,j}$ can be calculated only up to a given finite order in α_s, introducing an unphysical dependence on the renormalization scale μ_R which is related to the uncertainty of neglecting higher order terms. The addition of such higher order terms in the perturbative expansions of α_s reduces the dependence of the cross section on the choice of the renormalization scale. Another possibility to reduce the dependence of the cross section on μ_R and the related uncertainty is to set μ_R on an event by event basis, choosing a functional form which reflects the physical scale Q of the process. Studies on the appropriate choice of the renormalization scale for W/Z + jets processes have been performed in [8] and [9] [10]. The factorization scale μ_F is usually set equal to the renormalization scale μ_R.

1.3 Parton distribution functions

Perturbative QCD does not predict the form of the PDF, but can describe their evolution with the variation of the scale Q^2. The parton interactions at the lowest order in α_s are four parton branching processes: quark splitting into a quark through gluon radiation ($q \to qg$), gluon splitting into a gluon ($g \to gg$) gluon splitting into a quark ($g \to q\bar{q}$) and quark splitting into a gluon ($q \to gq$). In the soft and collinear limit, where the opening angle between the outgoing partons is small, and averaging over the polarizations and spins, these processes are described by the splitting functions:

$$P_{qq}(z) = \frac{4}{3}\left[\frac{1+z^2}{1-z}\right] \tag{1.6}$$

$$P_{gg}(z) = 6\left[\frac{1-z}{z} + \frac{z}{1-z} + z(1-z)\right] \tag{1.7}$$

$$P_{gq}(z) = \frac{4}{3}\left[\frac{1+(1-z)^2}{z}\right] \tag{1.8}$$

$$P_{qg}(z) = \frac{1}{2}[z^2 + (1-z)^2] \tag{1.9}$$

where P_{ab} represents the probability that a parton of type b radiates and becomes a parton of type a, and z is the fraction of momentum carried by the parton after the splitting. The P_{qq} and P_{gg} splitting functions are divergent in the soft limit ($z \to 1$). The integration of the splitting functions over the opening angle between partons diverges in the collinear limit, the introduction of an arbitrary factorization scale μ_F is needed to absorb such collinear divergences into the PDF itself. The evolution of the quarks PDF $q(x, \mu_F^2)$ and gluons PDF $g(x,\mu_F^2)$ as a function of the factorization scale μ_F can be written in terms of the splitting functions:

$$\frac{dq(x,\mu_F^2)}{d\ln\mu_F^2} = \frac{\alpha_s}{2\pi}\int_x^1 \frac{dz}{z}\left[P_{qq}(z)q(x/z,\mu_F^2) + P_{gq}(z)g(x/z,\mu_F^2)\right] \tag{1.10}$$

$$\frac{dg(x,\mu_F^2)}{d\ln\mu_F^2} = \frac{\alpha_s}{2\pi}\int_x^1 \frac{dz}{z}\left[P_{gg}(z)g(x/z,\mu_F^2) + P_{qg}(z)g(x/z,\mu_F^2)\right] \tag{1.11}$$

where x is the momentum fraction of the parton entering the hard scattering. These equations are called the DGLAP equations after Dokshitzer, Gribov, Lipatov, Altarelli and Parisi [11].

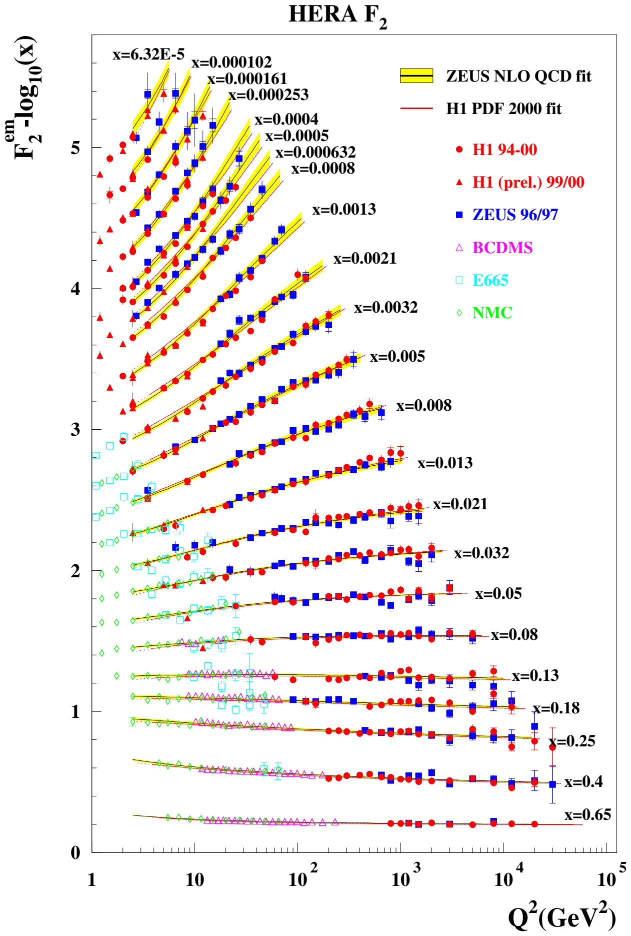

Figure 1.2: Structure function F_2 as a function of Q^2 and x measured in DIS experiments and compared to the global fit performed by the ZEUS collaboration.

Parton distribution functions are determined from fits to experimental data, DIS experiments provide direct constraints on the quark PDF, and through the observed evolution of quark at different scale and DGLAP evolution also indirect constraints on the gluon PDF.

In fact PDFs are directly related to the structure function of the proton F_2, a quantity that can be measured in DIS experiments and that can be expressed at zeroth order in α_s as:

$$F_2^{em} = x \sum_{i=q,\bar{q}} e_i^2 f_i^p(x) \tag{1.12}$$

Figure 1.2 shows the comparison between the fit from the ZEUS collaboration of the structure function F_2 of the proton as a function of x and Q^2 and DIS data.

1.4 QCD predictions

Different and complementary methods can be used to perform quantitative predictions in QCD. Fixed order calculations and parton showers Monte Carlo are commonly employed to evaluate predictions which can be compared to measured cross sections at hadron colliders. A different approach consists in the analytical resummation of the perturbative series, predictions based on resummation methods have not been compared to the measured cross sections presented in this thesis. Several techniques which combine the fixed order and parton shower methods have been developed, such techniques and the Monte Carlo programs used to perform predictions for the Z/γ^* + jets cross sections are reviewed in Chapter 2. Theoretical predictions need also to account for non-perturbative QCD effects such as hadronization and underlying event, which are characterized by a low scale $Q \lesssim 1$ GeV at which a perturbative calculation is not possible.

1.4.1 Perturbative QCD fixed order calculations

Conceptually the most simple way to calculate the cross section of a given process is to perform a fixed order expansion in α_s of the partonic cross sections $\hat{\sigma}_{i,j}$ of equation 1.5. As far as only the first terms are evaluated and the number of final state particles is limited calculations are actually feasible, but the numerical complexity grows up rapidly with the number of particles, and additional difficulties come from the exact subtraction of divergences associated to higher order terms of the perturbative expansion. The production of Z/γ^* + jets offers a good opportunity to test such perturbative QCD predictions: the presence of a boson with a large mass and high p_T jets provide a hard enough scale Q to make perturbative calculations possible. In the case of the production of Z/γ^* + 1 jet the leading order (LO) diagrams include the processes $q\bar{q} \to Zg$, $qg \to Zq$ and $\bar{q}g \to Z\bar{q}$, as shown in Figure 1.3.

Next-to-leading order (NLO) corrections to the LO cross section require the addition of 1-loop Z/γ^* + 1 parton diagrams and tree-level diagrams of Z/γ^* + 2 partons. A great complication of NLO (and beyond) calculations is the exact cancellation of the divergences associated to loop diagrams and the corresponding infrared divergences of real radiation diagrams. The problem is solved applying "subtraction" methods based on the addition of counter-terms which make the integration of the real and virtual part finite.

1.4.2 Parton shower Monte Carlo programs

A different approach to solve the issues related to the divergences which arise in the soft and collinear limits is represented by parton shower Monte Carlo programs [12]. The idea is to start from a simple process $2 \to n$ with low particle multiplicity in the final state, and iteratively perform the parton branchings $q \to qg$, $g \to gg$ and $g \to q\bar{q}$ in order to obtain

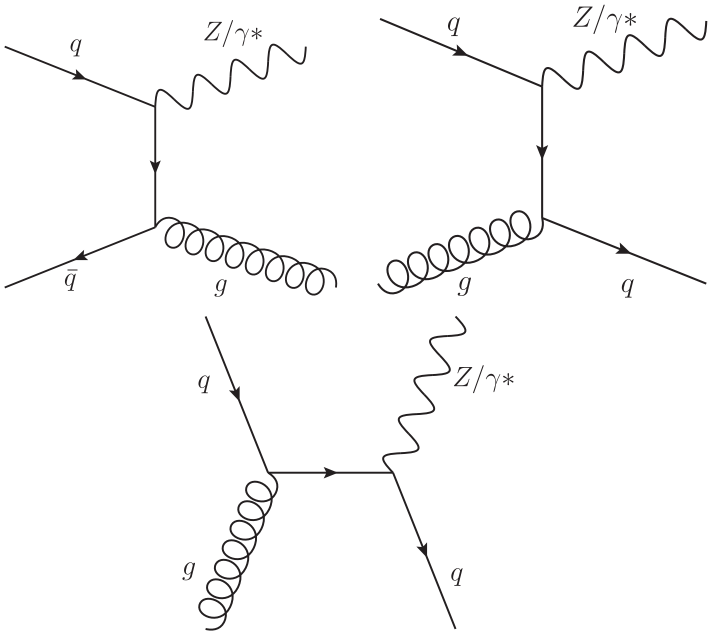

Figure 1.3: Leading order Feynman diagrams for Z/γ^* + 1 jet production.

a larger multiplicity in the final state. Branching probabilities are evaluated according to equations 1.9, and cancellation between real and virtual divergences are handled through the introduction of a Sudakov form factor:

$$\Delta(k_T, Q) \simeq \exp\left[-\frac{2\alpha_s C_F}{\pi}\int^{Q}\frac{dE}{E}\int^{\pi/2}\frac{d\theta}{\theta}\Theta(E\theta - k_T)\right] \tag{1.13}$$

which represents the probability of not having emission above the transverse momentum scale k_T and ensures that the total probability for a parton to branch never exceeds unity. Iterative branchings are performed until a lower cutoff scale $Q_0 \sim 1$ GeV is reached, at which the parton shower is stopped. Monte Carlo programs distinguish between initial-state and final-state showers, depending on whether showers are originated from an incoming or outgoing parton of the hard scattering; corresponding radiation is referred as initial-state radiation or ISR and final-state radiation or FSR.

1.4.3 Hadronization

The transition between partons and hadrons is described by hadronization models involving a number of non-perturbative parameters which needs to be tuned on experimental data. Commonly used hadronization models are the string model and the cluster model, a schematic representation of the two taken from [13] is shown in Figure 1.4. The string model uses colour strings which produce a linear confinement potential. As partons separate from each other, the string breaks into shorter strings creating colourless states. If the relative momentum of the new string is large enough, the string may break again. In the cluster model all the gluons in the final state are split into $q\bar{q}$ pairs, and quarks are then grouped in colourless clusters, which then decay into hadrons.

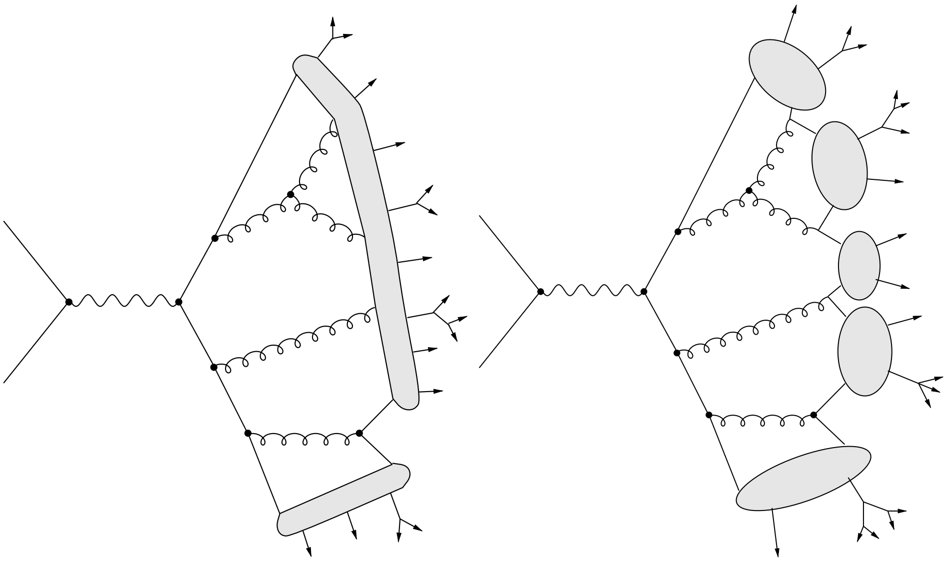

Figure 1.4: Schematic view of string (left) and cluster (right) hadronization models.

1.4.4 Underlying event

QCD predictions at hadron colliders need to include the simulation of the underlying event activity caused by additional interactions between partons not involved in the “primary” hard scattering. Such an effect is also referred to as multi-parton interactions, and is modeled adding multiple 2 → 2 parton processes. Underlying event processes occur at a low momentum scale, and need the introduction of non-perturbative parameters which are tuned to properly model experimental data.

1.5 Jet algorithms

Quarks and gluons originated in hadron collisions are not directly detectable, as soon as they are produced their divergent branching probabilities and QCD confinement makes them fragment and hadronize into jets of collimated hadrons. Jet algorithms provide a way of associating particles into jets: given a list of four-vectors that can be either detector calorimeter towers, stable particles in the final state of a Monte Carlo generated event, or partons in a fixed order perturbative QCD prediction, a jet algorithm combines the particles four-momenta into jets following a set of reconstruction rules. A recombination scheme defines how particles four-momenta are recombined to evaluate the jet four-momenta, and most jet algorithms also include a radius parameter R which is related to the opening angle of the jet. Jet algorithms are classified into cone and sequential recombination algorithms, a detailed review of jet reconstruction at hadron colliders is given in [14].

1.5.1 Cone jet algorithms

Cone algorithms are based on the idea of associating particles within a cone of a given radius R in rapidity y and azimuthal ϕ coordinates. Most cone algorithms belong to the iterative cones (IC) category. In such algorithms a subset of particles called seeds is used to set the initial directions of jets; all the particles within a cone of radius R in $y - \phi$ around a seed are associated to a jet, and the particles four-momenta are recombined to evaluate the jets directions which are used as seeds for the next iteration. The procedure stops when the resulting directions are stable. In contrast with IC algorithms, fixed cone (FC) algorithms do not iterate the cone direction, but rather associate particles to a jet in a fixed cone around a given seed. Jets reconstructed with IC or FC procedure can have particles in common, to avoid particles being associated to more than one jet three different methods have been followed. In the progressive removal (PR) approach initial seeds are ordered in E_T, and starting from the hardest seed, particles associated to a jet are removed from the list of available particles. Another approach is to apply a split-merge (SM) procedure to the list of stable jets, if the fraction of energy shared by two jets is higher than an overlap threshold f, typically set to 0.5 or 0.75, the two jets are merged in a single larger jet, otherwise particles are assigned to the closest jet. An alternative is a split-drop (SD) procedure in which the non-shared particles that belongs to the softer of the two jets are simply dropped and not clustered in any jet. The use of seeds in both IC and FC algorithms gives rise to infra-red and collinear safety issues, infact collinear splitting and soft radiation can change the number of initial seeds and as a consequence the set of final jets after the SM, SD or PR procedure. A partial workaround applied to IC-SM algorithms is to perform a further iteration introducing additional seeds evaluated in the “midpoints” of all stable cones, algorithms implementing this procedure are referred as midpoint jet algorithms. With such modification infra-red safety is assured for configurations with 2 hard particles in a common neighbourhood plus a soft one, but issues reappears in configurations with 3 hard particles plus a soft one. A full solution to infra-red and collinear safety problems is to avoid seeds and iterations, and find all stable cones through some exact procedure. This type of algorithm is referred as seedless-cone (SC), and the recent development of an efficient computational strategy in the SISCone implementation [15] made them usable also in events with a high number of particles.

1.5.2 Sequential recombination jet algorithms

A different category of jet algorithms is based on the sequential recombination (SR) of particles. Sequential recombination involves the definition of a distance between particles, pairs of particles are then recombined in order of increasing distances. Several variants of sequential recombination algorithms have been used, at hadron colliders the most widely used versions belong to the class of the longitudinally invariant generalized k_t algorithm. Longitudinally invariant distances d_{ij} between particles and d_{iB} between a particle and the beam are defined as:

$$d_{ij} = \min(p_{ti}^{2p}, p_{tj}^{2p}) \frac{\Delta R_{ij}^2}{R^2} \qquad \Delta R_{ij}^2 = (y_i - y_j)^2 + (\phi_i - \phi_j)^2 \tag{1.14}$$

$$d_{iB} = p_{ti}^{2p} \tag{1.15}$$

The parameter R is called jet-radius, and plays a role similar to that of the parameter R in a cone algorithm. The parameters p determines the type of the algorithm: $p = 1$ corresponds to the k_t algorithm, $p = 0$ to the Cambridge/Aachen and $p = -1$ to anti-k_t. In the commonly used inclusive variant of the algorithms the minimum distance between all the d_{ij} and d_{iB} is found, if it is a d_{ij} particles i and j are recombined and considered as a single particle in the next iteration, if it is a d_{iB} particle i is considered as a jet and removed from the list of particles. The procedure is repeated until no particles are left.

In the exclusive variant when the minimum distance is a d_{iB} particle i is assigned to the beam and removed, and the clustering stops when all the distances d_{ij} d_{iB} are above some threshold d_{cut}. Sequential recombination algorithms have the advantage of being infra-red and collinear safe, and generally less sensitive to hadronization than cone algorithms.

Chapter 2

Z/γ^* + jets theoretical predictions

Several Monte Carlo programs are used and combined in order to evaluate theoretical predictions of the $Z/\gamma^* \to l^+l^-$ + jets production cross section. MCFM v6.0 and BLACKHAT+SHERPA are employed to evaluate fixed order perturbative QCD calculation at LO and NLO, PYTHIA v6.4.26 Monte Carlo is used to perform parton showering and hadronization, POWHEG v1.0 performs a NLO calculation suitable to be showered, ALPGEN v2.14 matches LO perturbative QCD predictions at different jet multiplicities with parton showers, and LOOPSIM interfaced to MCFM v5.8 is used to combine fixed order NLO perturbative QCD calculations at different jet multiplicities and simulates higher order loop corrections to get an approximate $\bar{\text{n}}$NLO perturbative QCD prediction. The ALPGEN generator interfaced to PYTHIA parton shower is also used to perform the unfolding of the measured cross sections as described in section 4.6, and to evaluate the non perturbative QCD corrections which need to be applied to perturbative QCD calculation as discussed in section 5.1. NLO electroweak corrections to the Z/γ^* + jets cross section were calculated in [17], and have been recently implemented in a Monte Carlo code which is able to evaluate them for arbitrary cuts on lepton p_T and Z/γ^* invariant mass [18].

2.1 NLO perturbative QCD calculations - MCFM and BLACKHAT

The NLO perturbative QCD predictions are obtained with three different programs: MCFM, BLACKHAT and POWHEG. MCFM can perform perturbative QCD calculation at NLO for Z/γ^* + 1 jet and 2 jets final states, and is the first program which performed the NLO calculation for the Z/γ^* + 2 jets process [19]. The real corrections are incorporated in MCFM using the Catani-Seymour dipole subtraction with the method of Ellis, Ross and Terrano, which consists in creating subtraction counter-terms having the same singularity structure as the real emission matrix elements, but simple enough that they can be integrated over the phase space of the unobserved parton. MCFM NLO predictions were already compared to the CDF measured cross sections in [20], and to the D0 measurement in [21]. Recent developments in multi-leg perturbative QCD calculations opened the possibility of evaluating W/Z vector boson plus jets NLO predictions at higher jet multiplicity. Nowadays BLACKHAT in conjunction with SHERPA can be used to calculate

NLO cross sections for events with a Z/γ^* plus 1, 2, 3 and 4 jets [10] [22], even if the Z/γ^* + 4 jets prediction is currently available only for the LHC. The BLACKHAT library is used to evaluate the virtual contributions, employing the unitary method described in [23]. The real emission corrections are calculated with SHERPA, and the infrared singularities are canceled between real-emission and virtual contribution using the Catani-Seymour dipole subtraction method implemented in the AMEGIC++ program which is part of the SHERPA framework [24].

2.2 Approximate n̄NLO prediction - LOOPSIM

Several on-going efforts to improve the accuracy of Z/γ^* + jets theoretical prediction focus on beyond NLO QCD corrections. Although much progress have been made recently in NNLO perturbative QCD calculation of 2 to 2 scattering process in the context of the antenna subtraction method [25], NNLO predictions are not yet available for the Z/γ^* + jet final state at hadron colliders. Recently, threshold resummation for W and Z production at large p_T have been performed at next-to-next-to-leading logarithmic accuracy, including matching to next-to-leading fixed-order results [26]. To allow the comparison of this prediction with the $Z/\gamma^* \to l^+l^-$ + jets measured cross sections, differential calculation in the lepton and jet momenta are still needed to account for the experimental cuts. Another approach to resummation which provides an approximate NNLO prediction of high p_T vector boson production has been presented in [27].

A currently available theoretical calculation including beyond NLO QCD corrections is the LOOPSIM+MCFM prediction. The LOOPSIM method allows to combine Z/γ^* + 1 jet and Z/γ^* + 2 jets NLO perturbative QCD calculations and simulate the missing NNLO double-virtual contributions in order to obtain an approximate n̄NLO prediction [28]. The notation n̄NLO denotes an approximation of NNLO where the double-loop terms are estimated through the LOOPSIM procedure. The method was developed in the context of observables with giant NLO-LO K-factor, in fact such observables are expected to have significant beyond NLO corrections. The LOOPSIM method has been checked against the NNLO prediction of the Z/γ^* inclusive cross section, where it gives very reasonable results. In this thesis the Z/γ^* + $\geqslant$1 jet prediction evaluated with the LOOPSIM method is compared for the first time to experimental measurements. If applied to the Z/γ^* + $\geqslant$ 1, 2, 3 and 4 jets NLO BLACKHAT+SHERPA predictions the LOOPSIM method could provide Z/γ^* + $\geqslant$ 2 and 3 jets n̄NLO predictions, or even Z/γ^* + $\geqslant$ 1 jet approximate n̄n̄NLO and n̄n̄n̄NLO predictions.

2.3 PYTHIA Monte Carlo

PYTHIA is a general purpose Monte Carlo [29], it can be used to generate LO matrix elements for the hard scattering, to evolve ISR and FSR parton showers, to simulate multiple interaction and pile-up events and to implement hadronization. In the context of the Z/γ^* + jets predictions used in this thesis, the PYTHIA Monte Carlo is not used to generate matrix elements, but to simulate the parton shower evolution and the hadronization for two different generators: ALPGEN which provides Z/γ^* + N jets calculation at LO and POWHEG which evaluates Z/γ^* + 1 jet matrix elements at NLO. Hadronization in PYTHIA is modeled through the Lund model, an implementation of the string model described in section 1.4.3. Different tunes of the underlying event and hadronization parameters have been tested, Tune A [30], Tune DW and Tune Perugia 2011 [31]. PYTHIA Tune A parameters were determined fitting the Tevatron run I underlying event data [32], Tune DW is an improvement based on Tune A which accounts also for the Z-boson p_T spectrum measured in Tevatron Run I and the di-jet $\Delta\phi$ distribution. Both Tune A and Tune DW are based on virtuality-ordered parton shower. Tune Perugia 2011 belongs to the new generation of PYTHIA tunes based on p_T-ordered shower and the interleaved model for the Multiple Interactions [33]. Another important difference of the Perugia tunes with respect to the previous Tune A and DW is that they are tuned on minimum bias data instead of underlying event data [1]. In particular Tune Perugia 2011 includes some early LHC data for the tuning of the parameters, and uses the same value of Λ_{QCD} for all the shower activity, to assure coherence in the choice of α_s in the matching between matrix element generators and parton shower [34]. The merging of the parton shower as implemented in PYTHIA and matrix element generation follows two different approaches for the ALPGEN+PYTHIA and POWHEG+PYTHIA predictions, as described below.

2.4 LO matrix elements matched with parton shower - ALPGEN

ALPGEN is a LO matrix element generator [35] based on the ALPHA algorithm [36]. This technique is based on the recursive evaluation of the S-matrix in a way which reduces the computation time required to evaluate the matrix elements of processes with many particles in the final state. The ALPHA algorithm in fact has a complexity which grows like a power in the number of particles, compared to the factorial-like growing of the number of Feynmann diagrams. In the $Z/\gamma^* + N$ jets process the ALPGEN program can evaluate LO cross sections up to $Z/\gamma^* + 6$ jets, even if for the predictions used in this thesis $Z/\gamma^* +$ jets matrix elements have been calculated only up to 4 jets. Events are generated in a way that enables the subsequent perturbative evolution with a parton shower program, and PYTHIA Monte Carlo is interfaced to ALPGEN in order to get the $Z/\gamma^* +$ jets prediction. The merging between ALPGEN matrix element generator and PYTHIA parton shower is performed following the MLM matching scheme [37]. $Z/\gamma^* + N$ jets samples are generated at LO for each jet multiplicity and showered. To avoid double counting jets are matched to hard partons, and events are accepted only if the number of jets exactly match the number of hard generated partons, except for the sample with the highest multiplicity of hard generated partons in which extra jets are allowed.

2.5 NLO perturbative QCD merged with parton shower - POWHEG

Another implementation of the NLO perturbative QCD calculation is provided by POWHEG [38]. The POWHEG method allows interfacing parton shower generators with NLO QCD computations, in a framework which is independent from the Monte Carlo used for the parton shower. In the POWHEG formalism, the generation of the hardest emission is performed first at NLO, while the subsequent radiation is generated by the shower Monte Carlo (PYTHIA in this case) with an upper limit on the scale equal to the k_T of the POWHEG event. POWHEG+PYTHIA predictions were already compared with the CDF $Z/\gamma^* +$ jets measured cross section in [39].

---

[1] Minimum bias refers to events collected without any bias from restricted trigger conditions, and therefore dominated by low p_T QCD processes.

2.6 NLO electroweak corrections

Full electroweak NLO corrections to the Z/γ^* + jet cross section in the on-shell approximation for the Z-boson were calculated in [17] and more recently for the whole Drell-Yan l^+l^- spectrum in [18]. In both case they predict a negative correction at 300 GeV/c in the Z/γ^* p_T and leading jet p_T of the order of 10%, the most important contribution coming from large Sudakov logarithms in the virtual part of the electroweak corrections. The more precise QCD prediction nowadays available is the $\bar{\text{n}}$NLO calculation of LOOPSIM+MCFM, the uncertainty of this prediction is of the order of 5%, and is dominated by the variation of the factorization and renormalization scale. With such level of precision on the QCD prediction, the NLO electroweak corrections at high p_T give a non negligible contributions which needs to be evaluated. A factorized ansatz is used to combine EW and QCD corrections: the NLO-EW correction factor is evaluated on the LO perturbative QCD calculation, and applied to the NLO-QCD prediction. For the large virtual corrections due to the Sudakov logarithms this is certainly a valid approach, as long as the NLO QCD corrections to the LO QCD prediction are relatively small.

2.7 Further theoretical predictions

The comparison of the measured cross sections is limited to the predictions described above, nevertheless several other Z/γ^* + jets theoretical predictions and Monte Carlo tools are already available or being developed. Among others the most important are the CKKW matching of LO matrix elements and parton shower as performed in the SHERPA framework [40], alternative to the MLM matching employed in the ALPGEN+PYTHIA prediction; the MC@NLO approach for merging fixed order NLO calculation and parton showers [41] using a different formalism with respect to the POWHEG method; the recently developed High Energy Jets (HEJ) resummation framework which can be applied also to W/Z + jets processes [42]; recent efforts have been made in merging the LO-ME+PS CKKW merging with the POWHEG NLO+PS formalism, leading to the so-called MENLOPS approach as proposed in [43] and implemented in the SHERPA Monte Carlo [44].

Chapter 3

The Tevatron accelerator system and the CDF detector

The Tevatron collider has been operating from 1983 until the end of September 2011. The D0 and CDF detectors performed many important measurements of particle physics, among others the discovery of the top quark in 1995. In March 2001 the Tevatron Run II started, with $\mathrm{p\bar{p}}$ collisions at a center-of-mass energy of $\sqrt{s} = 1.96$ TeV. The data analyzed in this thesis correspond to the full Run II dataset collected by the CDF detector between February 2002 and September 2011. Detailed descriptions of the Tevatron accelerator complex and of the CDF detector can be found in the "Accelerator Concepts Rookie Book" [46] and in the "CDF Run II Technical Design Report" [47].

3.1 The Tevatron accelerator complex

The Tevatron is a proton-antiproton synchrotron accelerator located at the Fermi National Accelerator Laboratory, in which $\mathrm{p\bar{p}}$ collisions are produced at a center-of-mass energy of $\sqrt{s} = 1.96$ TeV [48]. The final proton and antiproton beams are the result of a complex acceleration system which involves different stages, spanning from proton and antiproton production, their acceleration and transfer towards different sub-systems, to their actual collision in designed interaction points where the CDF and D0 particle detectors are installed. A schematic view of the Tevatron acceleration chain is provided in Figure 3.1.

3.1.1 The proton source

The process leading to $\mathrm{p\bar{p}}$ collisions begins in a Cockcroft-Walton chamber in which H^- gas is produced by hydrogen ionization. H^- ions are immediately accelerated by a positive voltage to an energy of 750 KeV and transported through a transfer line to the linear accelerator, the Linac [49]. The Linac picks up the H^- ions at the energy of 750 KeV, and accelerates them up to the energy of 400 MeV. The Booster [50] takes the 400 MeV negative hydrogen ions from the Linac and strips the electrons off, which leaves only protons. The Booster is the first circular accelerator in the Tevatron chain, and consists of a series of magnets arranged around a 75-meter radius circle with 18 radio frequency cavities interspersed. When the bare protons are collected in the Booster, they are accelerated to the energy of 8 GeV by the conventional method of varying the phase of RF fields in the

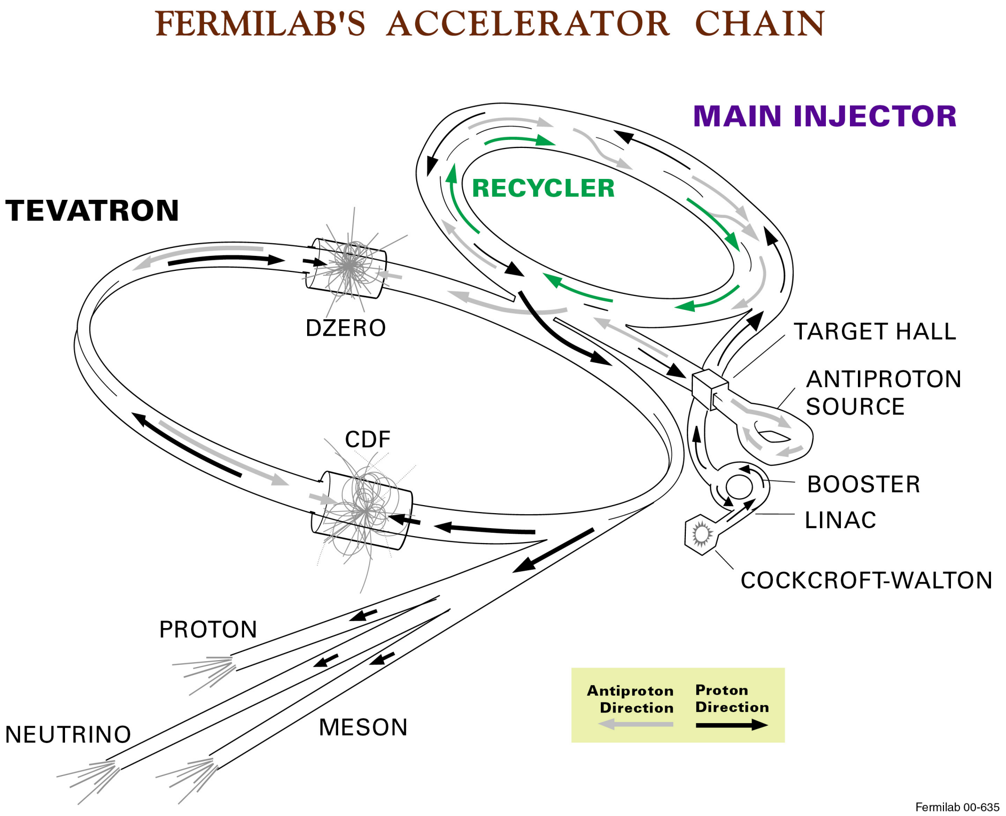

Figure 3.1: The FERMILAB's accelerator chain.

accelerator cavities, and subsequently injected into the Main Injector. The final "batch" will contain a maximum of 5×10^{12} protons divided among 84 bunches spaced by 18.9 ns, each consisting of 6×10^{10} protons.

3.1.2 The Main Injector

The Main Injector (MI) [51] is a circular synchrotron seven times the circumference of the Booster that plays a central role in linking the Fermilab acceleration facilities: the Main Injector can accelerate or decelerate particles, by means of radio frequency (RF) systems, between the energies of 8 GeV and 150 GeV . The sources of these particles and their final destination are variable, depending on the Main Injector operation mode: it can accept 8 GeV proton from the Booster or antiprotons from the Recycler and it can accelerate protons up to 120 GeV for antiproton production. The beam energy, for both proton and antiproton, can reach 150 GeV during the collider mode when particles are injected to the Tevatron for the last stage of the acceleration.

Antiproton production

Providing beam to the antiproton production target is one of the simplest tasks of the Main Injector [52]. In this mode, a single batch of protons is accepted from the Booster, accelerated up to 120 GeV and extracted towards the target, which yields 8 GeV antiprotons as will be described below. Recent upgrades focused in doubling the number of protons on the target station. A new procedure, called "slip stacking" allows to merge two batches from the Booster before sending them to the target station.

Collider operations

Collider Mode is the most complex scenario that the Main Injector has to cope with: in addition to supplying 120 GeV protons for antiproton production, the Main Injector must also feed the Tevatron protons and antiprotons at 150 GeV. The protons and antiprotons need to be filled into super-bunches more intense than any individual bunch that can be accelerated by the Booster. A process called coalescing has been developed for this task; coalescing takes place at Main Injector flat top, that is the maximum energy at which the machine can keep the particles for an extended time. The sequence of steps needed during a shot[1] can be described as follows:

- One batch (84 bunches) of protons is accelerated to 8 GeV by the Booster.
- Only 7 of the batch bunches are extracted to the Main Injector to be accelerated to 150 GeV.
- At flat top the bunches are coalesced, i.e. pushed together to form a narrow, high intensity bunch.
- The coalesced bunch is injected into the Tevatron.
- Previous steps are repeated until 36 coalesced bunches are sent to the Tevatron.
- Meanwhile, the 8 GeV antiprotons from the production target have been stored in the Accumulator, waiting to be injected in the Main Injector with opposite direction with respect to the protons.

---

[1] term indicating the load of protons and antiprotons

- After entering the Main Injector, antiprotons are accelerated to 150 GeV, coalesced and injected in the Tevatron in the opposite direction of protons.
- Main Injector drops back to 8 GeV for another group of antiproton bunches. The process is repeated until 36 antiproton bunches have been delivered to Tevatron.

After these steps the Tevatron ring hosts 36 bunches of protons and 36 of antiprotons at the energy of 150 GeV.

3.1.3 The antiproton source

The number of antiprotons available has always been an important limiting factor in reaching the high luminosity desired for Tevatron physics. They are difficult, or at least time-consuming, to produce. The performance of the proton source greatly affects the quality and duration of the physics run of the Tevatron. Anyway colliding protons and antiprotons has great advantages, for instance the antiprotons can be accelerated in the same ring used for protons because of their opposite charge, thus reducing the cost of the magnets for a second ring. The Fermilab antiproton source consists of a target station, two rings called the Debuncher and Accumulator, and the transfer lines between these rings and the Main Injector. An antiproton beam suitable for collisions in the Tevatron is produced through the following steps.

- A single batch of protons with an intensity up to $4 - 5 \times 10^{12}$ is accelerated by the Main Injector at 120 GeV. Proton beam intensities up to 7×10^{12} have been achieved.
- After the extraction the proton beam proceeds to the target area where its spot size is reduced by means of quadrupole magnets and collides with a nickel target producing showers of secondary particles. Immediately downstream of the target station is located the collection Lithium lens module, in which a solenoidal magnetic field focuses the negative secondaries. Lithium was chosen because it is the least-dense solid conductor which in turn minimizes particles scattering and absorption.
- A pulsed dipole magnet follows the lens. Its purpose is to select 8 GeV negative charged particles and to force them towards the Debuncher. Most of the particles with wrong charge-to-mass ratio are filtered out of the beam and collected by a graphite-core beam-dump.
- Surviving particles, typically 1 or 2 antiprotons for every 105 protons striking the target, are then injected in to the Debuncher where the momentum spread is reduced using stochastic and momentum cooling. The reduction of the momentum spread of incoming particles is needed in order to improve the transfer efficiency from the Debuncher to the Accumulator, because of the limited momentum aperture of the Accumulator at injection. The Debuncher is a rounded triangular-shaped synchrotron with a mean radius of 90 meters.
- Just before the next pulse arrives from the target, the antiprotons are extracted from the Debuncher and injected to the Accumulator, which purpose is to accumulate antiprotons. The Accumulator is a triangular-shaped synchrotron of radius 75 meters housed in the same tunnel of the Debuncher. All the collected antiprotons are stored at 8 GeV and cooled until needed, both RF and stochastic cooling systems are used in the momentum stacking process. The RF decelerates the recently injected pulses of antiprotons from the injection energy to the edge of the stack tail. The stack

tail momentum cooling system sweeps the beam deposited by the RF away from the edge of the tail and decelerates it towards the dense portion of the stack, known as the core. Additional cooling systems keep the antiprotons in the core at the desired momentum and minimize the transverse beam size.

- When enough antiprotons have been accumulated in the Accumulator, their transfer starts. Antiproton beam destination can be either the Main Injector or the Recycler ring.

Overall it can take from 10 to 20 hours to build up a stack of $\sim 3.5 \cdot 10^{12}$ antiprotons, which is then used in the Tevatron collisions.

3.1.4 The Recycler ring

The Recycler [53] is a 3.3 km-long storage ring of fixed 8 GeV kinetic energy, and is located directly above the Main Injector. It is composed solely by permanent gradient magnets and quadrupoles. Three main missions were designed for the Recycler operations: first, it allows antiprotons left over at the end of Tevatron Collider stores to be re-cooled and re-used; secondly, since the antiproton production rate decreases as the beam current in the Accumulator ring rises, the Recycler is designed to act as a post-Accumulator cooler ring, allowing the Accumulator to operate optimally. Finally, permanent magnets were chosen in the construction of the Recycler in order to dramatically reduce the probability of unexpected losses of antiprotons. In fact, the ring has been designed so that Fermilab-wide power could be lost for an hour with the antiproton beam surviving. Recycling the antiprotons left over after the end of Tevatron collisions is a bit involved, since the antiprotons are at 1 TeV. The procedure to accomplish this task takes time and cause huge losses in the remaining number of $\bar{p}$. For these reasons the Recycler is not used anymore for this purpose. Instead the Recycler takes up the role of the Accumulator as the final storage for 8 GeV antiprotons, allowing the existing Antiproton Source to perform more efficiently and to produce antiprotons with higher rate.

3.1.5 The Tevatron ring

The Tevatron [54] is the last stage of the Fermilab accelerator chain. The Tevatron is a 1 km radius synchrotron able to accelerate the incoming 150 GeV beams from Main Injector to 980 GeV, providing a center of mass energy of 1.96 TeV. The accelerator employs superconducting magnets throughout, requiring cryogenic cooling and consequently a large scale production and distribution of liquid helium. The Tevatron operates at the 36 × 36 mode, which refers to the number of bunches in each beam. The antiprotons are injected after the protons have already been loaded. Just before the antiproton injection a set of electrostatic separators are used to create a pair of non-intersecting helical closed orbits. When the Tevatron loading is complete, the beams are accelerated to the maximum energy and collisions begin. There are 72 regions along the ring where the bunch crossing occurs. While 70 of these are parasitic, in the vicinity of CDF and D0 detectors additional focusing and beam steering is performed, to maximize the chance that protons strike antiprotons. The focusing, driven by quadrupole magnets, reduces the beam spot size and thus increases the luminosity. The instantaneous luminosity, a quantity proportional to the number of collisions per unit time, is given approximately by:

$$\mathcal{L} \simeq \frac{N_B N_{\bar{p}} N_p f}{2\pi(\sigma_p^2 + \sigma_{\bar{p}}^2)} \tag{3.1}$$

where N_B is the number of bunches, N_p and $N_{\bar{p}}$ are the number of protons and antiprotons per bunch, f is the revolution frequency, and σ_p^2, $\sigma_{\bar{p}}^2$ are the effective width of the proton and antiproton beams. Smaller $\sigma_{p,\bar{p}}^2$ effective widths lead to larger rate of collisions. The instantaneous luminosity for the Run II dataset analyzed in this thesis is in the range between 0.1×10^{32} cm^{-2}s^{-1} and 4×10^{32}cm^{-2}s^{-1}. During collisions the instantaneous luminosity decreases in time as particles are lost and the beams begin to heat up. Meanwhile, new antiprotons are stored in the Accumulator. When the luminosity becomes too low (approximately after 15-20 hours) it becomes beneficial to dump the current store and start a new cycle.

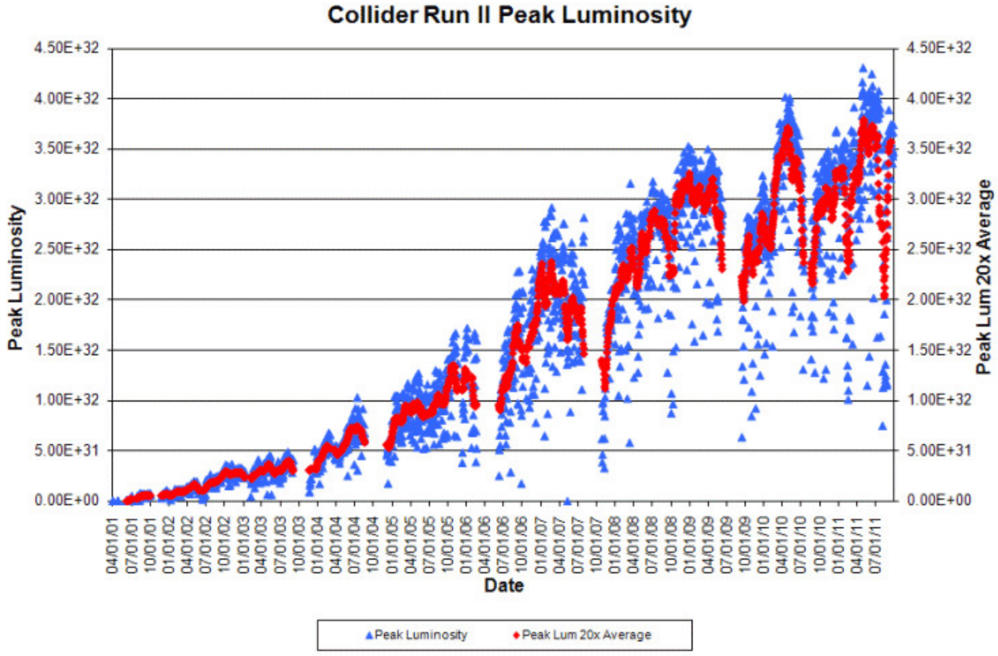

Figure 3.2: Tevatron Run II peak luminosity.

Figure 3.2 shows the Tevatron peak luminosity as a function of the time. The blue squares represent the peak luminosity at the beginning of each store. The red triangles display the average over 20 peak luminosity values. Continuous improvements in the accelerator complex led to the rapid increase of the initial instantaneous luminosity and, more important, to the increase of the rate of integrated luminosity delivered to the experiments. Figure 3.3 shows the weekly and total integrated luminosity as function of time.

3.2 The CDF II detector

CDF II is a general purpose solenoidal detector which combines precision charged particle tracking with fast projective calorimetry and fine grained muon detection. A schematic view of the detector is shown in Figure 3.4, an isometric view in Figure 3.5

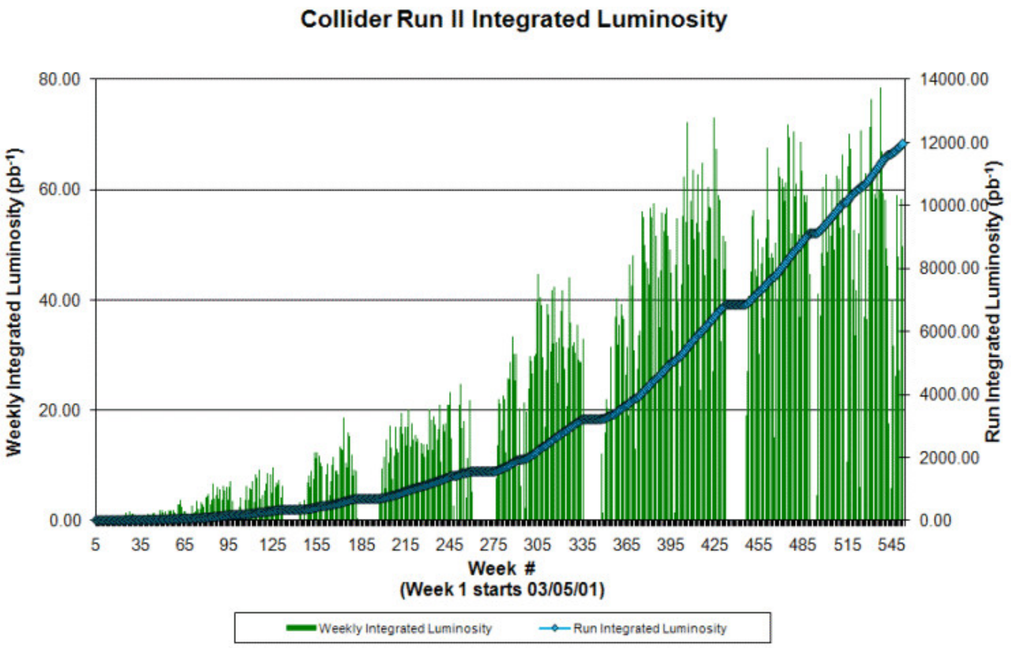

Figure 3.3: Tevatron Run II integrated luminosity.

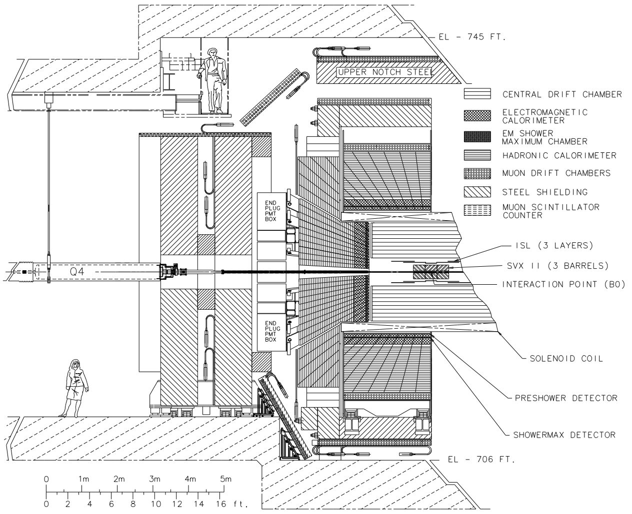

Figure 3.4: Elevation view of the CDF II detector.

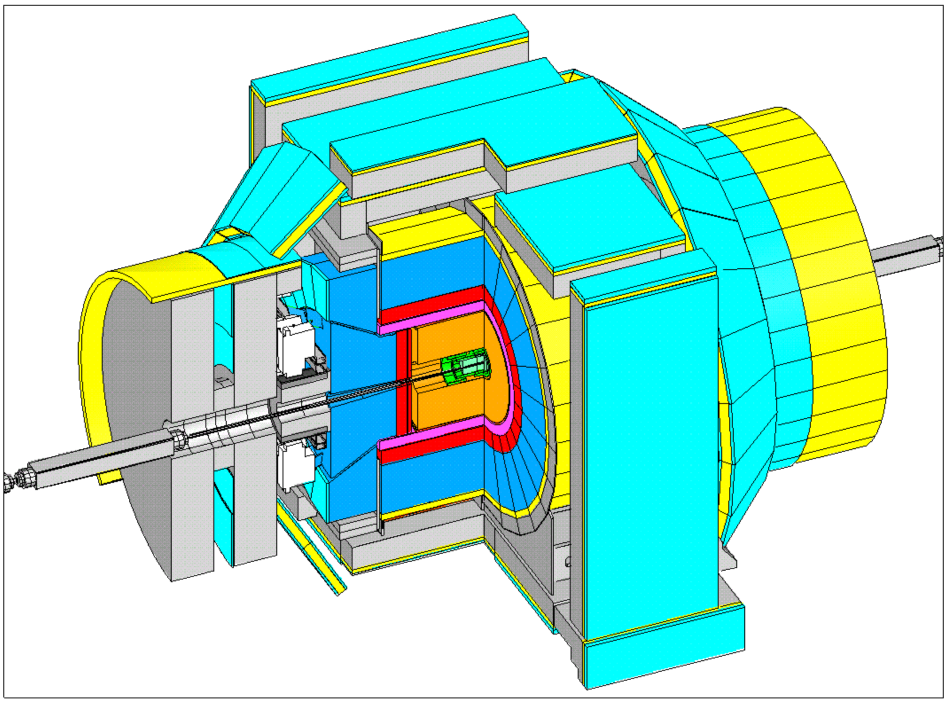

Figure 3.5: Isometric view of the CDF II detector.

3.2.1 The detector coordinate system

Cartesian, spherical and cylindrical coordinate systems are defined with the origin set in the geometrical center of the CDF detector. The z axis lays along the proton beam direction, the y axis points upward and the x axis lays in the accelerator plane pointing away from the center of the Tevatron ring. The azimuthal angle ϕ is measured counter-clockwise from the x axis, the polar angle θ is measured from the proton direction. As described in section 1.2 only a fraction of the proton and anti-proton momentum is carried by the partons which undergo the hard scattering, since this fraction is not known, it is useful to define variables that are invariant under longitudinal boosts. The transverse energy E_T and transverse momentum P_T are defined as:

$$E_T = E \cdot \sin\theta \tag{3.2}$$

$$P_T = P \cdot \sin\theta \tag{3.3}$$

Longitudinal rapidity and pseudorapidity are defined as:

$$y = \operatorname{atanh}(\beta_L) = \frac{1}{2}\log\left[\frac{1+\frac{v_z}{c}}{1-\frac{v_z}{c}}\right] \tag{3.4}$$

$$\eta = -\log(\tan\theta/2) \tag{3.5}$$

Pseudorapidity coincides with rapidity for massless particles, rapidity intervals are invariant under longitudinal boosts. To define the radius of collimated jet of particles it is useful to define an approximately Lorentz-invariant angular distance ΔR:

$$\Delta R = \sqrt{\Delta\eta^2 + \Delta\phi^2} \tag{3.6}$$

3.2.2 The tracking system

The tracking system of the CDF detector is used to measure the trajectory of charged particles originated in the collisions. It comprises an inner silicon tracker and a open cell drift chamber named Central Outer Tracker (COT). The tracking system is immersed in a 1.4 Tesla magnetic field generated by a superconducting solenoid of 1.5 m of radius. A schematic view of the tracking system is shown in Figure 3.6.

Particle trajectories can be completely described by five parameters:

- z_0: the z coordinate of the closest point to the z axis;
- d_0: the impact parameter defined as the shortest distance of a particle trajectory from the z axis;
- ϕ_0: the ϕ coordinate of the transverse momentum of the particle (tangential to the helix) at the point of the closest approach to the z axis;
- $\cot\theta$: cotangent of the polar angle at the point of closest approach to the z axis;
- C: the helix curvature.

Particle transverse and longitudinal momenta can be derived from the helix parameters:

$$P_T = \frac{cB}{2|C|} \tag{3.7}$$

$$P_z = P_T \cdot \cot\theta \tag{3.8}$$

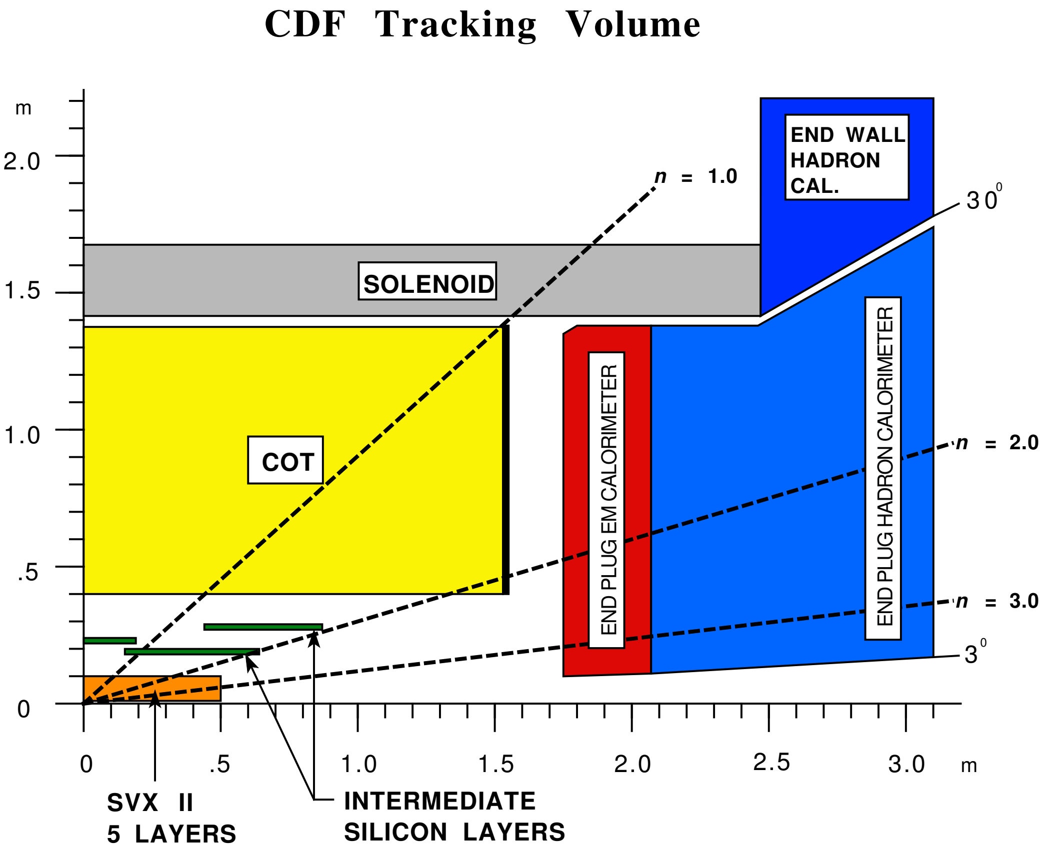

Figure 3.6: Longitudinal view of the CDF II Tracking System.

The silicon detector

The silicon detector [55] is a 8-layer silicon micro-strip tracker designed to provide high resolution measurement of the impact parameter of tracks, and to increase the acceptance of the COT outer tracker in the forward regions of the detector. The system is composed by 3 subdetectors and covers the region $|\eta| < 2.8$. The innermost layer (Layer00) goes from $r = 1.35$ cm to 2.4 cm and is mounted directly on the beam pipe. The next 5 layers constitute the Silicon Vertex detector (SVX II) and expand from $r = 2.4$ cm to 10.6 cm. The SVX detector is designed to improve the resolution in the determination of the impact parameter of tracks d_0, evaluated with respect to the primary interaction vertex. The Intermediate Silicon Layers (ISL) are located between the SVX II and the COT drift chamber. The SVX and ISL layers are double-sided detectors, while the Layer00 is single-sided. The impact parameter resolution of the combination of ISL and SVX II is $\sim 40\ \mu$m, including a 30 μm contribution from the resolution of the beamline position. Figure 3.7 shows a frontal view of the 3 silicon subdetectors.

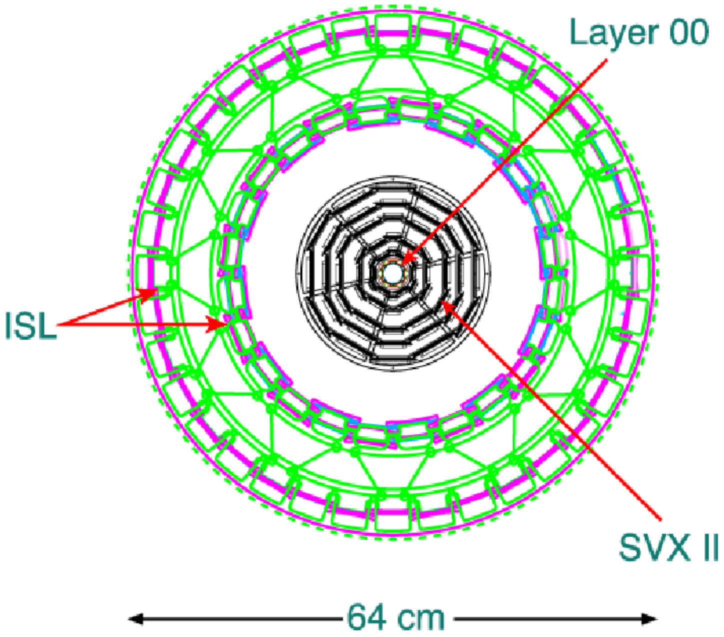

Figure 3.7: Frontal view of the silicon detector.

The COT chamber

The silicon detector is surrounded by the Central Outer Tracker (COT). The COT [56] is a cylindrical, open cell, multiwire drift chamber. The cylinder is 310 cm long, radially expands from $r = 40$ cm to 137 cm, and provides a coverage in pseudorapidity up to $|\eta| < 1$. A schematic view of the COT is shown in Figure 3.8.

The sense wire of the drift chamber are grouped in 8 "superlayers" (SL). The SL are divided along ϕ into "supercells", each supercell containing 12 sense wires and 13 potential wires (40 μm diameter gold coated tungsten wires), and delimited by 6.3 μm

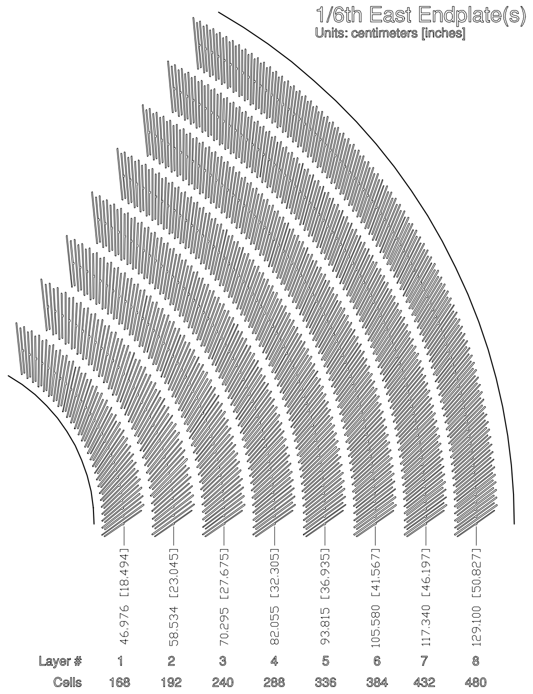

Figure 3.8: Schematic view of the COT superlayers.

thick gold coated mylar field sheets. Superlayers of wires parallel to z axis and of wires inclined at a small angle of $\sim 3^\circ$ with respect to the z axis are alternated, they are called respectively "Axial" and "Stereo" superlayers. The combination of the axial and stereo measurements provide z and $r - \phi$ position information. Single hit resolutions in the COT of 140 μm translate into transverse momentum resolutions of $\sigma(p_T)/p_T = (0.15\%) \times p_T[(\text{GeV/c})^{-1}]$. If silicon tracking information is added, the resolution improves to $(0.07\%) \times p_T[(\text{GeV/c})^{-1}]$. The COT chamber is filled with a gas mixture of Argon-Ethane (50:50) that provides a constant electron drift velocity across the cells. As the COT is immersed in a magnetic field, the electrons drift at a Lorentz angle of 35°. Supercells are tilted by 35° with respect to the radial direction to compensate this effect. Small quantities of Oxygen and Isopropyle are added to the gas mixture to reduce aging effects on the wires.

3.2.3 Time of flight detector

The Time of Flight (TOF) detector lies between the COT and the solenoid and is formed by 216 3-meter long scintillating bars located at $r \sim 140$ cm, a photo-multiplier tube is attached at both ends of each bar. Bars are segmented in 1.7° along ϕ and covers the pseudorapidity range $|\eta| < 1$. The TOF detector is used to distinguish between low momentum pions, kaons and protons, through the measurement of the time they take to travel from the primary vertex to the TOF system. Particles time of flight is measured with a resolution of ~ 100 ps.

	Coverage	$\eta \times \phi$ Segmentation	Resolution (E_T in GeV)
CEM	$\|\eta\| < 1.1$	0.1×0.26	$14\%/\sqrt{E_T} \oplus 2\%$
CHA	$\|\eta\| < 0.9$	0.1×0.26	$50\%/\sqrt{E_T} \oplus 3\%$
WHA	$0.9 < \|\eta\| < 1.3$	0.1×0.26	$75\%/\sqrt{E_T} \oplus 4\%$
PEM	$1.1 < \|\eta\| < 3.6$	$(0.1 - 0.6) \times (0.13 - 0.26)$	$16\%/\sqrt{E_T} \oplus 1\%$
PHA	$1.2 < \|\eta\| < 3.6$	$(0.1 - 0.6) \times (0.13 - 0.26)$	$80\%/\sqrt{E_T} \oplus 5\%$

Table 3.1: Coverage, segmentation, thickness and resolution of the CDF II calorimeter system.

3.2.4 Calorimetric systems

The CDF calorimetric system has been designed to measure energy and direction of neutral and charged particles which escapes the tracking region. Particles hitting the calorimeter can be divided into two classes according to their interaction with matter: electromagnetic interacting particles, such as electrons and photons, and hadronic interacting particles, such as mesons or baryons produced in hadronization processes. To detect these two classes of particles, two different calorimetric parts have been developed: an inner electromagnetic and an outer hadronic section. The calorimetric subsystems provide pseudorapidity coverage up to $|\eta| < 3.6$, and are segmented in $\eta - \phi$ sections, called towers, projected towards the geometrical center of the detector. Each tower consists of alternating layers of passive material and scintillator tiles. The signal is read out via wavelength shifters (WLS) embedded in the scintillator and the light from WLS is carried through light guides to photomultiplier tubes. The energy E measured in a given tower is the sum of the energy deposited in the electromagnetic calorimeter and in the hadronic calorimeter corresponding to that tower: $E = E_{\text{EM}} + E_{\text{HAD}}$. The calorimetric system is subdivided into three regions, central, wall and plug, in order of increasing pseudorapidity ranges, with the following naming convention: Central Electromagnetic (CEM), Central Hadronic (CHA), Wall Hadronic (WHA), Plug Electromagnetic (PEM) and Plug Hadronic (PHA). The most relevant characteristics of the CDF II calorimeters are summarized in Table 3.1

The Central Calorimeter

The Central Electro-Magnetic calorimeter (CEM) is segmented in $\eta \times \phi = 0.11 \times 15°$ projective towers consisting of alternate layers of lead and scintillator, while the Central and End Wall Hadronic calorimeters (CHA and WHA respectively), whose geometric tower segmentation matches the CEM one, use iron layers as radiators. A perspective view of a central electromagnetic calorimeter module, a wedge, is shown in Figure 3.9.

Two position detectors are embedded in each wedge of the CEM:

- The Central Electromagnetic Strip chamber (CES) is a two-dimensional strip/wire chamber located at the radial distance 184 cm. It measures the charge deposition of the electromagnetic showers, providing information on their pulse-height and position with a finer azimuthal segmentation than the calorimeter towers. This results in an increased angular resolution of electromagnetic object reconstruction.

- The Central Pre-Radiator (CPR) consists of two wire chamber modules placed immediately in front of the calorimeter. It acts as a pre-shower detector and with its 3072 channels collects charge deposit of showers originated by interaction of particles

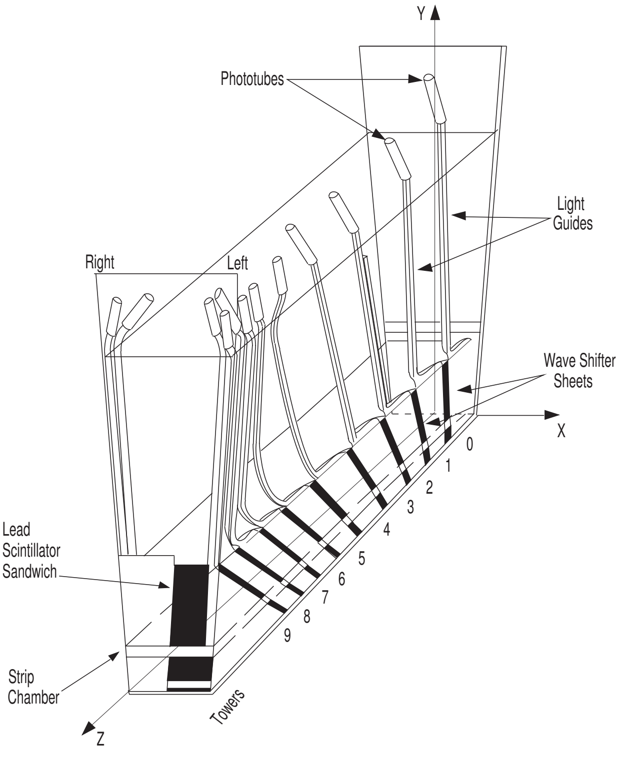

Figure 3.9: Perspective view of a CEM wedge.

with the tracking system and the solenoid material. It helps discriminating pions from electron and photons, because the latter deposit a greater amount of energy in the chamber.

The energy resolution of each segment of the calorimeter for a single particle has been measured using a testbeam and can be parametrized as:

$$\frac{\sigma}{E_T} = \frac{a}{\sqrt{E_T}} \oplus b \tag{3.9}$$

The first term a comes from sampling fluctuations and photostatistics of PMTs, the constant term b comes from the intercalibration between the different towers and the non-uniform response of the calorimeter, E_T is the transverse energy of the particle in GeV. For the CEM, the energy resolution parameters of high-energy electrons and photons are $a = 14\%[\text{GeV}]^{1/2}$ and $b = 2\%$. Charged pions were used to evaluate the energy resolution in the hadronic calorimeters, resolution parameters for the CHA are $a = 50\%[\text{GeV}]^{1/2}$ and $b = 3\%$, and for the WHA $a = 75\%[\text{GeV}]^{1/2}$ and $b = 4\%$.

The plug calorimeter

The plug calorimeter, shown in Figure 3.10, covers the pseudorapidity region $|\eta| = 1.1-3.6$. Both electromagnetic and hadronic sectors are divided in 12 concentric regions, with η width ranging from 0.10 to 0.64 according to increasing pseudorapidity, each segmented in 48 or 24 (for $|\eta| < 2.1$ or $|\eta| > 2.1$ respectively) projective towers. As in the central calorimeter, there is a front electromagnetic compartment and a rear hadronic compartment (PEM and PHA). Projective towers consist of alternating layers of absorbing material (lead and iron for electromagnetic and hadronic sectors respectively) and scintillator tiles. The first layer of the electromagnetic calorimeter acts as a pre-shower detector; to this scope, the first scintillator tile is thicker (10 mm instead of 6 mm) and made of a brighter material.

As in the central calorimeter, a shower maximum detector is also included in the plug electromagnetic calorimeter (PES). The PES consists of two layers of 200 scintillating bars each, oriented at crossed relative angles of 45° (±22.5° with respect to the radial direction). The position of a shower on the transverse plane is measured with a resolution of ~ 1 mm. Resolution parameters for the plug calorimeter, measured with testbeam, are $a = 16\%[\text{GeV}]^{1/2}$, $b = 1\%$ for the PEM, and $a = 80\%[\text{GeV}]^{1/2}$, $b = 5\%$ for the PHA.

3.2.5 The muon detectors

The CDF muon detector system [57] consists of drift chambers and scintillator counters, and covers a pseudorapidity range up to $|\eta| < 1.5$. The muon subsystems are located in the outer part of the CDF II detector, behind the most of the CDF detector material.

The central muon detector (CMU) is located right outside the CHA behind ~ 5 nuclear interaction absorption lengths λ_0 of detector material. It covers the pseudorapidity range $|\eta| < 0.68$. It is composed of a barrel with inner and outer radii $r_i = 347$ cm and $r_o = 396$ cm respectively, containing 4 drift tube layers sectioned by wedge matching the CHA towers: 3 sections of 4 tubes per layer per 15° wedge. Each tube operates in proportional mode, with a maximum drift time of 0.8 μs. The transtube multiple scattering resolution is $12/(p[\text{GeV}])$ cm and the longitudinal resolution is $\delta_z \simeq 10$ cm. The central muon upgrade detector (CMP) is located outside the CMU behind ~ 8 λ_0 of detector material that includes additional 60 cm thick steel slabs. The CMP contains four layers of rectangularly

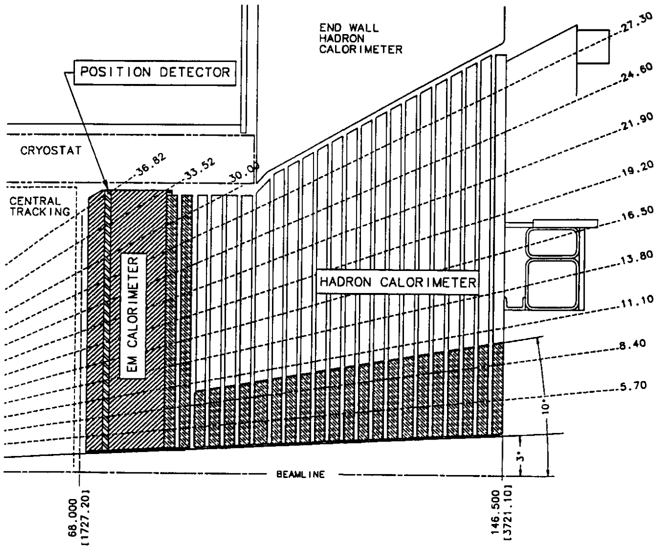

Figure 3.10: Schematic view of the plug calorimeter.

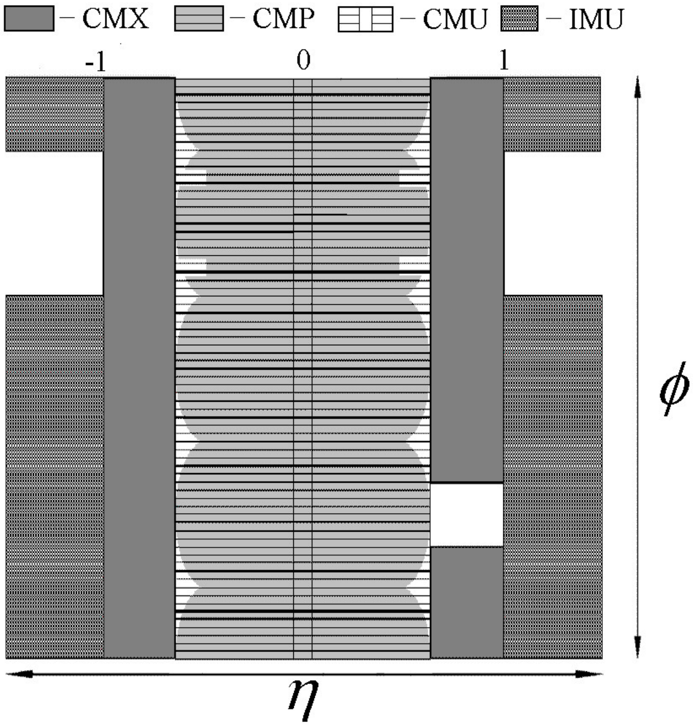

Figure 3.11: $\eta - \phi$ coverage of the CMU, CMP and CMX central muon detectors.

arrayed drift tubes. The rapidity extension of the CMP detector is $|\eta| < 0.68$. The CMP gas operation mode is proportional, the maximum drift time is 1.4 μs and it has a transtube multiple scattering resolution of $15/(p[\text{GeV}])$ cm. A layer of scintillators (CSP) mounted onto the outside surface of the CMP provides timing information with a resolution of $1-2$ ns. The central muon extension detector (CMX) consists of conical sections facing toward the interaction point behind $6-9$ λ_0 of detector material. The CMX system extends the central muon detector pseudorapidity coverage in the region $0.65 < |\eta| < 1.0$, except the east top 30° in azimuth. The CMX detector contains two folds of 4 layers of rectangular drift tubes. The transtube multiple scattering resolution is $13/(p[\text{GeV}])$ cm and the longitudinal position resolution is $\delta_z \simeq 14$ cm. Two layers of scintillators CSX provides timing information for the CMX, One layer is mounted on the outer surface and the other on the inner surface of the CMX drift chambers.

The intermediate muon detector (IMU) is built behind $6.2-20$ λ_0 of material, depending on the rapidity. It consists of two barrels which extends the CDF geometric muon acceptance in the pseudorapidity range $1.0 < |\eta| < 1.5$. It contains four layers of proportional drift tubes (BMU), with a maximum drift time of 0.8 μs. The transtube multiple scattering resolution is $13-25/(p[\text{GeV}])$ cm and the longitudinal position resolution is $\delta_z \simeq 16.5$ cm. Three layers of scintillators (BSU-F, BSU-R and TSU) are mounted outside the BMU and provide timing information.

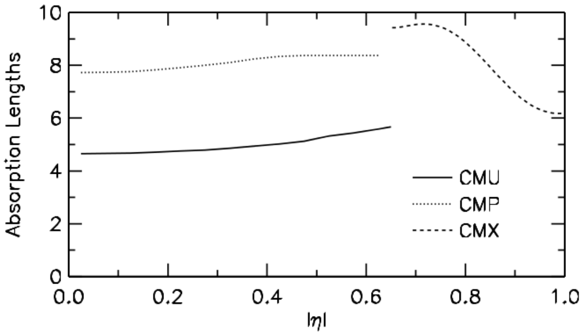

Figure 3.12: Number of absorption lengths λ_0 as a function of pseudorapidity averaged over azimuthal acceptance of the CMU, CMP and CMX systems.

The $\eta-\phi$ coverage of the muon detectors is shown in Figure 3.11, Figure 3.12 shows the number of absorption lengths λ_0 as a function of pseudorapidity for central muon systems. For the current $Z/\gamma^* \to l^+l^-$ + jets measurement only the central muon systems CMU, CMP and CMX have been used. The BMU system in fact has higher fake muon rates, and BMU based triggers need to be implemented with additional requirements on jets. Such requirements would bias the jets kinematic of a $Z/\gamma^* \to \mu^+\mu^-$ + jets sample collected with BMU triggers.

3.2.6 Cherenkov luminosity counters

CDF measures the collider luminosity with a coincidence between two arrays of Cherenkov counters, the CLC, placed around the beam pipes on the two detector sides [58]. They are located inside the endplug calorimeters, in the forward and backward regions ($3.7 < |\eta| <$

4.7). Each module consists of 48 thin, long, conical, gas filled Cherenkov counters. These counters are arranged around the beam pipe in three concentric layers with 16 counters each and pointing to the center of the interaction region. The counters measure the average number of interactions per bunch crossing μ, which is used to provide a measurement of the instantaneous luminosity L:

$$\mu \cdot f_{bc} = \sigma_{\mathrm{p\bar{p}}} \cdot L \tag{3.10}$$

where $\sigma_{\mathrm{p\bar{p}}}$ is the total $\mathrm{p\bar{p}}$ inelastic cross section and f_{bc} is the bunch crossing rate of the Tevatron. The $\mathrm{p\bar{p}}$ total inelastic cross section at $\sqrt{\sigma} = 1.96$ TeV is $\sigma_{\mathrm{p\bar{p}}} = 60.7 \pm 2.4$ mb [60], this value has been extrapolated from the measurement at $\sqrt{\sigma} = 1.8$ TeV [59]. The integrated luminosity is measured with a systematic uncertainty of 5.8%.

3.2.7 Trigger and data acquisition systems

At hadron collider experiments the collision rate is much higher than the rate at which data can be stored on tape. Tevatron bunches are separated by 396 ns, leading to a crossing rate of 2.5 MHz, while the tape writing speed is ~ 100 events per second. The role of the trigger is to efficiently select the most interesting physics events. Events selected by the trigger system are saved permanently on a mass storage and subsequently reconstructed offline.

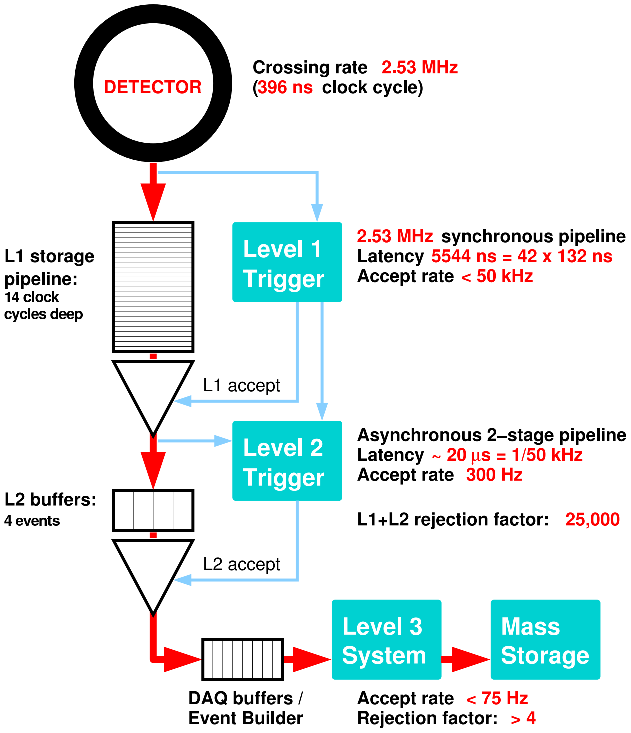

Figure 3.13: Schematic representation of the CDF II trigger and data acquisition systems.

The CDF trigger system has a three-level architecture, each level provides a rate reduction sufficient to allow processing in the next level with minimal deadtime. Figure

3.13 shows a schematic representation of the CDF data acquisition system. The front-end electronics of all detectors is interfaced to a synchronous pipeline where up to 42 subsequent events can be stored for 5.5 μs, while the Level 1 (L1) trigger hardware is taking a decision. L1 decisions always occurs at a fixed time lower than 4 μs, so that no deadtime is associated to this trigger level. L1 uses designed hardware to make decisions based on simple physics quantities reconstructed with a subset of the detector information. As shown in Figure 3.14, three different streams of information enter the L1 decision: calorimeter objects that may be further reconstructed into electrons, photons or jets, track segments in the muon detector, and tracking data to identify tracks which can be linked to objects in the calorimeter or muon detector. After L1, the event rate is reduced to less than 50 kHz. Events passing the L1 trigger requirements are moved to one of four on-board Level 2 (L2) buffers. Each separate L2 buffer is connected to a two-step pipeline, each step having a latency time of 20 μs: in step one, single detector signals are analyzed, while in step two the combination of the outcome of step one are merged and trigger decisions are made. The input data for L2 consists of L1 tracks, L1 muons, shower maximum calorimeters and data from the silicon detectors. The L2 trigger system consists of several asynchronous subsystems: the Cluster Finder (L2CAL) runs over calorimeter data to find clusters of energy; the Silicon Vertex Tracker (SVT) uses silicon detector hits to reconstruct tracks with high resolution in the impact parameter d_0, useful to select displaced tracks coming from B hadron decays; XCES boards analyze shower maximum detectors data to find isolated energy clusters and use track information to distinguish between electrons and photons. The data acquisition system allows a L2 trigger accept rate of ~ 1 kHz. Events satisfying both L1 and L2 requirements are transferred to the Level 3 (L3) trigger processor farm where they are reconstructed and filtered using the complete event information, with an accept rate of ~ 100 Hz, and then finally written to tape for permanent storage. Requirements are set for each trigger level based on the available reconstructed objects (primitives), and according to the physical process selection that a specific trigger is aimed at. Links across different levels are established by defining trigger paths, which identify a unique combination of a L1, a L2, and a L3 trigger. Data sets (or data streams) are then formed by merging the data samples collected via different trigger paths. Figure 3.14 shows the data flow of the L1 and L2 trigger systems.

Some trigger paths have output rates that exceed the maximum allowed value. To avoid the introduction of further selections which would bias the data sample such trigger paths are *prescaled* by a factor N, i.e. just one event out of N is accepted. Fixed prescale factors are called *static*, prescale factors which vary depending on the instantaneous luminosity to better exploit the available bandwith are called *dynamic*.

3.2.8 Data storage and offline processing

The data flow from L3 triggers is stored in real time on fast-access disks, all subsequent data processing data is referred as *offline* data handling. Stored raw data are unpacked, and physics objects as tracks, vertices, leptons and jets are reconstructed. The offline processing is similar to the L3 trigger reconstruction, with the difference that physics objects can be more elaborated and the most up-to-date detector calibrations are used. Offline processed data are divided into data sets which are used as input to physics analyses. Collected data are grouped during online acquisition in run numbers, during the offline processing several run numbers are grouped in run periods which integrated luminosity is of the order of ~ 100 pb^{-1}. Table 3.2 shows the run period subdivision of the CDF Run II data. In this thesis the full CDF II dataset collected between February 4th 2002 and

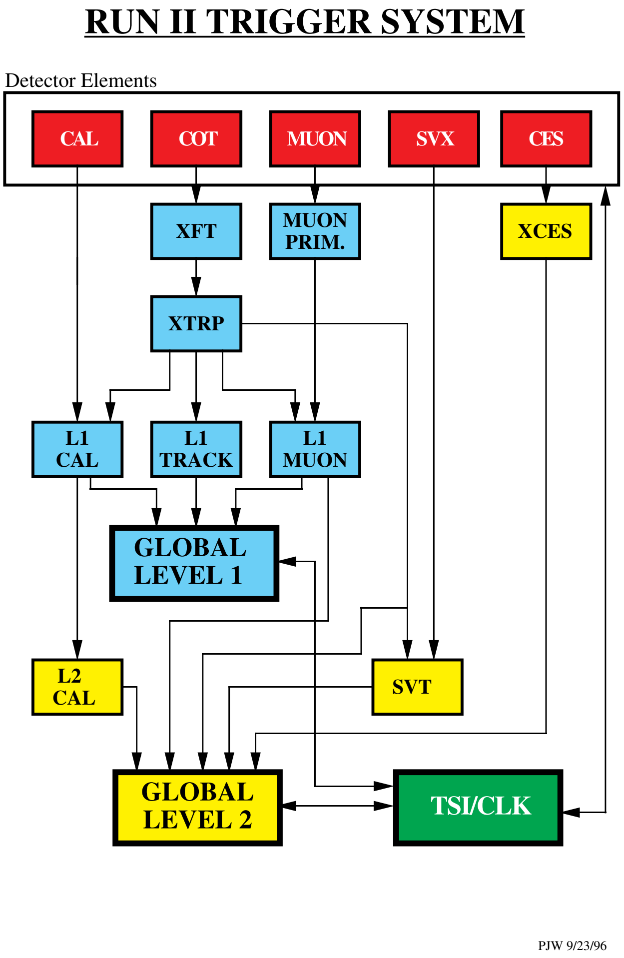

Figure 3.14: Block diagram of the CDF Level 1 and Level 2 trigger systems.

September 30th 2011 has been analyzed, which corresponds to an integrated luminosity of ~ 10 fb^{-1}.

3.3 Physics objects reconstruction

The $Z/\gamma^* \to l^+l^-$ + jets production measurement involves the reconstruction and identification of several physics objects in the final state. Muons, electrons and jets of particles need to be reconstructed from the raw data collected by the detector, often matching the information coming from different subsystems. Also the primary interaction vertex needs to be reconstructed, as its position is used as the reference point for the jet clustering.

3.3.1 Electron reconstruction

Electron objects are reconstructed from energy deposit in one or two calorimeter towers matched to clusters in the shower maximum detector and to reconstructed tracks. Depending on which part of the calorimeter system the cluster belongs to, the electrons are divided in Central (CEM) and Plug (PEM) electrons. CEM electrons are reconstructed from electromagnetic clusters in the central calorimeter, which covers a region in pseudorapidity up to $|\eta| < 1.0$, PEM electrons are reconstructed in the plug calorimeters and have pseudorapidity in the range $1.2 < |\eta| < 2.8$. Since muon reconstruction is limited by the COT coverage to $|\eta| < 1.0$, in order to combine the $Z/\gamma^* \to e^+e^-$ and $Z/\gamma^* \to \mu^+\mu^-$ channels in the same kinematic region only CEM electrons are used in this Z/γ^* + jets measurement. Tracks associated to electrons are beam constrained using the average beam position evaluated for each run of data taking, and a ϕ dependent correction is applied to the p_T of the track to account for misalignment of the COT tracking system. For the reconstruction of the particle 4-momentum $(E, \vec{p})$ electrons are assumed to be massless, track information is used to set the three dimensional direction $\vec{p}/|p|$ while the energy measured in the calorimeter determines the magnitude $E = |\vec{p}|$.

3.3.2 Muon reconstruction

Muon objects are reconstructed from tracks in the COT and silicon subdetectors, which can be matched to stubs in the CMU, CMP and CMX muon detectors. The muon 4-momentum $(E, \vec{p})$ is reconstructed from the p_T and ϕ of the associated track and setting the invariant mass equal to the muon invariant mass $M_\mu = 105.7$ MeV/c^2. As for the electrons the tracks associated to muons are constrained to the beam position, and a ϕ dependent correction is applied to the p_T of the track to account for COT misalignment.

3.3.3 Primary vertex reconstruction

The position along the z axis of the primary interaction vertex is used as a reference point to evaluate the θ coordinate of the calorimeter towers before the jet clustering. The z position of the primary vertex is determined through an algorithm which combines the information of the reconstructed tracks of the events. In the first step the average z_V of the z_0 parameter of all the tracks is evaluated. For each track a χ^2 with respect to z_V is evaluated as:

$$\chi^2 = \frac{(z_V - z_{0,i})^2}{\sigma^2_{z_{0,i}}}$$

Period	Online data taking	Integrated Luminosity [pb^{-1}]
0 (0d)	04 Feb 02 - 22 Aug 04	504.8
1-4 (0h)	07 Dec 04 - 04 Sep 05	464.0
5-7	05 Sep 05 - 22 Feb 06	293.6
8	09 Jun 06 - 01 Sep 06	212.2
9	01 Sep 06 - 22 Nov 06	180.8
10	24 Nov 06 - 31 Jan 07	270.7
11	31 Jan 07 - 30 Mar 07	248.1
12	01 Apr 07 - 13 May 07	169.8
13	13 May 07 - 4 Aug 07	323.6
14	28 Oct 07 - 3 Dec 07	58.4
15	5 Dec 07 - 27 Jan 08	168.2
16	27 Jan 08 - 27 Feb 08	128.9
17	28 Feb 08 - 16 Apr 08	189.3
18	18 Apr 08 - 01 Jul 08	428.3
19	01 Jul 08 - 24 Aug 08	286.1
20	24 Aug 08 - 04 Oct 08	259.8
21	12 Oct 08 - 01 Jan 09	503.8
22	2 Jan 09 - 10 Feb 09	283.0
23	15 Feb 09 - 21 Mar 09	232.6
24	22 Mar 09 - 04 May 09	292.2
25	05 May 09 - 13 Jun 09	236.2
26	15 Sep 09 - 25 Oct 09	192.3
27	25 Oct 09 - 05 Jan 10	425.4
28	06 Jan 10 - 25 Feb 10	272.4
29	26 Feb 10 - 13 Apr 10	359.3
30	13 Apr 10 - 19 Jun 10	460.5
31	20 Jun 10 - 17 Jul 10	177.0
32	21 Aug 10 - 01 Nov 10	446.7
33	01 Nov 10 - 24 Dec 10	376.2
34	06 Jan 11 - 06 Mar 11	389.8
35	12 Mar 11 - 13 May 11	392.7
36	15 May 11 - 05 Jul 11	433.2
37	05 Jul 11 - 16 Aug 11	182.4
38	16 Aug 11 - 30 Sep 11	256.7
Total	04 Feb 02 - 30 Sep 11	10.1 fb^{-1}

Table 3.2: Run period subdivision of data collected by the CDF detector in Run II. For each period the starting and ending dates and the corresponding integrated luminosity are shown.

where i is an index running on the tracks, $z_{0,i}$ is the z_0 parameter of track i and $\sigma_{z_{0,i}}$ is the uncertainty associated to z_{0i}. Tracks with $\chi^2 > 3$ are excluded, and the vertex z position z_V is calculated as:

$$z_V = \frac{\sum_i \frac{z_{0,i}}{\sigma^2_{z_{0,i}}}}{\sum_i \frac{1}{\sigma^2_{z_{0,i}}}}$$

The last step is repeated until the set of surviving track is stable. The resolution of z_V depends on the number of tracks in the event, typical values are of the order of $\sigma_{z_V} \simeq 45\ \mu\text{m}$.

3.3.4 Jet reconstruction

The jet algorithm used for the Z/γ^* + jets measurement is the Run II CDF midpoint implementation [61], with cone radius $R = 0.7$ and the merging/splitting fraction threshold set to $f = 0.75$. Jets are clustered considering as seeds all the towers with energy above 1 GeV, and using calorimeter towers with energy higher than 0.1 GeV. The 4-momentum associated to a calorimeter tower is determined as:

$$px = E_{\text{EM}} \cdot \sin\theta_{\text{EM}} \cdot \cos\phi_{\text{EM}} + E_{\text{HAD}} \cdot \sin\theta_{\text{HAD}} \cdot \cos\phi_{\text{HAD}} \tag{3.11}$$

$$py = E_{\text{EM}} \cdot \sin\theta_{\text{EM}} \cdot \sin\phi_{\text{EM}} + E_{\text{HAD}} \cdot \sin\theta_{\text{HAD}} \cdot \sin\phi_{\text{HAD}} \tag{3.12}$$

$$pz = E_{\text{EM}} \cdot \cos\theta_{\text{EM}} + E_{\text{HAD}} \cdot \cos\theta_{\text{HAD}} \tag{3.13}$$

$$E = E_{\text{EM}} + E_{\text{HAD}} \tag{3.14}$$

where E_{EM} and E_{HAD} are the amount of energy deposited in the electromagnetic and hadronic segment of the tower, and θ_{EM}, θ_{HAD}, ϕ_{EM}, ϕ_{HAD} are the angular coordinates of the shower maximum position of an electromagnetic and hadronic shower, evaluated using the primary interaction vertex as the center of the reference frame. Notice that when the primary vertex is displaced from the center of the detector θ_{EM} and θ_{HAD} have different values, as shown in Figure 3.15.

The 4-momentum of the jets are reconstructed recombining the towers 4-momenta following the E-scheme:

$$\mathbf{p}_{\text{jet}} = \sum_{\text{towers}} \mathbf{p}_i = \sum_{\text{towers}} (\vec{p}_i, E_i) \tag{3.15}$$

Transverse momentum $p_{T,\text{jet}}$ and rapidity y_{jet} are evaluated as:

$$p_{T,\text{jet}} = |\vec{p}_{\text{jet}}| \cdot \sin\theta \qquad y_{\text{jet}} = \frac{1}{2} \ln \frac{E + p_z}{E - p_z} \tag{3.16}$$

where θ is the polar angle. Rapidity y is used instead of pseudorapidity η because in the E-scheme jets are massive and only rapidity intervals Δy are invariant under Lorentz longitudinal boosts.

A specific lepton removal for the jet clustering was developed for the Z/γ^* + jets measurement, following a procedure similar to that of the previous $Z/\gamma^* \to e^+e^-+$ jets CDF measurement [20]. Calorimeter towers associated to reconstructed and identified electrons and muons are excluded from the jet clustering. Such removal avoids the contribution to the jets reconstruction of the electromagnetic clusters associated to the $Z/\gamma^* \to l^+l^-$ decay, and also prevents the possibility that seeds coming from the lepton energy deposit in the calorimeter introduce a bias in the jet clustering.

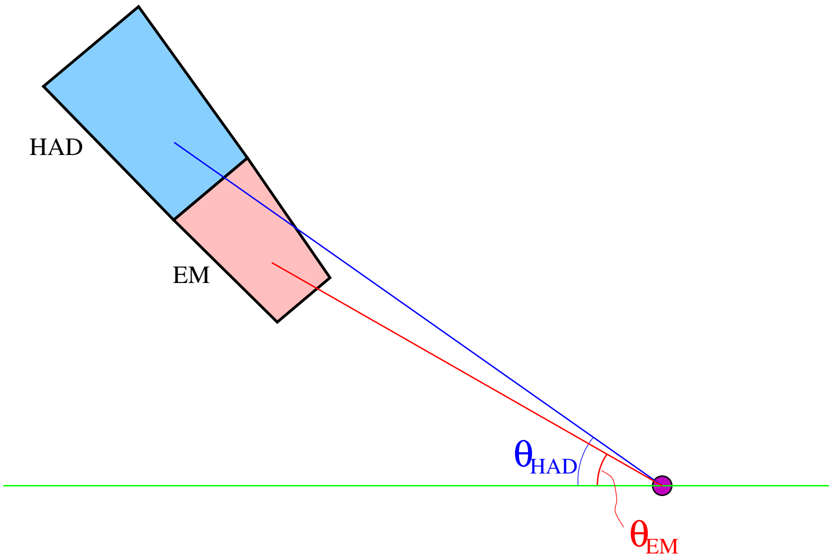

Figure 3.15: Determination of θ_{EM} and θ_{HAD} for a CDF calorimeter tower. θ_{EM} is the polar angle of the maximum of a typical electromagnetic shower developed in the tower with respect to the primary vertex, θ_{HAD} is the polar angle of the maximum of a typical hadronic shower. Figure taken from [61].

Jet energy corrections

The measured jet transverse momenta are corrected to particle level using the method described in [63]. The program GFLASH [64] is used to simulate electromagnetic and particle showers in the calorimeter, parameters of the simulation either are tuned with single isolated tracks from minimum bias data and test beam data, or the default setting from the H1 collaboration is used. Test beams of charged pions in the p_T range $7-230$ GeV/c and electrons in the p_T range $5-180$ GeV/c are used for the calibration of the hadronic and electromagnetic calorimeters. The energy calibration of the calorimeter is validated comparing the ratio E/p of the calorimeter energy over the track momentum in data and Monte Carlo simulated samples of single isolated tracks. Figure 3.16 shows E/p as a function of the particle momentum in the central calorimeter.

Even after the calorimeter energy calibrations the measured jet p_T is generally underestimated due to the presence of non-instrumented parts of the detector and because of the non-compensated nature of the calorimeters. Moreover in hadron collisions jets receive energy contribution from multiple p$\bar{\text{p}}$ interactions in the same bunch crossing. A jet energy correction is then applied to the jet p_T, which general form is:

$$p_T = [p_T^{\text{raw}} \times f_\eta - f_{\text{p}\bar{\text{p}}\text{I}}] \times f_{\text{jes}} \tag{3.17}$$

where p_T^{raw} is the measured jet p_T after the calorimeter energy calibration, f_η, $f_{\text{p}\bar{\text{p}}\text{I}}$ and f_{jes} are factors which correspond to different corrections:

- f_η is a correction depending on the detector pseudorapidity. A dependence of the calorimeter response with η arise from the separation of the calorimeter components at $\eta = 0$, where the two halves of the central calorimeter join, and at $\eta \sim 1.1$,

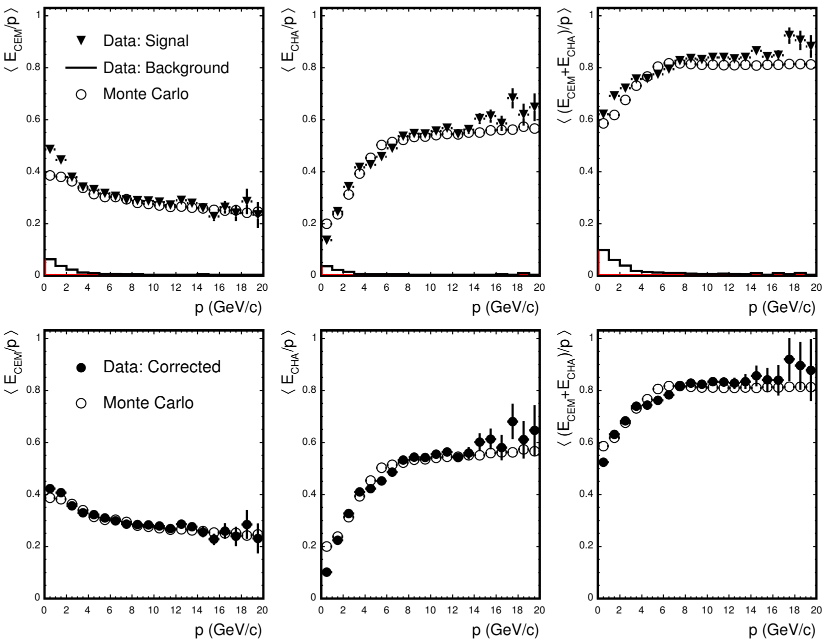

Figure 3.16: E/p observed in the central calorimeter as a function of particle momentum in data and Monte Carlo single track samples.

where the plug and central calorimeters are merged. The η-dependent corrections are obtained by requiring p_T balance of the two leading jets in di-jet events without additional hard QCD radiation. f_η corrections are determined separately for data and Monte Carlo simulated events, and for different p_T^{jet} bins. Residual differences are taken as systematic uncertainties on the correction, the total uncertainty on f_η ranges between 0.5% and 3%. Figure 3.17 shows the values of the correction for jets with radius $R = 0.7$ in data compared to PYTHIA and HERWIG [65] Monte Carlo simulation, the PYTHIA simulation shows a better agreement with data.

- $f_{\mathrm{p\bar{p}I}}$ is a correction to p_T^{jet} which accounts for extra energy in the jet cone coming from multiple $\mathrm{p\bar{p}}$ interactions occurred in the same bunch crossing. Extra $\mathrm{p\bar{p}}$ interactions are identified through the reconstruction of additional vertices, and the amount of transverse energy inside a random cone of radius $R = 0.7$ is parametrized as a function of the number of reconstructed vertices N_V. The average transverse momentum contribution to jets is measured in a minimum bias data sample, as a result an amount of 1.06 ± 0.32 GeV/c is subtracted from p_T^{jet} for each additional vertex in the event.
- f_{jes} is the average absolute jet energy correction applied to compensate the underestimation of the measured transverse momentum of the jets with respect to particle level jets. The correction is obtained from the calorimeter simulation as implemented in the Monte Carlo. For each particle jet, f_{jes} is determined as a function of the p_T^{jet} measured in the calorimeter. Difference in p_T between particle jets and calorimeter jets and values of the correction are shown in Figure 3.18. The uncertainty on the correction is computed from the difference between data and Monte Carlo in the

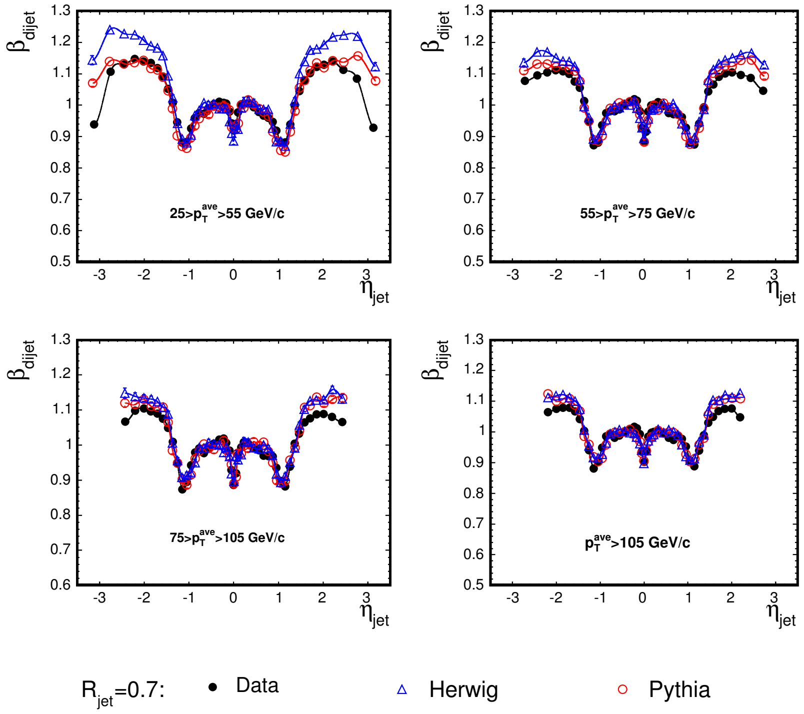

Figure 3.17: Di-jet balance as a function of jet η in data, PYTHIA and HERWIG Monte Carlo samples for different bins of jet p_T. The di-jet balance shows the non-homogeneous response of the calorimeter and the gaps at $\eta = 0$ and $|\eta| = 1.1$, the inverse of the function β_{dijet} is used to estimate the f_η correction.

calorimeter response to single particles. The uncertainty on f_{jes} constitutes the main source to the total jet energy uncertainty.

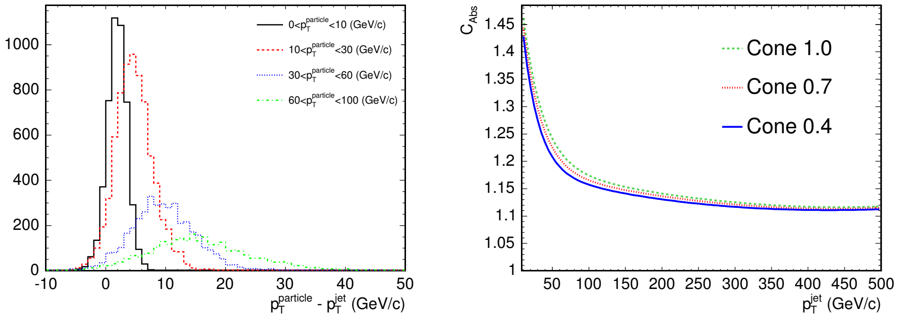

Figure 3.18: (left) p_T differences between particle jets and calorimeter jets for various jet p_T bins, and (right) values of the absolute jet energy correction.

Several tests confirm the validity of the jet energy corrections, among others the γ-jet balance in γ + jet events, and the di-jet balance. Such validations are performed period by period to ensure the stability of the jet corrections with respect to the increase of the instantaneous luminosity. PYTHIA and HERWIG Monte Carlo programs are used in the validation of the jet energy corrections, a good agreement between data and PYTHIA is observed, while HERWIG provides a poorer modeling of some distributions. According to this observation the Monte Carlo used to unfold the Z/γ^* + jets measurement from detector to particle level is based on the PYTHIA simulation of parton shower, hadronization and underlying event, as described in section 4.6.

Chapter 4

Measurement of Z/γ^* + jets production cross sections

The measurement of $Z/\gamma^* \to l^+l^-$ + jets inclusive and differential cross sections requires several analysis steps. High p_T muons and electrons coming from the $Z/\gamma^* \to l^+l^-$ decay are used to trigger Z/γ^* + jets events. The possible interplay between leptons and jets in the l^+l^- + jets final state is taken into account in the reconstruction and identification of leptons and jets physics objects. In order to improve the precision of the measurement trigger and identification efficiencies are measured within the analysis context accounting for run period dependency. The calculation of the efficiencies exploits the presence of pairs of leptons in $Z/\gamma^* \to l^+l^-$ events, and the method employed is validated through the estimation of the inclusive $Z/\gamma^* \to l^+l^-$ production cross section in the electrons and muons channels. The background contribution to the Z/γ^* + jets process is rather small, between 2% and 10%, the subtraction of background processes is done through Monte Carlo and data-driven techniques. Measured cross sections are unfolded back to the particle level using ALPGEN+PYTHIA Monte Carlo sample. Experimental systematic uncertainties are evaluated, the main uncertainty comes from the determination of the jet energy scale. $Z/\gamma^* \to e^+e^-$ and $Z/\gamma^* \to \mu^+\mu^-$ decay channels are combined accounting for the correlation between systematic uncertainties.

4.1 Data sample

The data used in the analysis were collected with the CDF detector between February 2002 and September 2011, and correspond to a total integrated luminosity of ~ 10 fb^{-1}. The data sample is divided in sub-samples corresponding to different run periods as listed in Table 3.2, the sub-samples are enumerated from 0 to 38, except for run period 0 which is called 0d and the run periods from 1 to 4 which are grouped together and called 0h. Events used in the analysis have been collected with a set of high-p_T electron and muon triggers, and the sample is filtered to select only runs of data taking in which all the sub-detectors relevant for the analysis were fully operational. After this preliminary selection the integrated luminosity of the data sample is 9.64 fb^{-1} for the $Z/\gamma^* \to \mu^+\mu^-$ channel and 9.42 fb^{-1} for the $Z/\gamma^* \to e^+e^-$ channel.

Electron trigger	
Level 1	Central electromagnetic cluster • $E_T > 8$ GeV • $E_{HAD}/E_{EM} \leqslant 0.125$ Track matched to the EM cluster • $p_T^{trk} > 8$ GeV/c • Hits in $\geqslant 4$ COT superlayers
Level 2	Central electromagnetic cluster • $E_T > 16$ GeV • $E_{HAD}/E_{EM} \leqslant 0.125$ Track matched to the EM cluster • $p_T^{trk} > 8$ GeV/c • $\eta^{trk} < 1.3$
Level 3	Central electromagnetic cluster • $E_T > 18$ GeV • $E_{HAD}/E_{EM} \leqslant 0.125$ • Lateral Shower $\leqslant 0.4$ Track matched to the EM cluster • $p_T^{trk} > 9$ GeV/c • $z_0 \leqslant 8$ cm from the primary vertex

Table 4.1: Electron trigger selection.

4.1.1 Electron Trigger

The electron trigger requires a cluster of energy in the central electromagnetic calorimeter matched to a reconstructed track, details of the requirements for each trigger level are listed in Table 4.1

The trigger efficiency is evaluated separately for the calorimeter requirements and for the tracking requirements. The efficiency of the calorimeter requirements depends on the E_T of the electron, and for electrons with $E_T \geqslant 25$ GeV, as required in the $Z/\gamma^* \to l^+l^-$ selection of this measurement, it is found to be flat and consistent with 100%. The efficiency of the tracking requirements is evaluated using a sample of $W \to e\nu$ collected with a trigger that has the same calorimeter requirements of the electron trigger used in the analysis and does not have any tracking requirement. The tracking efficiency is then evaluated for each trigger level with the following equations:

$$\epsilon_{L1}^{trk} = \frac{N_W^{\mathrm{L1}}}{N_W}$$

$$\epsilon_{L2}^{trk} = \frac{N_W^{\mathrm{L1+L2}}}{N_W^{\mathrm{L1}}}$$

$$\epsilon_{L3}^{trk} = \frac{N_W^{\mathrm{L1+L2+L3}}}{N_W^{\mathrm{L1+L2}}}$$

The tracking efficiency does not show any dependence with respect to the electron E_T. In order to account for detector aging, and for changes in the trigger requirements, the efficiency is evaluated for each run period. The values used in the analysis are reported in Table 4.3.

	CMUP	CMX
Level 1	CMU-stub • $p_T \geqslant 6$ GeV/c • hits in CMP Track matched to CMU stub • $p_T \geqslant 4$ GeV/c	CMX-stub • $p_T \geqslant 6$ GeV/c Track matched to CMX stub • $p_T \geqslant 8.3$ GeV/c
Level 2	Track matched to CMU-CMP stubs • $p_T \geqslant 14.8$ GeV/c • Hits in $\geqslant 4$ COT superlayers	Track matched to CMX stub • $p_T \geqslant 14.8$ GeV/c • Hits in $\geqslant 4$ COT superlayers
Level 3	Track matched to CMU-CMP stubs • $p_T \geqslant 18$ GeV/c • $\Delta x_{CMU} \leqslant 10$ cm • $\Delta x_{CMP} \leqslant 20$ cm	Track matched to CMX stub • $p_T \geqslant 18$ GeV/c • $\Delta x_{CMX} \leqslant 10$ cm

Table 4.2: Muon trigger requirements.

4.1.2 Muon Trigger

A set of muon triggers corresponding to the central muon subdetectors CMU, CMP and CMX described in section 3.2.5 is used in the analysis. Tracks reconstructed in the muon detectors are called *stubs*, each of the muon triggers requires a stub in at least one of the muon subsystem matched to a reconstructed track in the COT. The CMUP trigger requires a stub both in the CMU and in the CMP detectors, the CMX trigger requires a stub in the CMX detector. The requirements of the muon triggers are described in Table 4.2, the p_T of the stubs in the muon detectors is derived from timing information from the drift chambers.

The muon trigger efficiencies are evaluated within the analysis context to properly account for the correlation between the trigger efficiency itself and the current muon identification selection. Since the trigger requirements underwent a few changes to deal with the increasing instantaneous luminosity of Tevatron collisions, a different efficiency is evaluated for every run period. Events with a reconstructed $Z/\gamma^* \rightarrow \mu^+\mu^-$ in which one muon is fiducial in the CMX chamber and the other is fiducial both in the CMU and in the CMP chambers are selected. The $Z/\gamma^* \rightarrow \mu^+\mu^-$ reconstruction follows the same criteria used in the analysis which is described in section 4.3.2. For each run period, events are divided in three categories depending on which trigger has fired: N^p_{CMUP} are the events which fired the CMUP trigger, N^p_{CMX} the events which fired the CMX trigger, and $N^p_{\text{CMUP-CMX}}$ the events which fired both triggers. An additional complication comes from the fact that the CMX trigger has been operating with dynamic prescale (see section 3.2.7) for a short period, however the effect of such prescale turned out to be negligible.

The Z/γ^* yields for each category correspond to:

$$N^p_{\text{CMUP-CMX}} = \epsilon^p_{\text{CMUP}} \cdot \epsilon^p_{\text{CMX}} \cdot LT^p_{\text{CMX}} \cdot F^p \qquad (4.1)$$

$$N^p_{\text{CMUP}} = \epsilon^p_{\text{CMUP}} \cdot F^p \qquad (4.2)$$

$$N^p_{\text{CMX}} = \epsilon^p_{\text{CMX}} \cdot LT^p_{\text{CMX}} \cdot F^p \qquad (4.3)$$

$$F^p = \mathcal{L}^p \cdot \sigma(Z \rightarrow \mu^+\mu^-) \cdot \mathcal{A} \qquad (4.4)$$

$$p = 0d, 0h, 5-7, 8, 9..., 38$$

where $\mathcal{L}^p$ is the integrated luminosity for run period p, $\sigma(Z \rightarrow \mu^+\mu^-)$ is the inclusive cross section of Z/γ^* production times the $Z/\gamma^* \to \mu^+\mu^-$ branching ratio and $\mathcal{A}$ is the acceptance of the employed $Z/\gamma^* \to \mu^+\mu^-$ reconstruction. LT^p_{CMX} are the *live time* fractions of the CMX trigger which account for the trigger dynamic prescale.

The trigger efficiencies for each run period are evaluated as:

$$\epsilon^p_{\mathrm{CMUP}} = \frac{N^p_{\mathrm{CMUP\text{-}CMX}}}{N^p_{\mathrm{CMX}}} \tag{4.5}$$

$$\epsilon^p_{\mathrm{CMX}} \cdot LT^p_{\mathrm{CMX}} = \frac{N^p_{\mathrm{CMUP\text{-}CMX}}}{N^p_{\mathrm{CMUP}}} \tag{4.6}$$

Notice that the dynamic prescale live time factor LT^p_{CMX} is accounted in the determination of the CMX trigger efficiency. The results are shown in Table 4.3.

4.2 Monte Carlo samples

Monte Carlo simulated samples are used to estimate most of the background contributions and to unfold the $Z/\gamma^* \to l^+l^-$ + jets measured cross sections back to the particle level. In addition, samples of inclusive $Z/\gamma^* \to e^+e^-$ and $Z/\gamma^* \to \mu^+\mu^-$ are used to evaluate the Monte Carlo electron and muon identification efficiencies, such efficiencies are used to evaluate the Data/MC scale factors employed in the unfolding as described in section 4.6. The $Z/\gamma^* \to e^+e^-$ and $Z/\gamma^* \to \mu^+\mu^-$ samples are also used to calculate the acceptance of the employed Z/γ^* selection, which is needed to perform a cross check on the $\sigma(Z/\gamma^* \to l^+l^-)$ inclusive cross section as shown in section 4.5. The integrated luminosities of the Monte Carlo samples used in the analysis are summarized in Table 4.4. All the samples are passed through the CDF detector simulation, GEANT3 [66] is used to simulate the interaction of particles in the Monte Carlo events with the detector. Multiple pp̄ interaction in the same bunch crossing are simulated with PYTHIA v6.2.16 [29].

- $Z/\gamma^* \to l^+l^-$ + jets
  ALPGEN v2.14 [35] interfaced to PYTHIA v6.4.26 [29] with Tune Perugia 2011 parameters [31], MSTW2008 NLO PDF set [67] for the matrix elements and α_s-matched settings [34] is used to simulate $Z/\gamma^* \to l^+l^-$ + jets signal events. Samples are generated for Z/γ^* + 0, 1, 2, 3, and $\geqslant 4$ jets and matched to PYTHIA showering with the MLM matching procedure [37] to remove phase space overlap between matrix elements and parton showers. The sample is reweighted in the number of extra pp̄ interactions to match the luminosity profile in data using the method described in section 4.6.3.

- $Z/\gamma^* \to e^+e^-$ and $Z/\gamma^* \to \mu^+\mu^-$
  PYTHIA v6.2.16 [29] Tune AW [32] samples of $Z/\gamma^* \to e^+e^-$ and $Z/\gamma^* \to \mu^+\mu^-$ inclusive production are used to evaluate the electron and muon identification efficiencies in Monte Carlo. These efficiencies are combined into $Z/\gamma^* \to e^+e^-$ and $Z/\gamma^* \to \mu^+\mu^-$ reconstruction efficiencies and used to evaluate the Data/MC scale factors needed for the unfolding. The $Z/\gamma^* \to e^+e^-$ and $Z/\gamma^* \to \mu^+\mu^-$ samples are also used to calculate the acceptance of the employed Z/γ^* selection, which is needed to perform a cross check on the $\sigma(Z/\gamma^* \to l^+l^-)$ inclusive cross section.

- ZZ, WZ and ZZ
  Diboson production is considered as a background contribution to the $Z/\gamma^* \to l^+l^-$

Run period	$\epsilon_{\text{electron}}$	ϵ_{CMUP}	ϵ_{CMX}
0d	0.962 ± 0.007	0.832 ± 0.009	0.963 ± 0.005
0h	0.976 ± 0.006	0.834 ± 0.007	0.867 ± 0.007
5-7	0.979 ± 0.004	0.834 ± 0.009	0.856 ± 0.009
8	0.959 ± 0.007	0.857 ± 0.011	0.857 ± 0.011
9	0.960 ± 0.002	0.826 ± 0.012	0.790 ± 0.013
10	0.959 ± 0.002	0.793 ± 0.010	0.853 ± 0.009
11	0.961 ± 0.004	0.777 ± 0.011	0.830 ± 0.010
12	0.960 ± 0.003	0.767 ± 0.014	0.786 ± 0.014
13	0.957 ± 0.003	0.749 ± 0.011	0.783 ± 0.011
14	0.960 ± 0.030	0.803 ± 0.027	0.799 ± 0.027
15	0.963 ± 0.005	0.776 ± 0.014	0.822 ± 0.013
16	0.961 ± 0.005	0.737 ± 0.019	0.833 ± 0.017
17	0.962 ± 0.003	0.763 ± 0.013	0.838 ± 0.012
18	0.962 ± 0.003	0.757 ± 0.009	0.836 ± 0.008
19	0.962 ± 0.003	0.759 ± 0.012	0.812 ± 0.012
20	0.959 ± 0.003	0.752 ± 0.012	0.827 ± 0.011
21	0.958 ± 0.002	0.750 ± 0.009	0.829 ± 0.008
22	0.958 ± 0.003	0.753 ± 0.011	0.846 ± 0.010
23	0.960 ± 0.003	0.751 ± 0.013	0.815 ± 0.012
24	0.960 ± 0.003	0.732 ± 0.012	0.806 ± 0.011
25	0.960 ± 0.003	0.733 ± 0.013	0.792 ± 0.012
26	0.953 ± 0.003	0.761 ± 0.015	0.763 ± 0.015
27	0.952 ± 0.003	0.765 ± 0.009	0.795 ± 0.009
28	0.950 ± 0.003	0.733 ± 0.012	0.794 ± 0.011
29	0.950 ± 0.003	0.747 ± 0.010	0.778 ± 0.010
30	0.946 ± 0.003	0.723 ± 0.010	0.748 ± 0.009
31	0.943 ± 0.007	0.729 ± 0.015	0.740 ± 0.015
32	0.939 ± 0.007	0.712 ± 0.010	0.749 ± 0.010
33	0.941 ± 0.007	0.714 ± 0.011	0.723 ± 0.011
34	0.941 ± 0.007	0.722 ± 0.010	0.762 ± 0.010
35	0.937 ± 0.007	0.720 ± 0.011	0.743 ± 0.011
36	0.940 ± 0.007	0.704 ± 0.011	0.729 ± 0.011
37	0.941 ± 0.007	0.736 ± 0.016	0.717 ± 0.016
38	0.940 ± 0.007	0.723 ± 0.014	0.717 ± 0.014

Table 4.3: Trigger efficiencies of the electron, CMUP and CMX triggers. Only the tracking efficiency is considered for the electron trigger.

Physic process	Monte Carlo generator	Integrated luminosity
$Z/\gamma^* \to e^+e^-$ + jets	ALPGEN+PYTHIA Tune Perugia 2011	37.6 fb^{-1}
$Z/\gamma^* \to \mu^+\mu^-$ + jets	ALPGEN+PYTHIA Tune Perugia 2011	38.5 fb^{-1}
$Z/\gamma^* \to e^+e^-$	PYTHIA Tune AW	60.3 fb^{-1}
$Z/\gamma^* \to \mu^+\mu^-$	PYTHIA Tune AW	60.4 fb^{-1}
ZZ	PYTHIA Tune A	21.6×10^3 fb^{-1}
WZ	PYTHIA Tune A	28.8×10^3 fb^{-1}
WW	PYTHIA Tune A	6×10^3 fb^{-1}
$t\bar{t}$	PYTHIA Tune AW	860 fb^{-1}
$Z/\gamma^* \to \tau^+\tau^-$ + jets	ALPGEN+PYTHIA Tune BW	36.0 fb^{-1}

Table 4.4: Monte Carlo samples.

+ jets process. ZZ, WZ, and WW processes are simulated with PYTHIA v6.2.16 Tune A [32] Monte Carlo.

- $t\bar{t}$
  $t\bar{t}$ production is a source of background for the $Z/\gamma^* \to l^+l^-$ + jets process when an electron-positron pair or a muon anti-muon pair originates from the leptonic decay of the W bosons. The $t\bar{t}$ process is simulated with PYTHIA v6.2.16 Tune AW [32] Monte Carlo, with PARP(91) parameter set to 2.5, and the top mass set to 172.5 GeV/c^2.

- $Z/\gamma^* \to \tau^+\tau^-$ + jets
  ALPGEN v2.10' interfaced to PYTHIA v6.3.25 with Tune BW [32] and CTEQ5L PDF set [68] is used to simulate the background contribution of $Z/\gamma^* \to \tau^+\tau^-$ + jets events.

4.3 Event selection

The data samples collected with the electron and muon triggers are analysed to reconstruct and identify the physical objects of the Z/γ^* + jets final state: the electrons and muons, the Z/γ^* boson and the jets. All the events are required to have at least one reconstructed primary interaction vertex with z position within 60 cm from the center of the detector. The acceptance of the primary vertex requirement is $97.7 \pm 1.0\%$. Since the Monte Carlo samples are filtered requiring a generated primary vertex to be within 60 cm, the acceptance of the primary vertex requirement can be applied directly as a Data/MC scale factor in the unfolding.

4.3.1 Lepton selection

Z/γ^* boson candidates are reconstructed with two high-p_T electrons or muons in the central region of the detector ($|\eta| < 1.0$). Leptons are required to have p_T or $E_T \geqslant 25$ GeV, and the invariant mass M_{ll} has to be within 66 and 116 GeV/c^2.

$\vert\eta\vert$	$\leqslant 1$
E_T	$\geqslant 25$ GeV
Track p_T	$\geqslant 10\ GeV/c$
Track $\vert z_0\vert$	$\leqslant 60$ cm

Table 4.5: Electron kinematic requirements.

Electron identification	
COT Ax & St Layers	$\geq 3\vert\geq 2$
$E_{\mathrm{HAD}}/E_{\mathrm{EM}}$	$\leq 0.055 + (0.00045 \cdot E)$
E/p	≤ 2 or $p_T \geq 50\ GeV/c$
Lateral Shower	≤ 0.2
CES strip χ^2	≤ 10
Signed CES ΔX	$-3 \leq Q \cdot \Delta X \leq 1.5$
CES $\vert\Delta Z\vert$	≤ 3 cm

Table 4.6: Electron identification requirements.

Electron identification

All electrons are required to have $E_T \geqslant 25$ GeV, $|\eta| \leqslant 1.0$ and an associated track with $p_T \geqslant 10$ GeV/c and $|z_0| \leqslant 60$ cm. The kinematic cuts for the electron selection are summarized in Table 4.5.

Table 4.6 describes the details of the identification requirements. Commonly electron identification enforce a requirement on the isolation of the electron with respect to the energy deposited in the calorimeter in a cone around the candidate electron. Such isolation cut is not applied in this analysis to avoid loosing efficiency in events with high jet multiplicity or when the Z/γ^* boson is highly boosted.

The electron energy is reconstructed summing the energy of the calorimeter towers that form the electron cluster as described in section 3.3.1, after this reconstruction the electron energy is corrected for several effects:

- A *face correction* accounts for different response from wedge to wedge. The correction was determined mapping the response across the wedge using test beam data.
- The energy deposit in the pre-radiator is added to the energy measured in the calorimeter.
- The fraction of the energy which is expected to be deposited outside the cluster is added. This correction depends on the position of the center of the electron shower in the calorimeter cluster.

To account for residual differences between data and simulation in the electron E_T scale a run period dependent correction has been evaluated. Data are corrected with an E_T scale factor:

$$E_T \rightarrow E_T \cdot S_e \tag{4.7}$$

Values for the E_T scale correction S_e are evaluated considering data and Monte Carlo $Z/\gamma^* \rightarrow e^+e^-$ invariant mass spectra within the range $84 \div 98$ GeV/c^2. The Monte Carlo is left uncorrected, while for each run period a set of spectra is generated applying the E_T scale correction at different values from 1.00 to 1.03. For each run period a χ^2 is evaluated as a function of S_e according to the following equation:

$$\chi^2_p = \sum_i^{\text{Mass bins}} \left(\frac{N^i_{\text{Data p}} - N^i_{MC}}{\sqrt{N^i_{\text{Data p}}}}\right)^2 \tag{4.8}$$

When evaluating the χ^2 the Monte Carlo spectrum is normalized to the area of the data spectrum. The χ^2 distributions as a function of S_e for the different run periods are fitted with a second degree polynomial function $a \cdot x^2 + b \cdot x + c$. The best value for the correction is given by the minimum $\frac{-b}{2 \cdot a}$, and the uncertainty by $\frac{1}{\sqrt{a}}$ which is the half width of the curve at minimum +1. Results are shown in Figure 4.1, an improvement in the calibration method of the CEM energy leads to lower values of S_e starting from run period 18.

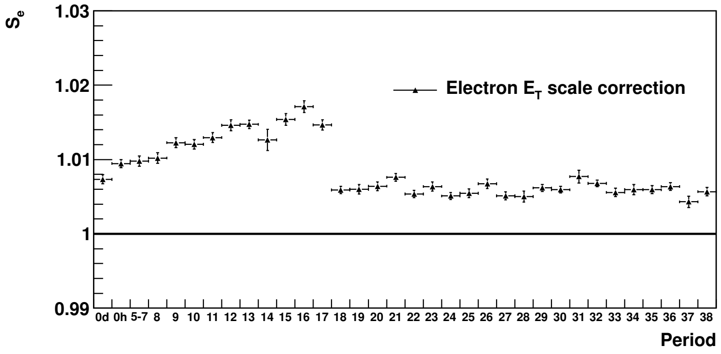

Figure 4.1: Electrons E_T scale correction parameters as a function of run period.

The electron identification efficiencies and Data/MC scale factors are evaluated for the current selection requirements and in the same lepton kinematic region used for the measurement. The efficiencies are evaluated using the "lepton counting method" on a sample of $Z/\gamma^* \rightarrow e^+e^-$ events. A tag leg is defined as a CEM electron passing the kinematics and identification requirements of Tables 4.5, 4.6, a further isolation requirement $E_T(\Delta R < 0.4)/E_T(e) \leqslant 0.05$, a tighter E over p requirement $E/p \leqslant 1.2$ and a tighter requirement on Lateral Shower energy $\leqslant 0.1$. A probe leg is an electron passing the kinematic requirements of Table 4.5, and associated to a tag electron so that the tag-probe electrons couple has invariant mass within $86 - 96$ GeV/c^2. Background from W + jets events is reduced requiring $\not{E}_T \leqslant 20$ GeV. All events having at least one tag-probe couple are selected, and all probe legs are considered for the efficiency calculation. Notice that it is possible to have two probe legs per event, when the two electrons pass both the tag and the probe selection. The efficiencies are evaluated as:

$$\epsilon_{ID} = \frac{N_{\text{ID}}}{N_{\text{probe}}} \tag{4.9}$$

where N_{probe} is the number of probe legs, and N_{ID} is the subset of probe legs which pass the considered identification selection. A different identification efficiency is evaluated for every run period, the results are shown in Figure 4.2. The efficiency of each selection requirement for the whole dataset are reported in Table 4.7.

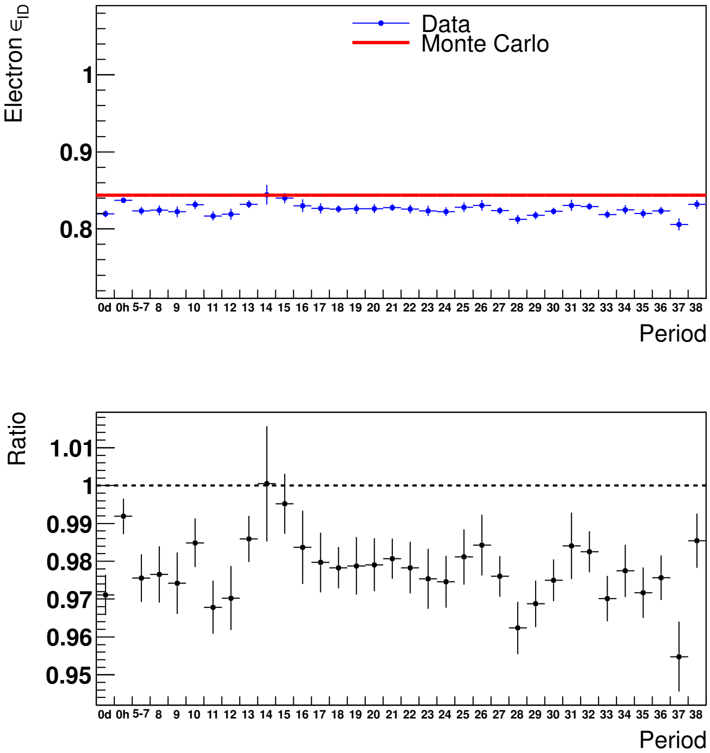

Figure 4.2: Electron identification efficiencies and Data/MC scale factors as a function of run period.

Requirement	Efficiency
COT Ax ≥ 3 and St Layers ≥ 2	99.38 ± 0.02
$E_{\mathrm{HAD}}/E_{\mathrm{EM}} \leq 0.055 + (0.00045 \cdot E)$	99.25 ± 0.02
$E/p \leq 2$ or $p_T \geq 50\ GeV/c$	90.88 ± 0.07
Lateral Shower ≤ 0.2	98.74 ± 0.03
CES strip $\chi^2 \leq 10$	95.96 ± 0.05
Signed CES ΔX $-3 \leq Q \cdot \Delta X \leq 1.5$	97.91 ± 0.04
CES $\lvert\Delta Z\rvert \leq 3$ cm	99.20 ± 0.02
Total electron ϵ_{ID}	82.51 ± 0.10

Table 4.7: Efficiencies of the electron identification requirements.

Muon identification

Muons are reconstructed from tracks in the COT and silicon subdetectors, as described in section 3.3.2, and divided in three categories: CMUP, CMX and stubless (CMIO) muons. Muons enter the CMUP category when the associated track extrapolates to the CMU and CMP muon detectors, CMX when the track extrapolates to the CMX detector, and stubless when the extrapolated track does not cross any of the muon detectors. This categorization allows to associate at least one muon of a $Z/\gamma^* \to \mu^+\mu^-$ event to the corresponding muon trigger: events triggered with the CMUP(CMX) trigger are required to have at least one CMUP(CMX) muon. Figure 4.3 shows the muon distribution in the $\eta - \phi$ plane for the three categories.

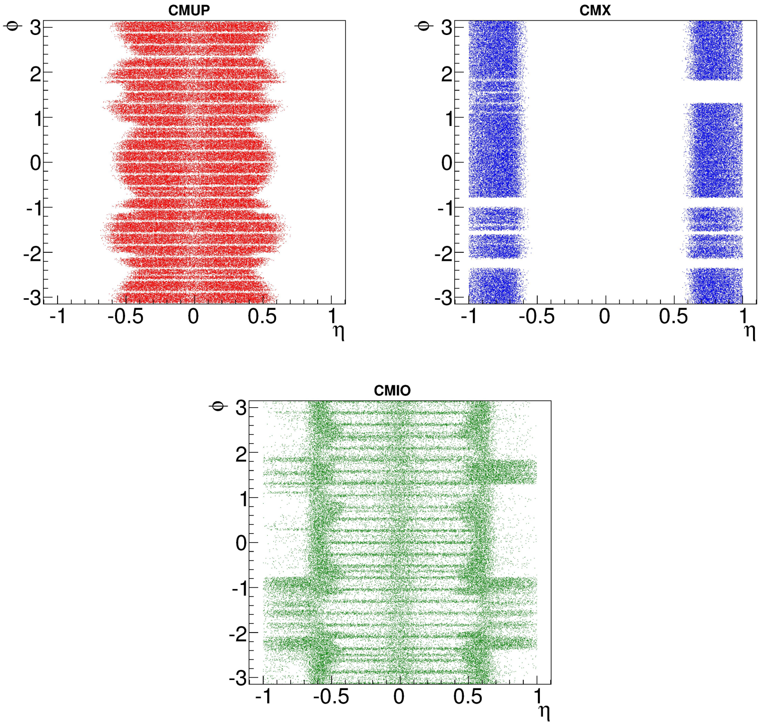

Figure 4.3: Muons geometry in the $\eta - \phi$ plane for CMUP, CMX and stubless (CMIO) muons. Events are required to pass the $Z/\gamma^* \to \mu^+\mu^-$ reconstruction.

All Muons are required to have $p_T \geqslant 25$ GeV/c and $|\eta| \leqslant 1$, and to cross all the SL of the COT[1]. The kinematic cuts for the muon selection are summarized in Table 4.8.

To account for difference between data and simulation in the muon p_T resolution and scale a run period dependent correction is evaluated. Monte Carlo simulation is corrected with a gaussian smearing on the curvature:

$$\frac{1}{p_T} \to \frac{1}{p_T} + f \tag{4.10}$$

---

[1] muon tracks are required to have an exit radius at the COT edge $z_{COT} = 155$ cm larger than the COT radius $r_{COT} = 140$ cm

	CMUP, CMX and CMIO muons
$\eta - \phi$	see Fig 4.3
$\|\eta\|$	$\leqslant 1$
p_T	> 25 GeV/c
$\|z_0\|$	< 60 cm
$\rho_{COT} =$ $= (155 \cdot \mathrm{sign}(\eta) - \mathrm{z}_0) \cdot \tan(\theta)$	$\geqslant 140$ cm (COT outer radius)

Table 4.8: Kinematic requirements for CMUP, CMX and stubless (CMIO) muons.

where f is a random value of a gaussian spectrum of mean 0 and width σ. Data are corrected with a scale factor:

$$p_T \to p_T \cdot C \tag{4.11}$$

Values for the p_T smearing correction σ and the p_T scale correction C are evaluated with the same method used for the electrons. Data and Monte Carlo $Z/\gamma^* \to \mu^+\mu^-$ invariant mass spectra within the range $84 \div 98$ GeV/c^2 are considered. Data are subdivided by run period and left uncorrected, while two sets of Monte Carlo spectrum are generated applying separately the smearing correction and the inverse of the p_T scale correction at different values. For each run period the χ^2 is evaluated separately as a function of σ and C according to:

$$\chi^2_p = \sum_i^{\text{Mass bins}} \left(\frac{N^i_{\text{Data p}} - N^i_{MC}}{\sqrt{N^i_{\text{Data p}}}}\right)^2 \tag{4.12}$$

As for the electrons, when evaluating the χ^2 the Monte Carlo spectra are normalized to the area of the data spectrum. The χ^2 distribution as a function of σ and C for the different run periods are fitted with a second degree polynomial function $a \cdot x^2 + b \cdot x + c$. The best value for the correction is given by the minimum $\frac{-b}{2 \cdot a}$, and the uncertainty by $\frac{1}{\sqrt{a}}$ which is the half width of the curve at minimum +1. Results are shown in Figure 4.4.

The p_T scale correction is found to be run period independent, for this reason the procedure is repeated evaluating one global correction on the full dataset. The resulting value is 1.00138 ± 0.00009. The p_T smearing correction distribution versus run period is fitted with a linear distribution to evaluate the value of this correction for each run period. The smearing function applied to Monte Carlo samples is generated in two steps: first a run period is selected picking up a random value from a step function representing the luminosity fraction of each run period: $l(p) = \frac{L_p}{L_{Tot}}$. Then a gaussian smearing function with σ corresponding to the selected run period is generated, and a random value from this distribution is applied as a correction to the muon p_T.

Muon are identified requiring that the energy deposit in calorimeter towers crossed by the track associated to the muon is compatible with a minimum ionizing particle. The track is also required to originate from the primary vertex and to pass quality requirement on the number of hits and fit χ^2. The details of the identification requirement applied to all the muon categories are reported in Table 4.9. Calorimeter isolation of muons is not required to avoid loosing efficiency in events with a high jet multiplicity environment. Requirements on COT χ^2, number of hits, and number of transitions in the track fit residuals are tuned to reject most of the decay in flight (DIF) component of the fakes background.

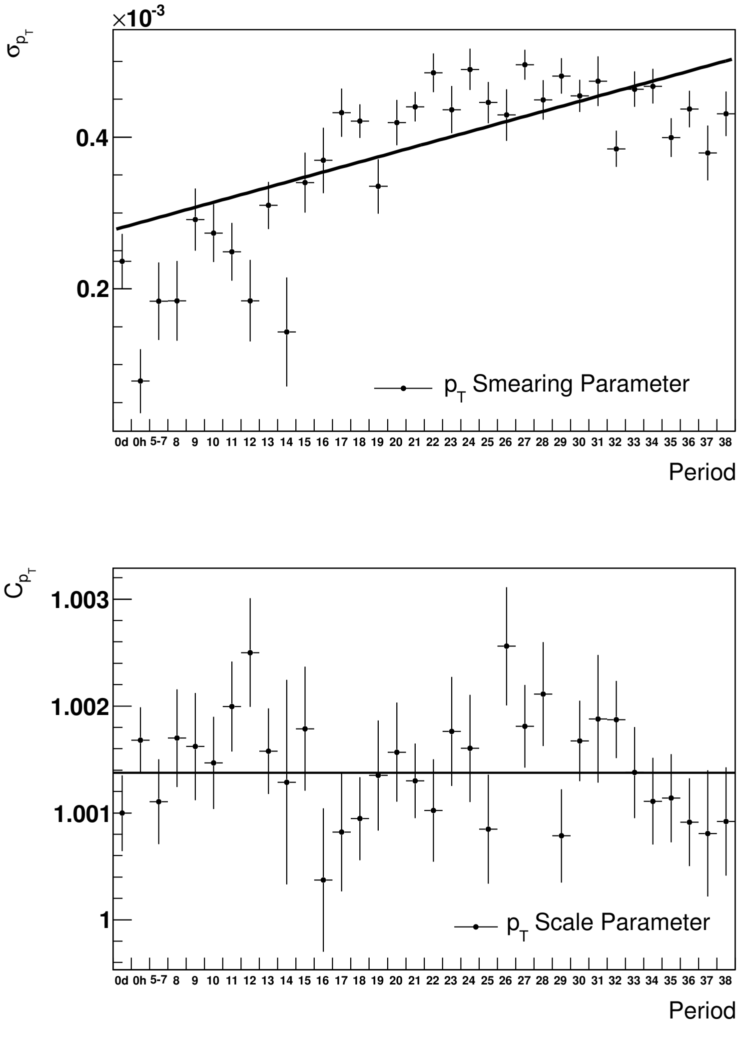

Figure 4.4: Scale and smearing parameters for the muon p_T correction as a function of run period.

Muon identification	
E_{EM}	$\leqslant 2 + \max(0, (\text{p} - 100) \cdot 0.0115)$ GeV
E_{HAD}	$\leqslant 6 + \max(0, (\text{p} - 100) \cdot 0.028)$ GeV
$\lvert d_0 \rvert$ no Si	$\leqslant 0.2$ cm
$\lvert d_0 \rvert$ Si Tracks	$\leqslant 0.02$ cm
Axial COT SL with ≥ 5 hits	≥ 2
Stereo COT SL with ≥ 5 hits	≥ 2
COT χ^2/n.d.f.	$\leqslant 4$
COT hits	$\geqslant 55$
transitions in COT hits residuals	$\geqslant 20$

Table 4.9: Identification requirements for CMUP, CMX and stubless muons.

	CMUP	CMX
CMU $\lvert\Delta x\rvert$	< 7 cm	-
CMP $\lvert\Delta x\rvert$	< 5 cm	-
CMX $\lvert\Delta x\rvert$	-	< 6 cm

Table 4.10: Stub requirements for CMUP and CMX muons (used only for the identification efficiency calculation).

As for the electrons, the muon identification efficiencies and Data/MC scale factors are evaluated for the current selection requirements and in the same lepton kinematic region used for the measurement. The same "lepton counting method" used for the electron efficiencies is employed on a sample of $Z/\gamma^* \to \mu^+\mu^-$ events. A tag leg is defined as a muon passing the kinematics and identification requirements of Tables 4.8, 4.9. In addition the tag leg is required to be linked to a stub in the muon system according to the match requirements in Table 4.10, and to fulfill a calorimeter isolation cut $E_T(\Delta R < 0.4)/p_T(\mu) \leqslant 0.1$. A probe leg is a muon passing the kinematic requirements of Table 4.8, and associated to a tag muon so that the tag-probe muons couple has invariant mass within $81 - 101$ GeV/c^2, opposite charge tracks and $\lvert\Delta Z_0\rvert \leqslant 4$ cm. If the 3D opening angle α of the muon pair is $\geqslant 3.1$ rad at least one of the two legs is required not to be tagged as a cosmic muon according to COT timing criteria. All events having at least one tag-probe couple are selected, and all probe legs are considered for the efficiency calculation. Notice that it is possible to have two probe legs per event, when the two muons pass both the tag and the probe selection.

The efficiencies are then defined as:

$$\epsilon_{ID} = \frac{N_{\text{ID}}}{N_{\text{probe}}} \tag{4.13}$$

where N_{probe} is the number of probe legs, and N_{ID} is the subset of probe legs which pass the considered identification selection. The muon efficiencies are combined into Z/γ^* reconstruction efficiencies and then a scale factor for each Z/γ^* category is evaluated, as described in section 4.3.2.

Since the identification efficiencies for the three muons categories turned out to be consistent within the statistical error, an overall identification efficiency is evaluated. A different identification efficiency is evaluated for every run period, the results are shown in

Figure 4.5. The efficiency of each selection requirement for the whole dataset are reported in Table 4.11.

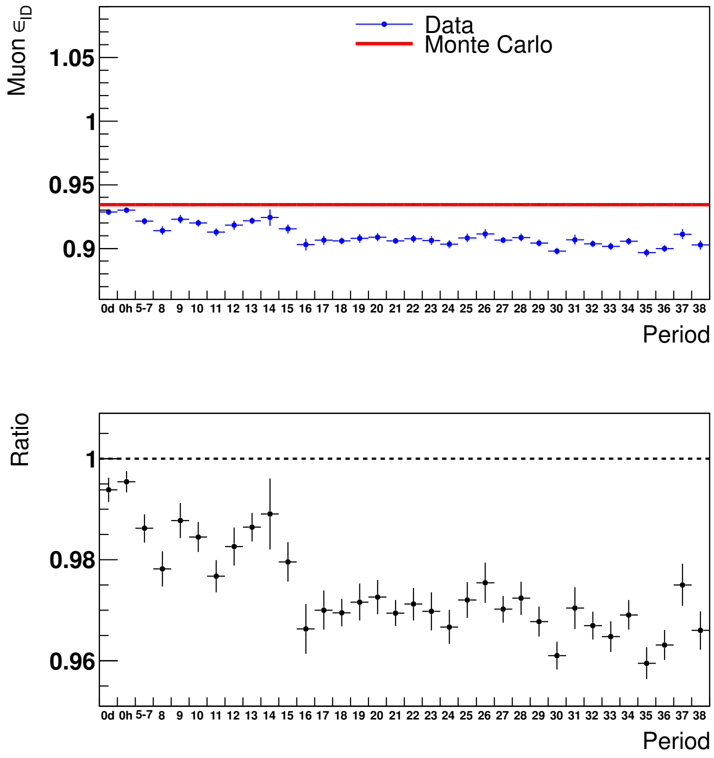

Figure 4.5: Muon identification efficiencies and Data/MC scale factors as a function of run period.

4.3.2 $Z/\gamma^* \to l^+l^-$ reconstruction and selection

Electrons and muons passing the identification requirements are used to reconstruct Z/γ^* candidates following a $Z/\gamma^* \to l^+l^-$ reconstruction algorithm. The highest p_T identified electron or muon compatible with the trigger associated to the event is selected, in $Z/\gamma^* \to \mu^+\mu^-$ events such first muon can be either a CMUP or CMX but not a CMIO. Then the highest p_T identified lepton of the same flavour other than the first is selected. The leptons pair is considered as a candidate $Z/\gamma^* \to l^+l^-$ boson and the event is selected if the reconstructed Z/γ^* boson has an invariant mass within $66 - 116$ GeV/c^2. In the case of muons the associated tracks are also required to have opposite charge. Reconstructed $Z/\gamma^* \to l^+l^-$ events are divided in one $Z/\gamma^* \to e^+e^-$ electron category and five $Z/\gamma^* \to \mu^+\mu^-$ categories depending on which category the two leptons belong to: CEM-CEM refers to the $Z/\gamma^* \to e^+e^-$ category, CMUP-CMUP, CMX-CMX, CMUP-CMX, CMUP-CMIO, CMX-CMIO are the $Z/\gamma^* \to \mu^+\mu^-$ categories. Z/γ^* reconstruction efficiencies and Data/MC scale factors are evaluated for each category and for each run period combining

Requirement	Efficiency
$E_{EM} \leqslant 2 + \max(0, (\mathrm{p} - 100) \cdot 0.0115)$ GeV	$96.48 \pm 0.03\%$
$E_{HAD} \leqslant 6 + \max(0, (\mathrm{p} - 100) \cdot 0.028)$ GeV	$97.52 \pm 0.03\%$
$\lvert d_0 \rvert \leqslant 0.02(0.2)$ cm Si Tracks(no Si)	$98.02 \pm 0.03\%$
Axial and Stereo COT SL with ≥ 5 hits ≥ 2	$99.99 \pm 0.00\%$
COT χ^2/n.d.f. $\leqslant 4$	$99.33 \pm 0.01\%$
COT hits $\geqslant 55$	$99.12 \pm 0.02\%$
transitions in COT hits residuals $\geqslant 20$	$97.83 \pm 0.03\%$
Total muon ϵ_{ID}	$91.01 \pm 0.05\%$

Table 4.11: Efficiencies of the muon identification requirements.

Z/γ^* category		Trigger efficiency
$Z/\gamma^* \to e^+e^-$	CEM-CEM	$\epsilon_{\mathrm{electron}} \cdot (2 - \epsilon_{\mathrm{electron}})$
$Z/\gamma^* \to \mu^+\mu^-$	CMUP-CMUP	$\epsilon_{\mathrm{CMUP}} \cdot (2 - \epsilon_{\mathrm{CMUP}})$
	CMX-CMX	$LT_{\mathrm{CMX}} \cdot \epsilon_{\mathrm{CMX}} \cdot (2 - \epsilon_{\mathrm{CMX}})$
	CMUP-CMX	$\epsilon_{\mathrm{CMUP}} + LT_{\mathrm{CMX}} \cdot \epsilon_{\mathrm{CMX}} \cdot (1 - \epsilon_{\mathrm{CMUP}})$
	CMUP-CMIO	ϵ_{CMUP}
	CMX-CMIO	$LT_{\mathrm{CMX}} \cdot \epsilon_{\mathrm{CMX}}$

Table 4.12: Trigger efficiencies of Z/γ^* reconstruction.

the trigger and lepton identification efficiencies reported in Table 4.3, Figure 4.2 and Figure 4.5. Trigger efficiencies formulas are reported in Table 4.12.

4.3.3 Jet reconstruction and selection

As described in section 3.3.4 jets are reconstructed with the Run II CDF midpoint algorithm in a cone radius $R = 0.7$ and with the merging/splitting fraction set to $f = 0.75$. The jets are clustered using calorimeter towers with transverse energy above 0.1 GeV and seeds of 1 GeV, towers associated to reconstructed and identified electrons and muons are excluded from the jet clustering. The measured jet transverse momenta are corrected to particle level using the method described in [63], after these corrections jets with $p_T^{\mathrm{jet}} > 30$ GeV/c and $|y^{\mathrm{jet}}| < 2.1$ are selected. A minimum distance between the jets and the leptons $\Delta R_{l-\mathrm{jet}} > 0.7$ is also required. The jet shapes in the region $p_T > 30$ GeV/c are properly described by PYTHIA Tune A and Tune Perugia 2011 as shown in [69] and [34], jets in the rapidity range $|y^{\mathrm{jet}}| < 2.1$ have limited contributions from proton/antiproton remnants. As shown in [70] the value $R = 0.7$ for the jet radius minimises the non-perturbative contributions from hadronization and underlying event at the Tevatron center-of-mass energy.

4.4 Background estimation

Background estimation is done both with Monte Carlo and data driven techniques. QCD and W + jets backgrounds are estimated using a data-driven method, other background contributions coming from electroweak processes and $t\bar{t}$ events are estimated using Monte

Carlo samples. The sources of backgrounds considered are ZZ, ZW, WW diboson production, $t\bar{t}$ production and $Z/\gamma^* \to \tau^+\tau^-$ + jets. The Monte Carlo samples used to simulate background processes are described in section 4.2, the samples are normalized to the NLO cross section.

4.4.1 QCD and W + jets backgrounds

QCD multi-jet events contribute to the background when two hadronic jets are misidentified as leptons, while in W + jets background events one of the two identified lepton is a real lepton from the W leptonic decay, and the other is a hadronic jet.

Two different data-driven methods are used to estimate the QCD and W + jets background in the $Z/\gamma^* \to e^+e^-$ and $Z/\gamma^* \to \mu^+\mu^-$ decay channels. In the electron channel the background is estimated measuring the electron fake rate, that is the probability of a jet to be identified as an electron. After evaluating the fake rate in a jet data sample, a prediction of the total background contribution is obtained applying the measured fake rate to a W + jets events sample.

The QCD and W + jets background in the muon channel is estimated with a sample of events selected with the same requirements of the analysis described in section 4.3, but instead of requiring the two muon tracks to be opposite charged, they are required to be same charged. The same charge events yield is then directly considered as the background estimation for QCD and W + jets.

Electron fake rate

Fake electrons are hadronic jets which are incorrectly identified as electrons, and the fake rate is defined as the probability of a jet to be matched to an electron object which passes all the requirements of the electron identification. Jets are selected in the same kinematic region of the corresponding electron objects: $E_T \geqslant 25$ GeV, $|y| \leqslant 1.0$ and at least one track with $p_T \geqslant 10$ GeV/c matched to the jet. The energy corrections described in section 3.3.4 are not applied to the jets, instead the E_T of the jet is scaled and smeared to model the energy of a corresponding electron. In fact due to the difference in the reconstruction algorithms of jets and electrons, a jet of a given E_T corresponds to a fake electron of lower energy. The energy scaling between jets and electrons is evaluated matching jets and electron objects in the same sample used to evaluate the fake rate. The difference in energy is shown in Figure 4.6(right), a gaussian fit is used to model the correction which has been applied to jets. The fake rate is measured on a jet sample collected with a trigger which requires at least a jet with $E_T \geqslant 20$ GeV. Events with more than one electron or $\not{E}_T > 15$ GeV are excluded to reject real electrons coming from the decays of Z/γ^* and W bosons. The result is shown in Figure 4.6(left), an exponential fit is used to model the fake rate.

QCD and W + jets background estimation in the $Z/\gamma^* \to e^+e^-$ channel

Once the fake rate is obtained, the electron sample is used to estimate the QCD and W + jets background. W + jets events with exactly one reconstructed central electron are selected, and each electron-jet pair which fulfills the Z/γ^* kinematic requirements of the measurement is considered as a $Z/\gamma^* \to e^+e^-$ candidate. The background estimation is obtained assigning to each electron-jet candidate the fake probability associated to the jet, corrected for the probability of the other jets in the event to fail the electron identification.

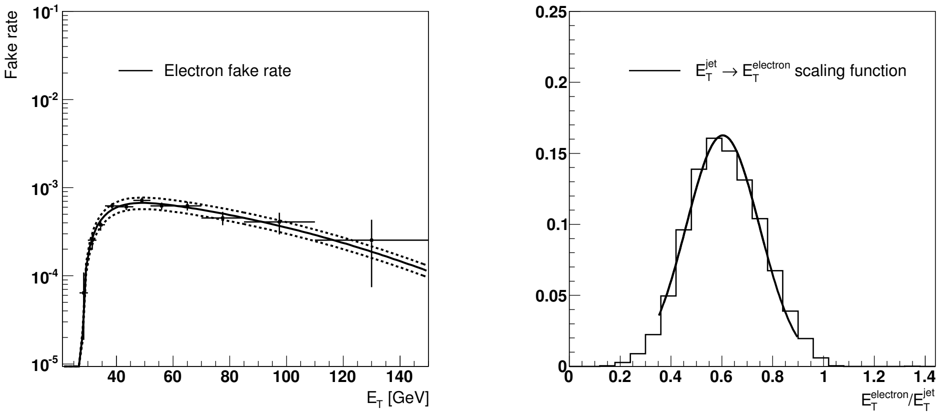

Figure 4.6: (left) Electron fake rate as a function of electron E_T, the dashed lines correspond to the associated uncertainty of 15%. (right) Scaling of jet E_T to the corresponding fake electron E_T.

4.4.2 Background expectation

The numbers of estimated events for each background in the $Z/\gamma^* \rightarrow e^+e^-$ and $Z/\gamma^* \rightarrow \mu^+\mu^-$ channels are summarized in Tables 4.13 and 4.14.

CDF Run II Preliminary

$Z/\gamma^* \rightarrow e^+e^-$ + jets				
Backgrounds	**Estimated events in** 9.42 fb^{-1}			
	Z + $\geq$ 1 jet	**Z + $\geq$ 2 jets**	**Z + $\geq$ 3 jets**	**Z + $\geq$ 4 jets**
QCD, W + jets	25.8 ± 3.9	4.0 ± 0.6	0.6 ± 0.1	0.1 ± 0.0
WW, ZZ, ZW	119 ± 36	43.2 ± 12.9	4.2 ± 1.3	0.3 ± 0.1
$t\bar{t}$	44.7 ± 13.4	25.4 ± 7.6	2.9 ± 0.9	0.2 ± 0.1
$Z/\gamma^* \rightarrow \tau^+\tau^-$ + jets	7.2 ± 2.2	0.5 ± 0.1	0.0 ± 0.0	0.0 ± 0.0
Total Background	197 ± 38	73.1 ± 15.0	7.8 ± 1.5	0.6 ± 0.1
Data	12883 ± 114	1446 ± 38	136 ± 11.7	13 ± 3.6

Table 4.13: Estimated background events in 9.42 fb^{-1} for $Z/\gamma^* \rightarrow e^+e^- + \geqslant 1$, 2, 3 and 4 jets compared to data yield.

The accuracy of the background estimation is checked comparing the Z/γ^* invariant mass spectrum of data and signal plus background in the side bands outside the Z mass peak, which are mostly populated by background events. Figures 4.7 and 4.8 show the comparison for $Z/\gamma^* \rightarrow l^+l^- + \geqslant 1$ jet and $Z/\gamma^* \rightarrow l^+l^- + \geqslant 2$ jets events.

CDF Run II Preliminary

$Z/\gamma^* \rightarrow \mu^+\mu^-$ + jets				
Backgrounds	**Estimated events in** 9.64 fb^{-1}			
	Z + $\geq$ 1 jet	**Z + $\geq$ 2 jets**	**Z + $\geq$ 3 jets**	**Z + $\geq$ 4 jets**
QCD, W + jets	51.0 ± 51.0	18.0 ± 18.0	3.0 ± 3.0	1.0 ± 1.0
WW, ZZ, ZW	180 ± 57	69.1 ± 20.7	6.7 ± 2.0	0.5 ± 0.2
$t\bar{t}$	67.9 ± 20.4	38.1 ± 11.4	4.4 ± 1.3	0.5 ± 0.1
$Z/\gamma^* \rightarrow \tau^+\tau^-$ + jets	9.4 ± 2.8	1.1 ± 0.3	0.1 ± 0.0	0.0 ± 0.0
Total Background	317.8 ± 79.1	126.3 ± 29.7	14.2 ± 3.8	2.0 ± 1.0
Data	19525 ± 140	2235 ± 47	195 ± 14	13.0 ± 3.6

Table 4.14: Estimated background events in 9.64 fb^{-1} for $Z/\gamma^* \rightarrow \mu^+\mu^-$ $+ \geqslant 1$, 2, 3 and 4 jets compared to data yield.

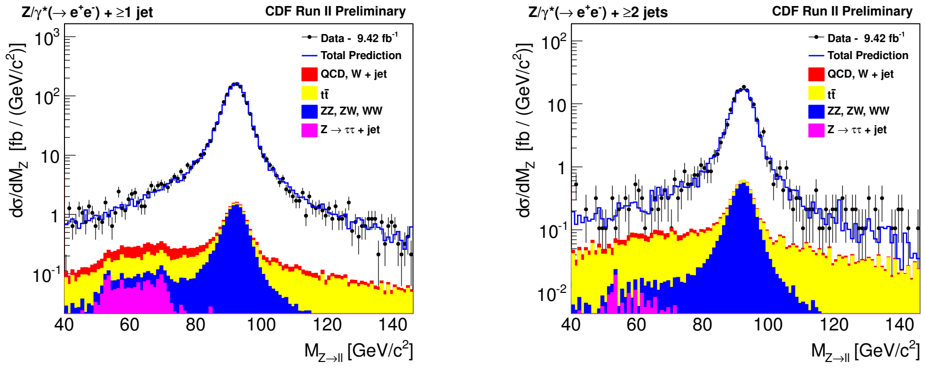

Figure 4.7: Data and signal plus background estimation within Z mass window and on side bands, in (left) $Z/\gamma^* \rightarrow e^+e^- + \geqslant 1$ jet and (right) $Z/\gamma^* \rightarrow e^+e^- + \geqslant 2$ jets events.

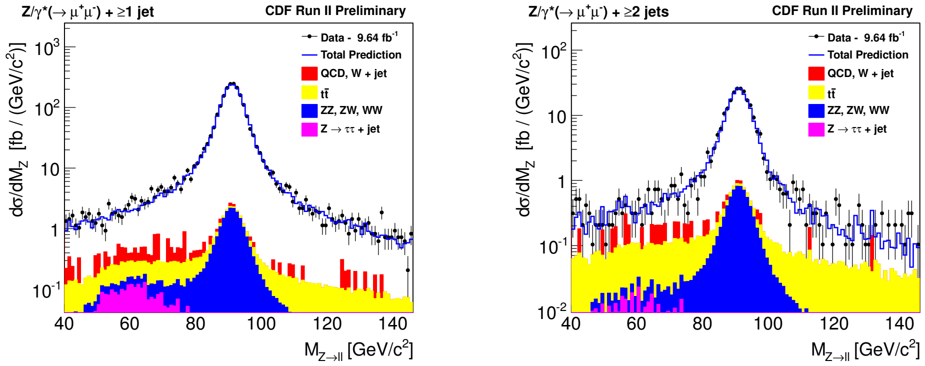

Figure 4.8: Data and signal plus background estimation within Z mass window and on side bands, in (left) $Z/\gamma^* \rightarrow \mu^+\mu^- + \geqslant 1$ jet and (right) $Z/\gamma^* \rightarrow \mu^+\mu^- + \geqslant 2$ jets events.

4.5 $Z/\gamma^* \to l^+l^-$ inclusive cross section

The measurement of the $Z/\gamma^* \to e^+e^-$ and $Z/\gamma^* \to \mu^+\mu^-$ inclusive cross sections provide a check of the accuracy of the Z/γ^* reconstruction and of the trigger and lepton identification efficiencies calculation described in section 4.3. The $Z/\gamma^* \to l^+l^-$ inclusive cross section was measured with the CDF detector in [71], and was found in good agreement with the NNLO prediction. In this study only the statistical and luminosity uncertainties of the Z/γ^* cross section measurement are evaluated, while the systematic uncertainties are not considered. $Z/\gamma^* \to l^+l^-$ events are selected with the same method used for the $Z/\gamma^* \to l^+l^-$ + jets measurements and discussed in section 4.3.2. In the $Z/\gamma^* \to \mu^+\mu^-$ channel a cosmic muon rejection requirement is added to the selection: when the 3D opening angle between the two muons is $\geqslant 3.1$ rad at least one of the muons is required not to be tagged as cosmic according to COT timing criteria.

The processes considered as sources of backgrounds include QCD and W + jets, $Z \to \tau^+\tau^-$, $t\bar{t}$, and WW production. ZZ and ZW events are considered as signal for the inclusive cross section since a $Z/\gamma^* \to l^+l^-$ (l=e,μ) decay may occur in such processes. The inclusive cross section is evaluated for each Z/γ^* category and run period according to:

$$\sigma_{ip}(Z/\gamma^* \to l^+l^-) = \frac{N_{ip}^{data} - N_{ip}^{data-bkg} - N_{ip}^{MC-bkg}}{\mathcal{L}^p \cdot A_{ip}^{data}} \tag{4.14}$$

$$N_{ip}^{MC-bkg} = N_i^{MC-bkg} \cdot SF_{ip} \cdot \epsilon_p^{vtx} \cdot \frac{\mathcal{L}_p}{\mathcal{L}_{MC}} \tag{4.15}$$

$$A_{ip}^{data} = A_{ip}^{MC} \cdot SF_{ip} \cdot \epsilon_p^{vtx} \tag{4.16}$$

$$p = 0d, 0h, 5-7, 8, 9..., 38 \tag{4.17}$$

where i = CEM-CEM, CMUP-CMUP, CMX-CMX, CMUP-CMX, CMUP-CMIO, CMX-CMIO are the $Z/\gamma^* \to l^+l^-$ categories, N_{ip}^{data} is the Z/γ^* yield in data for category i and run period p, $N_{ip}^{data-bkg}$ is the data driven background estimation, N_i^{MC-bkg} is the number of background events estimated from Monte Carlo, $\mathcal{L}_p$ is the integrated luminosity of run period p, $\mathcal{L}_{MC}$ is the luminosity of each Monte Carlo dataset, obtained as the number of events divided by the cross section of the simulated process, A_{ip}^{MC} is the acceptance of the Z/γ^* reconstruction and selection for category i and run period p evaluated with the $Z/\gamma^* \to l^+l^-$ inclusive Monte Carlo, SF_{ip} is the corresponding Data/MC scale factor and ϵ_p^{vtx} is the primary vertex acceptance for run period p. Cross sections per run period are evaluated separately for the $Z/\gamma^* \to e^+e^-$ and $Z/\gamma^* \to \mu^+\mu^-$ channels, in the $Z/\gamma^* \to \mu^+\mu^-$ channel Z/γ^* categories are combined according to:

$$\sigma_p(Z/\gamma^* \to l^+l^-) = \frac{(N_p^{data} - N_p^{data-bkg}) - N_p^{MC-bkg}}{\mathcal{L}_p \cdot A_p^{data}} \tag{4.18}$$

$$N_p^{data} = \sum_i N_{ip}^{data} \tag{4.19}$$

$$N_p^{data-bkg} = \sum_i N_{ip}^{data-bkg} \tag{4.20}$$

$$N_p^{MC-bkg} = \sum_i N_{ip}^{MC-bkg} \tag{4.21}$$

$$A_p^{data} = \sum_i A_{ip}^{MC} \cdot SF_{ip} \cdot \epsilon_p^{vtx} \tag{4.22}$$

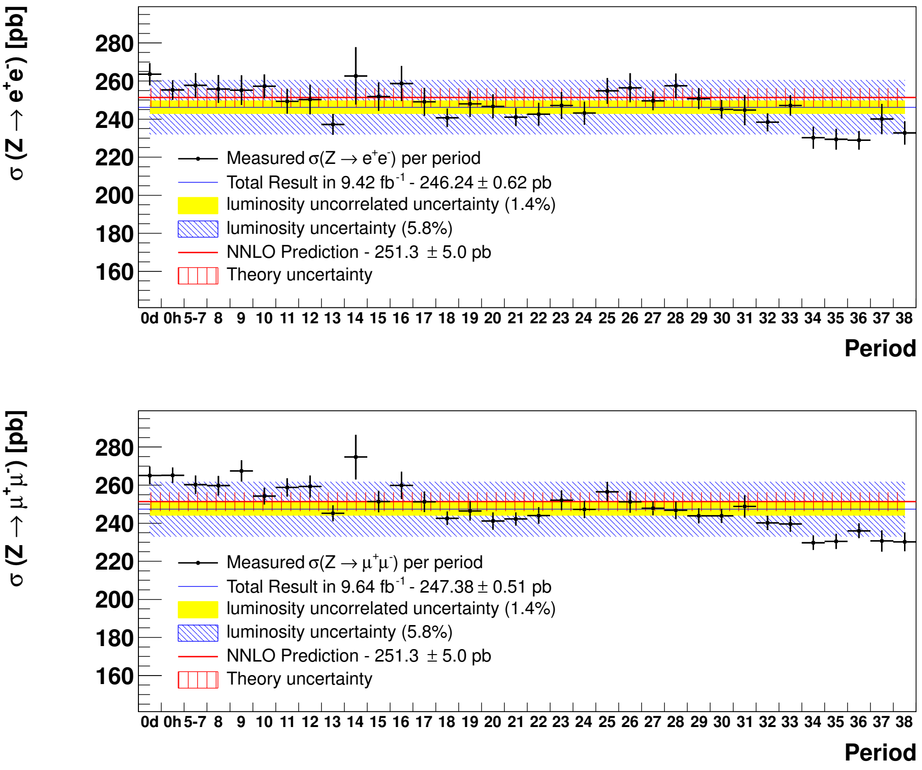

Figure 4.9: Inclusive $Z/\gamma^* \to l^+l^-$ cross section as a function of run period (up) in the $Z/\gamma^* \to \mu^+\mu^-$ decay channel and (down) in the $Z/\gamma^* \to e^+e^-$ decay channel.

Z/γ^* category		Measured cross section [pb]
$Z/\gamma^* \to e^+e^-$	CEM-CEM	246.24 ± 0.62
$Z/\gamma^* \to \mu^+\mu^-$	CMUP-CMUP	249.72 ± 0.76
	CMX-CMX	247.72 ± 0.75
	CMUP-CMX	246.13 ± 0.72
	CMUP-CMIO	246.79 ± 0.95
	CMX-CMIO	246.99 ± 0.91

Table 4.15: $Z/\gamma^* \to l^+l^-$ measured cross sections for Z/γ^* categories, only statistical uncertainties are quoted.

To compare the results per run period with the total result the relative uncertainty of the luminosity fraction need to be evaluated. A 1.4% relative luminosity uncertainty is estimated summing only the uncorrelated contributions to the absolute luminosity uncertainty. Results are shown in Figure 4.9, the $Z/\gamma^* \to l^+l^-$ inclusive cross sections per run period fairly agree with the total cross section result within the statistical and relative luminosity uncertainty. A $\sim$ 10% fall in the cross section is observed starting from run period 34. The same effect appears both in the electron and muon channels, and is probably due to an overestimation of the integrated luminosity in the run periods 34-38. The impact on the total cross section is of the order of 2%, which is well below the 5.8% total luminosity uncertainty.

Cross sections per category are evaluated combining efficiencies and scale factors with respect to relative luminosities fraction per run period according to:

$$\sigma_i(Z/\gamma^* \to l^+l^-) = \frac{(N_i^{data} - N_i^{data-bkg}) - N_i^{MC-bkg}}{\mathcal{L}_{Tot} \cdot A_i^{data}} \tag{4.23}$$

$$N_i^{data} = \sum_p N_{ip}^{data} \tag{4.24}$$

$$N_i^{data-bkg} = \sum_p N_{ip}^{data-bkg} \tag{4.25}$$

$$N_i^{MC-bkg} = \sum_p N_{ip}^{MC-bkg} \tag{4.26}$$

$$A_i^{data} = \sum_p \frac{\mathcal{L}_p}{\mathcal{L}_{Tot}} A_{ip}^{MC} \cdot SF_{ip} \cdot \epsilon_p^{vtx} \tag{4.27}$$

$Z/\gamma^* \to l^+l^-$ measured cross sections per Z/γ^* category are shown in Table 4.16.

The total cross sections in the $Z/\gamma^* \to e^+e^-$ and $Z/\gamma^* \to \mu^+\mu^-$ channels are evaluated combining efficiencies and scale factors with respect to relative luminosities fraction and

	Measured cross section [pb]	Integrated luminosity [fb^{-1}]
$Z/\gamma^* \to e^+e^-$	$246.24 \pm 0.62 \pm 14.3$	9.42
$Z/\gamma^* \to \mu^+\mu^-$	$247.38 \pm 0.51 \pm 14.3$	9.64
NNLO prediction	251.3 ± 5.0	

Table 4.16: $Z/\gamma^* \to e^+e^-$ and $Z/\gamma^* \to \mu^+\mu^-$ measured cross sections, only statistical and luminosity uncertainties are quoted.

Monte Carlo acceptances, according to:

$$\sigma(Z/\gamma^* \to l^+l^-) = \frac{(N^{data} - N^{data-bkg}) - N^{MC-bkg}}{\mathcal{L}_{Tot} \cdot A^{data}} \tag{4.28}$$

$$N^{data} = \sum_{ip} N^{data}_{ip} \tag{4.29}$$

$$N^{data-bkg} = \sum_{ip} N^{data-bkg}_{ip} \tag{4.30}$$

$$N^{MC-bkg} = \sum_{ip} N^{MC-bkg}_{ip} \tag{4.31}$$

$$A^{data} = \sum_{ip} \frac{\mathcal{L}_p}{\mathcal{L}_{Tot}} A^{MC}_{ip} \cdot SF_{ip} \cdot \epsilon^{vtx}_p \tag{4.32}$$

The $Z/\gamma^* \to e^+e^-$ and $Z/\gamma^* \to \mu^+\mu^-$ inclusive cross section measured with the full dataset are 246.24±0.62±14.3 pb and 247.38±0.51±14.3 pb, where only the statistical and luminosity uncertainties are quoted. This values agree within the luminosity uncertainty of 5.8% with the NNLO prediction of 251.3 ± 5.0 pb [71].

4.6 Unfolding

ALPGEN+PYTHIA $Z/\gamma^* \to e^+e^-$ + jets and $Z/\gamma^* \to \mu^+\mu^-$ + jets Monte Carlo samples are used to unfold the measured cross section from detector level back to the particle level with a bin-by-bin procedure. The Monte Carlo samples used for the unfolding are validated comparing measured and predicted cross sections at detector level. The unfolding factors account for $Z/\gamma^* \to l^+l^-$ reconstruction efficiency, particle detection and jet reconstruction in the calorimeter, and the effect of multiple p$\bar{\text{p}}$ interactions in the same bunch crossing.

4.6.1 Detector level Data-Monte Carlo comparison

Before unfolding the cross section, data and ALPGEN+PYTHIA samples are compared at detector level in the most relevant variables. The measured detector level cross section per bins of the variable α is defined as:

$$\frac{\Delta\sigma^{data}_{detector}(\alpha)}{\Delta\alpha} = \frac{1}{\Delta\alpha}\frac{\sum_{ip} N^{data}_{ip}(\alpha)}{\mathcal{L}} \tag{4.33}$$

$$p = 0d, 0h, 5-7, 8, 9..., 38 \tag{4.34}$$

where $N^{data}_{ip}(\alpha)$ is the number of jets per bin for run period p and Z/γ^* category i.

The corresponding Monte Carlo prediction is evaluated as:

$$\frac{\Delta\sigma^{prediction}_{detector}(\alpha)}{\Delta\alpha} = \frac{\Delta\sigma^{MC}_{detector}(\alpha)}{\Delta\alpha} + \frac{\Delta\sigma^{MC-bkg}_{detector}(\alpha)}{\Delta\alpha} + \frac{\Delta\sigma^{data-bkg}_{detector}(\alpha)}{\Delta\alpha} \tag{4.35}$$

$$\frac{\Delta\sigma^{MC}_{detector}(\alpha)}{\Delta\alpha} = \frac{1}{\Delta\alpha}\sum_{ip}\frac{N_i^{MC}(\alpha)}{\mathcal{L}_{MC}}\cdot SF_{ip}\cdot\epsilon_p^{vtx}\cdot\frac{\mathcal{L}_p}{\mathcal{L}_{Tot}} \tag{4.36}$$

$$\frac{\Delta\sigma^{MC-bkg}_{detector}(\alpha)}{\Delta\alpha} = \sum_{bkgs}\sum_{ip}\frac{N_i^{MC-bkg}(\alpha)}{\mathcal{L}_{MC-bkg}}\cdot SF_{ip}\cdot\epsilon_p^{vtx}\cdot\frac{\mathcal{L}_p}{\mathcal{L}_{Tot}} \tag{4.37}$$

$$\frac{\Delta\sigma^{data-bkg}_{detector}(\alpha)}{\Delta\alpha} = \frac{1}{\Delta\alpha}\frac{\sum_{ip} N_{ip}^{data-bkg}(\alpha)}{\mathcal{L}} \tag{4.38}$$

where in the Monte Carlo background contributions the sum is over all the considered sources described in section 4.4.

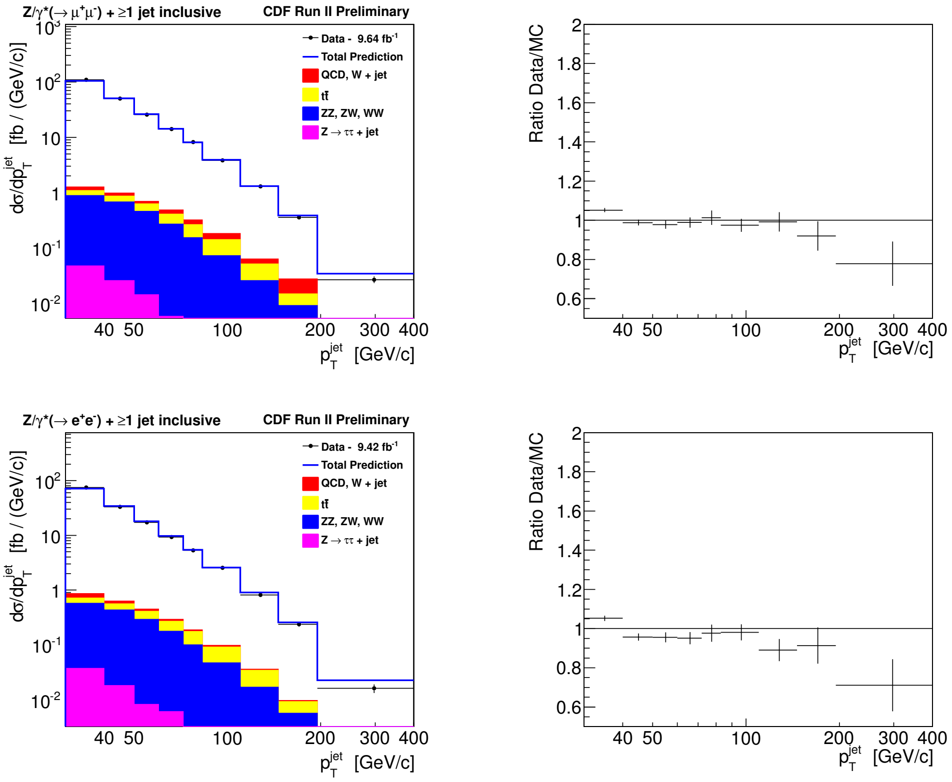

Figure 4.10: Detector level differential cross section as a function of inclusive jet p_T in $Z/\gamma^* + \geqslant 1$ jet events. Data are compared to ALPGEN+PYTHIA Monte Carlo prediction, only statistical uncertainties are shown.

With the particular choice of settings used to generate the sample, detailed in section 4.2, and especially due to the new α_s-matched procedure [34], the ALPGEN+PYTHIA Monte Carlo does not need any normalization factor to properly describe data. The features of the new ALPGEN+PYTHIA prediction are further discussed in section 5.9.

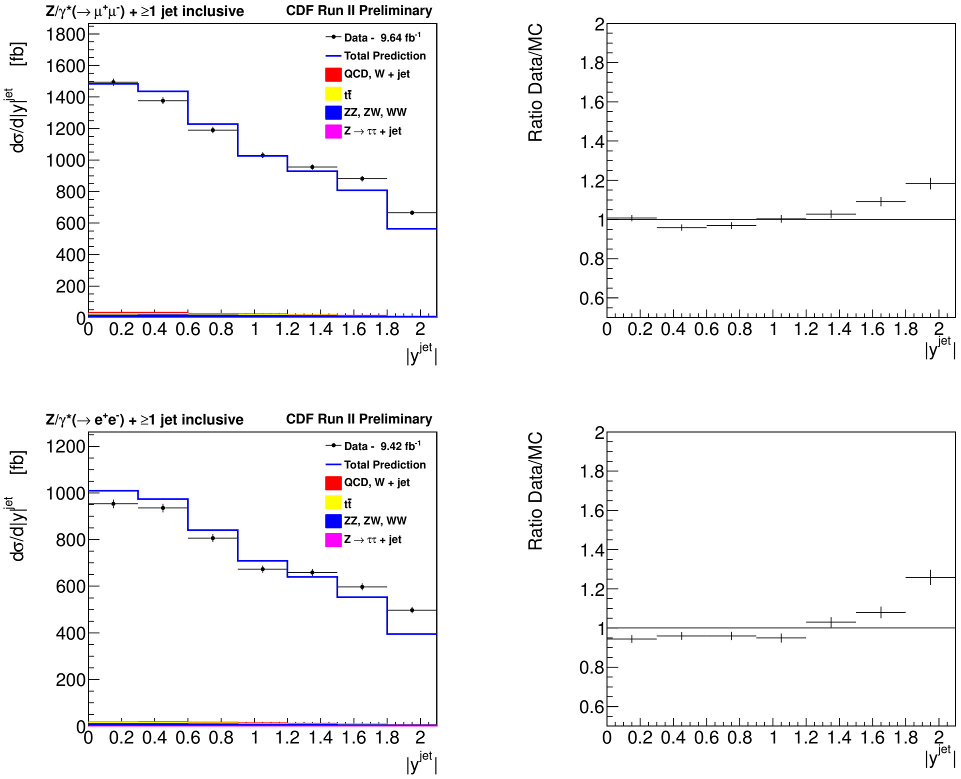

Figure 4.11: Detector level differential cross section as a function of inclusive jet rapidity in Z/γ^* + $\geqslant 1$ jet events. Data are compared to ALPGEN+PYTHIA Monte Carlo prediction, only statistical uncertainties are shown.

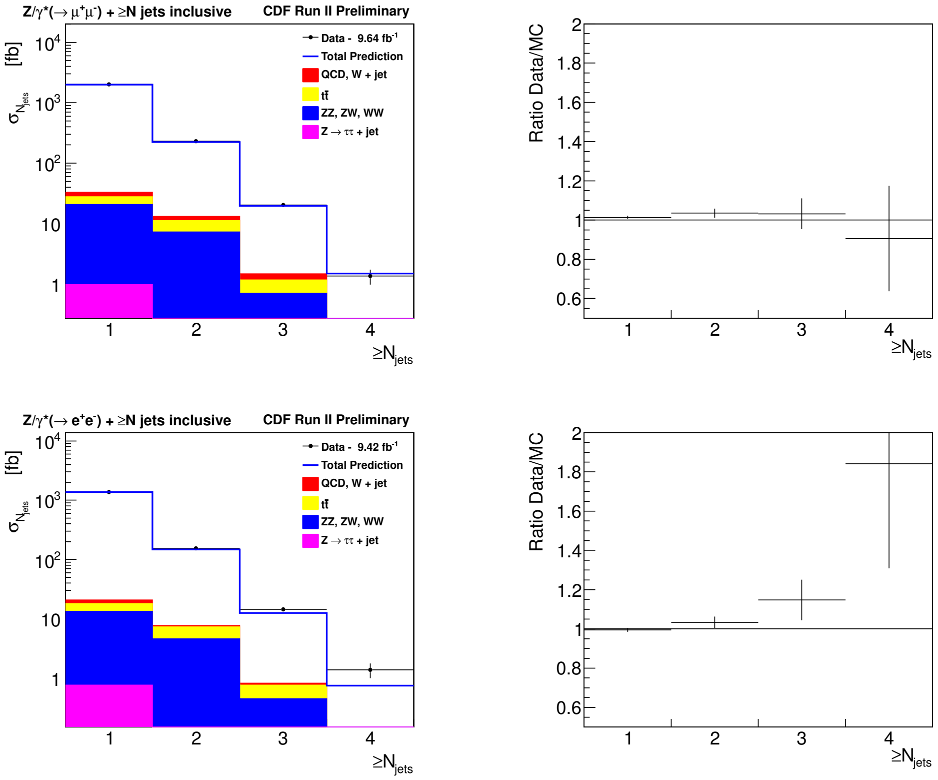

Figure 4.12: Detector level cross section as a function of jet multiplicity. Data are compared to ALPGEN+PYTHIA Monte Carlo prediction, only statistical uncertainties are shown.

The detector level cross section as a function of inclusive jet p_T is compared with the ALPGEN+PYTHIA prediction in Figure 4.10. Figure 4.11 shows the detector level cross section as a function of jet rapidity. A fair agreement is found for the shape of both variables. Cross section as a function of jet multiplicity is shown in Figure 4.12.

4.6.2 Measurement definition

The measurement of $Z/\gamma^* \rightarrow l^+l^-$ + jets production cross sections is performed at particle level: measured cross sections are unfolded back to particle level and theoretical prediction are corrected to the same level when needed. Particle level refers to physics objects reconstructed from quasi-stable (lifetime > 10 ps) and confined final state particles. The definition of the particle level jets corresponds to the *truth level* of the hadronic final state outlined in Section 9 of [72], and includes hadronization and underlying event contribution, but not the contribution from pile-up of multiple $p\bar{p}$ interactions in the same bunch crossing. According to such definition jets are reconstructed at particle level clustering final state particles after parton shower and hadronization evolution, and including particles originated from multi-parton interactions. Particle level jets are often called hadron level jets, a schematic view is shown in Figure 4.13. In the particle level definition used in this measurement radiated photons are recombined with leptons following a scheme similar to that used in [18]. A photon and a lepton from $Z/\gamma^* \rightarrow l^+l^-$ decay are recombined when $\Delta R_{\gamma-l} < 0.1$. If both charged leptons in the final state are close to a photon, the photon is recombined with the lepton with the smallest $\Delta R_{\gamma-l}$. Photons which are not recombined to leptons are included in the list of particles for the jet clustering. With such definition leptons can be referred as "dressed", compared to a "bare" lepton definition in which ra-

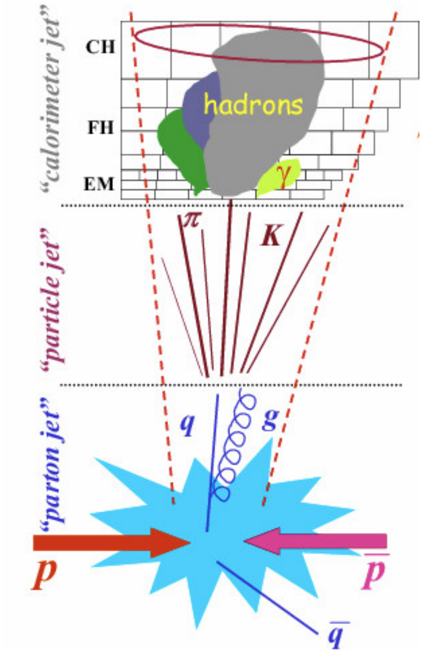

Figure 4.13: Schematic view of hadron-particle level jets.

	Kinematic requirements
Leptons	$P_T^\mu \geqslant 25$ GeV/c $E_T^e \geqslant 25$ GeV $\lvert\eta^l\rvert \leqslant 1.0$
Z/γ^* boson	66 GeV/c$^2 \leqslant \mathrm{M_Z} \leqslant$ 116 GeV/c^2
Jets	$p_T^{\mathrm{jet}} \geqslant 30$ GeV/c $\lvert y^{\mathrm{jet}}\rvert \leqslant 2.1$

Table 4.17: Phase space measurement definition.

diated photons are not recombined. The definition of a lepton-photon recombination at particle level is particularly important to allow comparison with theoretical predictions which include photon radiation, such the NLO QCD $\otimes$ NLO EW prediction discussed in section 5.11. Notice also that there is not any requirement on the energy fraction of photons inside a jet, consequently also a photon can originate a jet at particle level, and Z/γ^* + γ production enters within the definition of Z/γ^* + jets besides $Z/\gamma^* + q$ and $Z/\gamma^* + g$. Similarly at detector level requirements on the fraction of the jet energy deposited in the electromagnetic calorimeter are not applied, and the Z/γ^* + γ process is not considered as a background. The reason of this choice is that both at detector and at particle levels issues arise in the definition of an electromagnetic fraction requirement: at detector level it would be necessary to evaluate the efficiency of such requirement on jets originated by partons, at particle level a cut on the energy fraction of a photon is not collinear safe, as discussed in [18]. The contribution of Z/γ^* + γ process to the Z/γ^* + jets cross section is at the percent level, it is accounted through QED ISR and FSR PYTHIA simulation, further details are given in sections 5.1 and 5.3.

Physics object reconstruction and kinematic requirements applied at particle level establish the measurement definition. Jets are reconstructed at particle level in the Monte Carlo sample with the midpoint algorithm in a cone of radius $R = 0.7$, merging/splitting fraction set to $f = 0.75$, and using as seeds particles with $p_T \geqslant 1$ GeV/c. In order to minimize the uncertainty of extrapolating the measured cross sections to a larger kinematic region, the same requirements applied to jets and leptons at detector level, described in section 4.3, are applied at particle level. Particle level kinematic requirements are summarized in Table 4.17, such requirements define the phase space of the measurement.

The measured particle level cross section is defined as

$$\frac{\Delta\sigma^{data}_{particle}(\alpha)}{\Delta\alpha} = \left(\frac{\Delta\sigma^{data}_{detector}(\alpha)}{\Delta\alpha} - \frac{\Delta\sigma^{MC-bkg}_{detector}(\alpha)}{\Delta\alpha} - \frac{\Delta\sigma^{data-bkg}_{detector}(\alpha)}{\Delta\alpha}\right) \cdot U(\alpha) \tag{4.39}$$

where $U(\alpha)$ is the bin-by-bin unfolding factors for the variable α defined as follows:

$$U(\alpha) = \frac{N^{MC,particle}(\alpha)}{\sum_{ip} \frac{\mathcal{L}_p}{\mathcal{L}_{Tot}} \cdot N_i^{MC,detector}(\alpha) \cdot SF_{ip} \cdot \epsilon_p^{vtx}} \tag{4.40}$$

$N^{MC,particle}(\alpha)$ and $N^{MC,detector}(\alpha)$ are the numbers of reconstructed particle level and detector level events in a bin of the variable α, passing the kinematic requirements of Table 4.17.

4.6.3 Multiple p$\bar{\text{p}}$ interactions reweighting

Although the energy of the jets is corrected for the contribution from multiple p$\bar{\text{p}}$ interactions in the same bunch crossing [63], any residual effect needs to be accounted in the unfolding to avoid dependence of the measured cross sections on the instantaneous luminosity. To correct for the residual effects of multiple p$\bar{\text{p}}$ interactions the ALPGEN+PYTHIA Z/γ^* + jets Monte Carlo samples are reweighted to follow the same multiple interactions profile expected in data. The data instantaneous luminosity profile is converted to a multiple interactions profile assuming one extra interaction per $28.254 \cdot 10^{30}\ cm^{-2}s^{-1}$ of instantaneous luminosity. In fact the expected number of multiple interactions as a function of the instantaneous luminosity is $\mu = \frac{\mathcal{L} \cdot \sigma_{in}}{f_{BC}}$ where $\sigma_{in} = 60.7$ mb is the total p$\bar{\text{p}}$ inelastic cross section [60] and $f_{BC} = 1.75$ MHz is the average rate of bunch crossing. A multiple interaction profile is built summing for each run of data taking a poissonian distribution of average rate equal to the expected number of multiple interactions $\mu = L_{Inst}/28.254 \cdot 10^{30}\ cm^{-2}s^{-1}$ and normalized to the integrated luminosity of the run. The Monte Carlo samples are reweighted in the number of extra p$\bar{\text{p}}$ interactions to match such data multiple interactions profile.

4.6.4 Unfolding factors

The unfolding factors $U(\alpha)$ are evaluated bin-by-bin according to equation (4.40), they correct simultaneously for $Z/\gamma^* \to l^+l^-$ acceptance in the detector, efficiency of the reconstruction and selection requirements and jet reconstruction in the calorimeter. They also correct residual dependence of the measured cross section on the instantaneous luminosity not already accounted in the jet energy scale. The unfolding factors as a function of inclusive jet p_T, inclusive jet rapidity and jet multiplicity are shown in Figures 4.14 to 4.16.

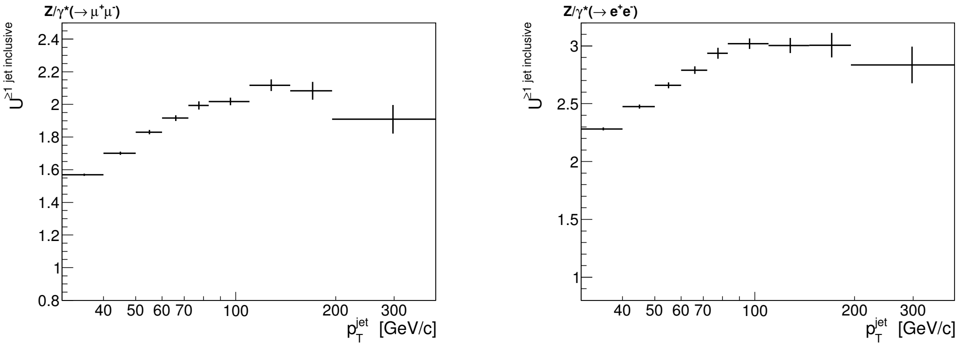

Figure 4.14: Unfolding factors as a function of inclusive jet p_T in events with $Z/\gamma^* + \geqslant 1$ jet.

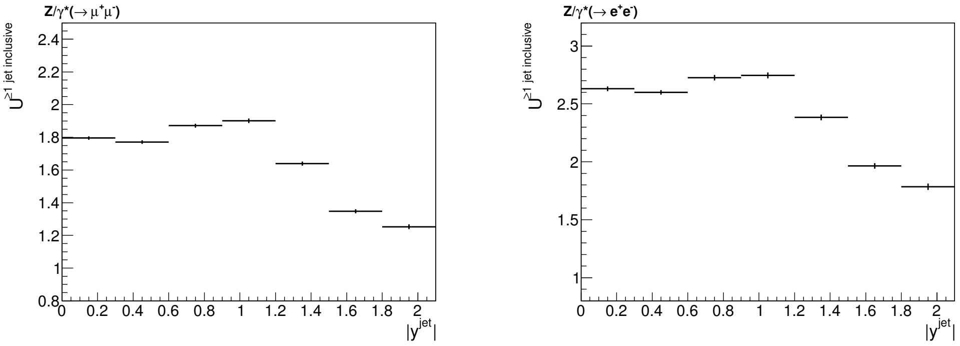

Figure 4.15: Unfolding factors as a function of inclusive jet rapidity in events with Z/γ^* + $\geqslant$ 1 jet.

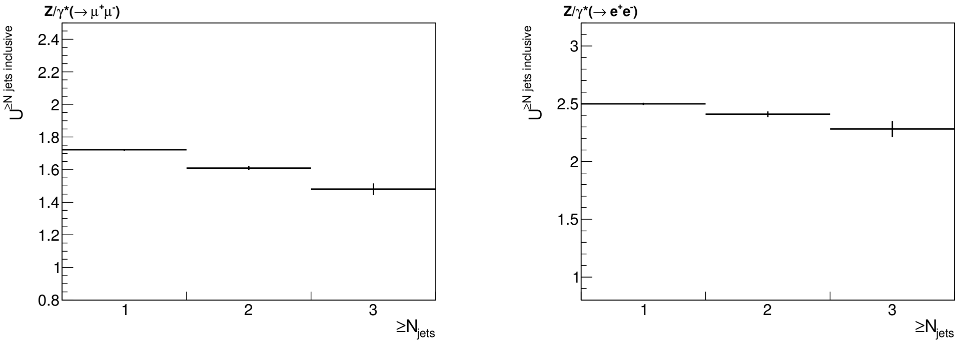

Figure 4.16: Unfolding factors for Z/γ^* + $\geqslant$ N jets as a function of jet multiplicity.

4.7 Systematic uncertainties

The main systematic uncertainty of the $Z/\gamma^* \rightarrow l^+l^-$ + jets measurement is associated to the absolute jet energy scale. Another important systematic uncertainty in the jet energy comes from the multiple $p\bar{p}$ interactions in the same bunch crossing, which affects especially the kinematic region with low p_T jets. Other sources of systematic uncertainties considered in the $Z/\gamma^* \rightarrow l^+l^-$ + jets measurement are related to trigger and lepton identification efficiencies, background subtraction and primary vertex acceptance.

- **Jet energy scale**: The jet energy scale is varied according to [63] to account for the related systematic uncertainty. Three sources of systematic uncertainty are considered, absolute jet energy scale, multiple $p\bar{p}$ interactions, and η-dependent calorimeter response. The absolute jet energy scale uncertainty depends on the response of the calorimeter to an individual particle and on how well the Monte Carlo reproduces the particles multiplicity and p_T spectrum inside a jet. This uncertainty affects especially observables involving high p_T jets and high jet multiplicity. The jet energy uncertainty related to multiple $p\bar{p}$ interactions arises from inefficiency in the reconstruction of multiple interactions vertices, and mainly affects low jet p_T and high jet rapidity kinematic regions, and high jet multiplicity. The η-dependent uncertainty accounts for residual discrepancies between data and Monte Carlo after the calorimeter response has been corrected for the dependence on η of the di-jet p_T balance.

- **Trigger and lepton ID efficiencies and scale factors**: Trigger efficiency and lepton identification uncertainties for each category and run period are evaluated assuming a binomial distribution. All the uncertainties are first propagated into uncertainties on the SF_{ip} scale factors uncertainties and then combined to evaluate the corresponding uncertainty in each bin of the different measured variables.

- **QCD and W+jets background estimation**: In the $Z/\gamma^* \rightarrow e^+e^-$ channel the main source of uncertainty on the QCD and W + jets background subtraction is due to the estimation of the fake rates. A conservative 15% uncertainty is assigned to the fake rate to cover any statistical and systematic uncertainty of the fit functions. In the $Z/\gamma^* \rightarrow \mu^+\mu^-$ channel a conservative 100% uncertainty is considered in the same-sign subtraction of QCD and W + jets background.

- **MC backgrounds**: A conservative 30% uncertainty on the cross section normalization is assigned to the Monte Carlo backgrounds estimation.

- **Vertex efficiency**: The uncertainty on the primary vertex acceptance is $\sim 1\%$, the effect of this uncertainty is propagated to each bin of the measured variables.

Systematic uncertainties as a function of inclusive jet p_T and rapidity are shown in Figure 4.17.

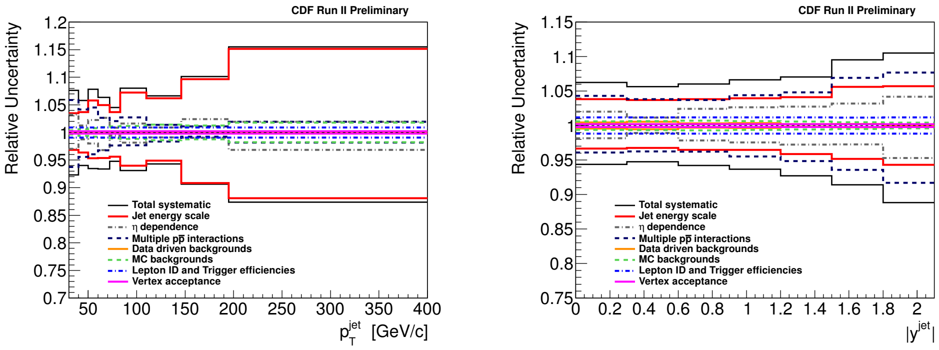

Figure 4.17: Total systematic uncertainties as a function of inclusive jet p_T (left) and inclusive jet rapidity (right) in events with $Z/\gamma^* + \geqslant 1$ jet.

Uncertainty	electrons-muons correlation	proportional to measured value
Statistical	0	no
Jet energy scale	1	yes
Trigger and lepton ID	0	yes
QCD and W+jets background	0	no
MC background	1	no
Vertex efficiency	1	yes

Table 4.18: Uncertainties correlation in the $Z/\gamma^* \to e^+e^-$ and $Z/\gamma^* \to \mu^+\mu^-$ combination.

4.8 $Z/\gamma^* \to e^+e^-$ and $Z/\gamma^* \to \mu^+\mu^-$ decay channels combination

Z/γ^* + jets differential cross sections are measured independently in the $Z/\gamma^* \to e^+e^-$ and $Z/\gamma^* \to \mu^+\mu^-$ decay channels and combined using the BLUE (Best Linear Unbiased Estimate) method [73]. The BLUE algorithm returns a weighted average of the measurements taking into account different types of uncertainty and their correlations. A modified version of the algorithm has been used to treat asymmetric uncertainties, such variant was developed at CDF in the measurement of the single top production cross section [74]. Systematic uncertainties related to trigger efficiencies, lepton reconstruction efficiencies, and QCD and W + jets background estimation are considered uncorrelated between the two channels, the other systematic uncertainties are treated as fully correlated. All the uncertainties, except for the statistical uncertainty and the background estimation systematic uncertainty, are proportional to the measured value of the cross section. As a consequence, fluctuations of the measured cross sections to lower values are associated to reduced proportional uncertainty. To avoid a bias in the combination due to this effect an iterative procedure is applied in which proportional uncertainties are recalculated at each step relatively to the combined cross section value. Correlation and proportionality of the uncertainties are summarized in Table 4.18.

Figures 4.18 and 4.19 show the measured cross sections as a function of inclusive jet p_T, inclusive jet rapidity and Z/γ^* p_T in the $Z/\gamma^* \to e^+e^-$ and $Z/\gamma^* \to \mu^+\mu^-$ channels compared to the combined $Z/\gamma^* \to l^+l^-$ cross section. Only the statistical and the uncorrelated systematic uncertainties are shown in the plots.

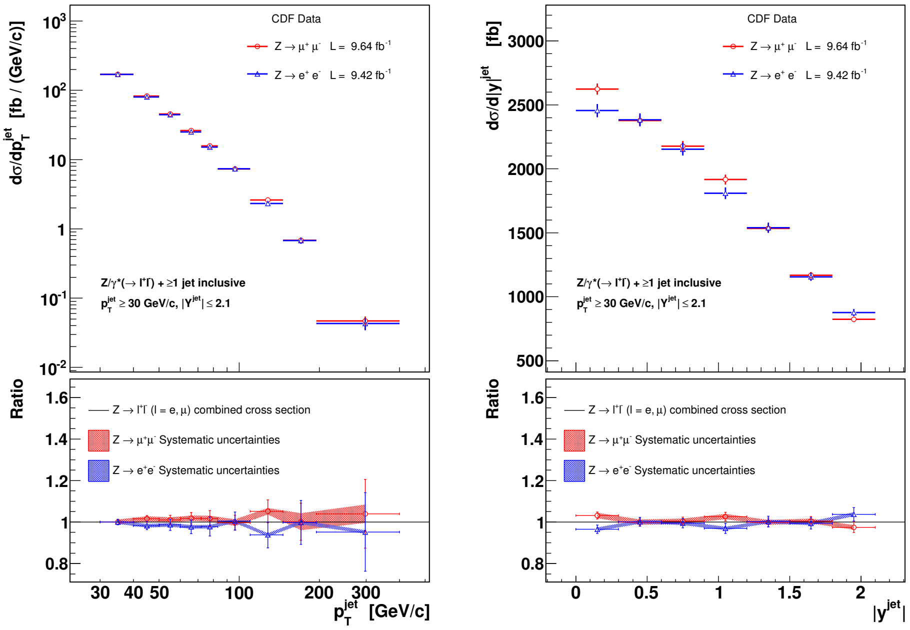

Figure 4.18: Measured cross sections in the $Z/\gamma^* \to \mu^+\mu^-$ and $Z/\gamma^* \to e^+e^-$ decay channels as a function of (left) inclusive jet p_T and (right) inclusive jet rapidity in events with $Z/\gamma^* + \geqslant 1$ jet.

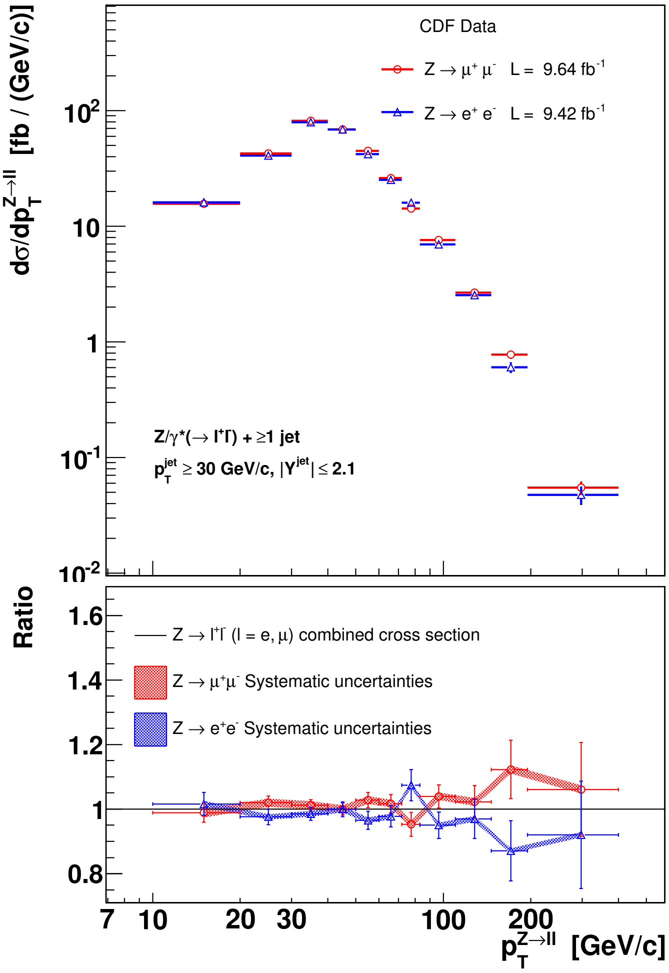

Figure 4.19: Measured cross sections in the $Z/\gamma^* \to \mu^+\mu^-$ and $Z/\gamma^* \to e^+e^-$ decay channels as a function of Z/γ^* p_T in events with Z/γ^* + $\geqslant$ 1 jet.

Chapter 5

Results

The ability of theoretical predictions to describe Z/γ^* + jets final states, and the accuracy of such modeling can be investigated through a detailed analysis of several differential cross sections. From a critical comparison of the measured Z/γ^* + jets differential cross sections with several theoretical predictions a general picture emerges, in which experimental or theoretical uncertainties can be in turn the limiting factor. Measured cross sections are compared with LO-ME+PS Monte Carlo ALPGEN+PYTHIA, NLO perturbative QCD predictions from MCFM and BLACKHAT+SHERPA, NLO+PS POWHEG+PYTHIA and approximate n̄NLO LOOPSIM+MCFM. MCFM predictions are available for Z/γ^* + $\geqslant 1$ and 2 jets final states, LOOPSIM+MCFM only for Z/γ^* + $\geqslant 1$ jet final state, NLO BLACKHAT+SHERPA for jet multiplicity up to Z/γ^* + $\geqslant 3$ jets and POWHEG+PYTHIA predictions are available for all the jet multiplicities but have NLO accuracy only for Z/γ^* + $\geqslant 1$ jet. ALPGEN LO calculation is available for jet multiplicities up to Z/γ^* + 6 jets but for the current comparison the matrix elements generation has been performed up to Z/γ^* + 4 jets. A recently developed Monte Carlo program allows the calculation of both NLO electroweak and NLO QCD corrections to the Z/γ^* + $\geqslant 1$ jet cross sections [18], the QCD and electroweak part of the NLO corrections are combined on the base of a factorized ansatz. Detailed features of these theoretical predictions are discussed in Chapter 2.

Section 5.1 describes the non-perturbative QCD corrections related to hadronization and multi-parton interactions and the radiative QED corrections which need to be applied to the fixed order QCD predictions MCFM, BLACKHAT and LOOPSIM. In section 5.2 the issue of IRC-unsafety of the midpoint jet algorithm is discussed, while section 5.3 describes settings and parameters of the theoretical predictions. In sections 5.4 and 5.5 measured differential cross sections in the Z/γ^* + $\geqslant 1$ jet and Z/γ^* + $\geqslant 2$ jets final states are shown and the agreement with the different predictions is discussed, section 5.6 shows the Z/γ^* + $\geqslant N$ jets measured cross section as a function of jet multiplicity. The following sections 5.7, 5.8, 5.9 and 5.10 present detailed features and further variations of the theoretical predictions LOOPSIM, BLACKHAT, ALPGEN, and POWHEG. Section 5.11 discuss the impact of NLO electroweak corrections and shows the comparison with NLO QCD $\otimes$ NLO EW prediction.

5.1 Non-perturbative QCD corrections and QED radiation

Fixed order perturbative QCD predictions need to be corrected for non-perturbative QCD effects in order to compare them with the measured cross sections. In fact the underlying event associated to multi-parton interactions and beam remnants and hadronization are not simulated in fixed order predictions. Another important effect which is not accounted for in the perturbative QCD predictions and which needs to be evaluated is the QED photon radiation from leptons and quarks. Both ISR and FSR are considered, with the main effect coming from FSR. The inclusion of QED radiation also corrects the Z/γ^* + jets cross sections for the contribution of $Z/\gamma^* + \gamma$ production, which enters the definition of the Z/γ^* + jets particle level used in this measurement, as discussed in section 4.6.2. The non-perturbative QCD effects and the QED radiation are estimated with the ALPGEN+PYTHIA α_s-matched Tune Perugia 2011 Monte Carlo simulation, where the PYTHIA Monte Carlo handle the simulation of these effects. To evaluate the corrections parton level and particle level ALPGEN+PYTHIA cross sections are defined: parton level cross sections are calculated with QED radiation, hadronization and multi-parton interactions switched off in the PYTHIA settings, while for the particle level cross sections the three switches are turned on. Kinematic requirements on leptons and jets and jet clustering parameters for the parton and particle levels are the same used for the measured cross sections, and the lepton-photon recombination described in section 4.6 is applied whenever radiated photons are present in the final state. The corrections are obtained evaluating the ratio of the particle to parton cross sections bin-by-bin for the various measured variables. To evaluate the different impact of QED radiation, hadronization and underlying event, a breakdown of the parton to particle corrections is performed.

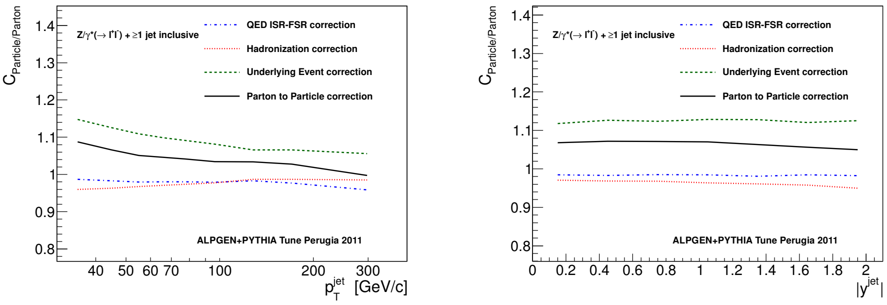

Figure 5.1: Parton to particle corrections as a function of inclusive jet p_T and inclusive jet rapidity for $Z/\gamma^* + \geqslant 1$ jet events. The relative contribution of QED radiation, hadronization and underlying event is shown.

Figure 5.1 shows the parton to particle correction as a function of inclusive jet p_T and inclusive jet rapidity for $Z/\gamma^* + \geqslant 1$ jet events, with the different contributions from QED ISR and FSR radiation, hadronization and underlying event. The corrections have a moderate dependence with the jet multiplicity, as shown in Figure 5.2.

Figure 5.3 shows the parton to particle corrections evaluated with different tunes of the underlying event and hadronization model, and with the POWHEG+PYTHIA simulation. The corrections are generally below 10%, and quite independent from the PYTHIA

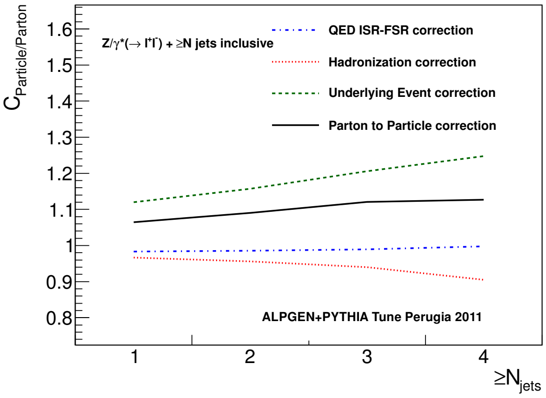

Figure 5.2: Parton to particle corrections as a function of jet multiplicity.

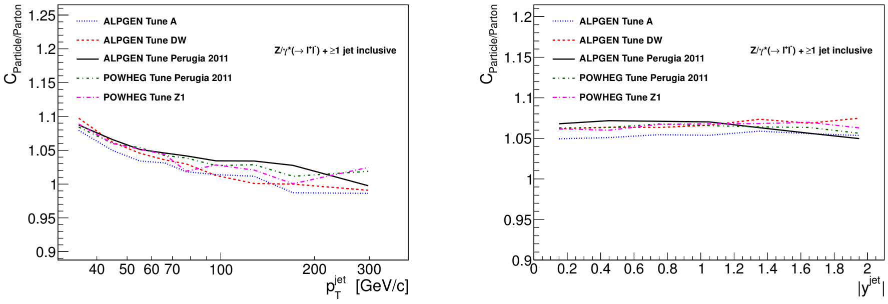

Figure 5.3: Parton to particle corrections as a function of inclusive jet p_T and inclusive jet rapidity for $Z/\gamma^* + \geqslant 1$ jet events. The impact of different choices of the PYTHIA tune and of different matrix element generators ALPGEN or POWHEG is shown.

Monte Carlo tune and from the underlying matrix element generator ALPGEN or POWHEG. Two important exceptions are the Z/γ^* p_T in the low p_T region and the $\Delta\phi$ between the leading jet and the Z/γ^* in the region below $\pi/2$, where the corrections are higher and have a larger dependence on the PYTHIA tune, as shown in Figure 5.4. These two regions are indeed more sensitive to non-perturbative QCD effects. The high underlying event corrections to the Z-jet $\Delta\phi$ in the region below $\pi/2$ are enhanced by double parton scattering (DP) contribution[1]. The relative contribution of Z/γ^* + jet production in double parton interactions is more important in the region below $\pi/2$ where the Z/γ^* + jets cross section is much lower because only Z + $\geqslant$ 3 jets events contributes to the perturbative QCD prediction, as discussed in section 5.4.

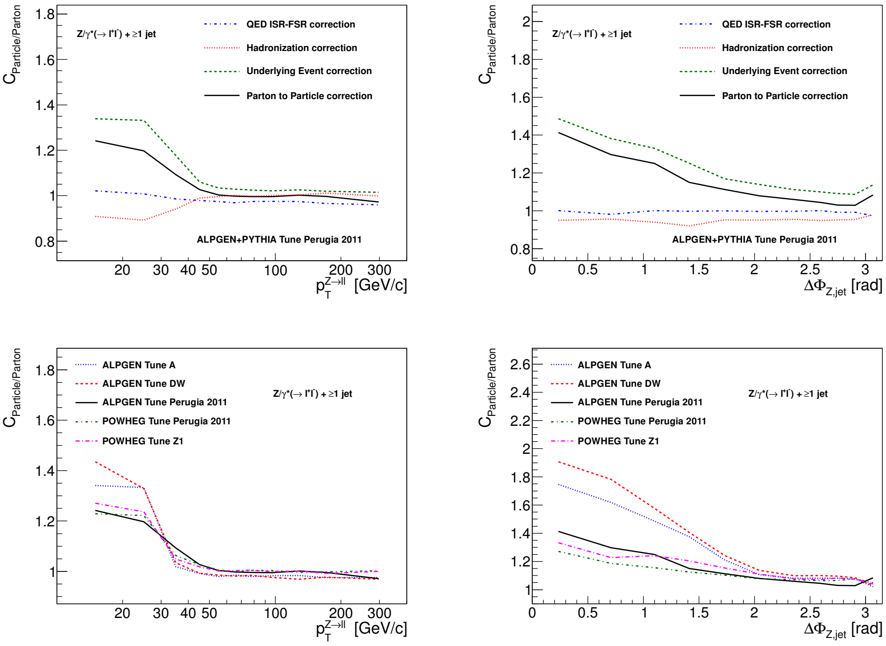

Figure 5.4: Parton to particle corrections as a function of Z/γ^* p_T and Z-jet $\Delta\phi$ for Z/γ^* + $\geqslant$ 1 jet events.

Because of these large non-perturbative corrections the comparison with fixed order perturbative QCD predictions in the low Z/γ^* p_T and low Z-jet $\Delta\phi$ kinematic regions is not very meaningful, while the predictions provided by Monte Carlo tools including parton shower evolution like ALPGEN+PYTHIA and POWHEG+PYTHIA are more reliable.

In general it would be desirable to reduce the amount of non-perturbative QCD corrections and the related uncertainty, one possibility is an appropriate choice of the jet reconstruction algorithm. As shown at the end of section 5.2, the anti-k_T jet algorithm has a lower dependence on the hadronization modeling, while SISCone is less sensitive to the underlying event.

---

[1] for a detailed discussion of DP interactions in γ + 3 jets events see [75]

5.2 IRC safe jet algorithms and perturbative QCD predictions

Until the recent development of fast algorithms for the jet clustering [15] [82], iterative cone jets had the practical advantage of requiring less CPU time than cluster and seedless cone jets, and historically they have been prefered for detector level jets where the reconstruction algorithm is run over a high number of particles. For this reason most of the measurements performed with the CDF detector employ iterative cone algorithms in the jetclu and CDF midpoint variants. As a consequence the CDF jet energy scale corrections have been developed and tuned on iterative cones algorithms, and the use of one such algorithm has the important advantage of having a solid understanding and validation of the jet energy corrections and uncertainties. As a drawback iterative cone algorithms are in general affected by infra-red and collinear (IRC) safety issues, in particular the CDF midpoint jet algorithm used in this measurement is infra-red unsafe, divergences appear in a fixed order calculation for configurations with three hard particles in a common neighborhood plus a soft one. These divergences do not appear in the measured cross sections due to the finite resolution and E_T threshold of the calorimeter towers, and get regularized in a fixed order plus parton shower prediction by a lower cutoff for branching at the non-perturbative scale Λ_{QCD}. On the other hand, in a perturbative calculation infrared unsafety can compromise the convergence of the perturbative series. As discussed in [14] and [15] the last meaningful order for a fixed order calculation with midpoint would be NLO for Z/γ^* + 1 jet, LO for Z/γ^* + 2 jets, and no order of calculation is meaningful for $Z/\gamma^* + \geqslant 3$ jets, in fact all the neglected pieces of the perturbative series would be of the same order.

However it is still possible to compare the measured cross sections with a fixed order prediction, the strategy adopted here is to use in the prediction an infrared and collinear safe jet algorithm as close as possible to the midpoint algorithm, and estimate the additional uncertainty coming from the use of different jet algorithms between data and theory. As discussed in [14] midpoint is expected to behave similarly to SISCone when soft particles are present everywhere, and to the anti-kt algorithm when no soft particles are present. Based on this consideration, a possible approach to estimate the uncertainty is to take the difference between the anti-kt and the SISCone fixed order prediction. In the present study a different method has been adopted, cross sections for midpoint and the IRC safe algorithm used in the fixed order prediction have been evaluated with the ALPGEN+PYTHIA LO-ME+PS prediction, and the relative difference at parton showered level is considered as a systematic uncertainty.

Figure 5.5 shows the ratio of midpoint cross sections with SISCone and anti-kt for inclusive jet p_T in $Z/\gamma^* + \geqslant 1$ jet final state. The difference at parton level between SISCone and CDF midpoint is between 2 and 3%, while the difference with anti-kt is of the order of 5%. Higher differences between midpoint and SISCone are observed once the underlying event is switched on.

Figures 5.6 and 5.7 show the same comparison as a function of jet rapidity and jet multiplicity. The difference at parton level between midpoint and SISCone is always below 3% and generally flat, while the anti-kt algorithm have larger deviations with respect to midpoint. Such observations validate what suggested in [15] and also confirmed by the LOOPSIM and BLACKHAT authors: the best choice for a comparison with measurement performed with the midpoint algorithm is SISCone, with the same merge-split threshold $f = 0.75$ and the same jet radius $R = 0.7$ parameters of the CDF midpoint used for the measured cross sections. They also motivate the choice of considering the difference between SISCone and midpoint at showered parton-level, and not the difference between

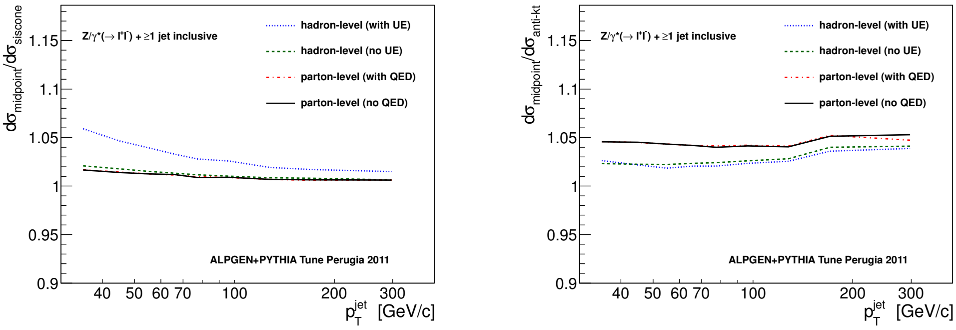

Figure 5.5: Comparison of CDF midpoint with SISCone and anti-kt jet algorithms as a function of inclusive jet p_T in $Z/\gamma^* + \geqslant 1$ jet events.

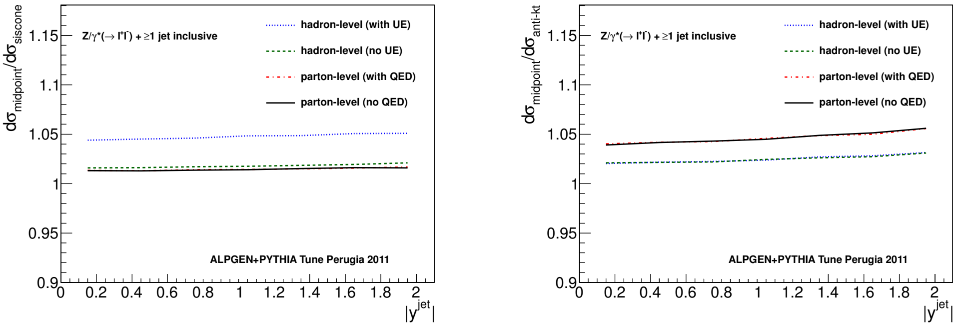

Figure 5.6: Comparison of CDF midpoint with SISCone and anti-kt jet algorithms as a function of inclusive jet rapidity in $Z/\gamma^* + \geqslant 1$ jet events.

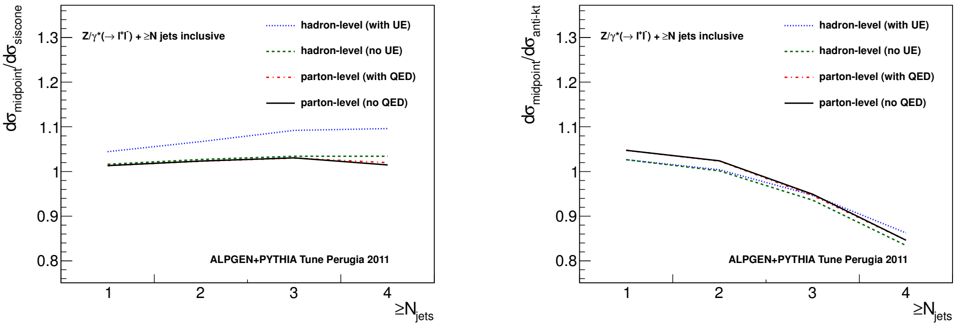

Figure 5.7: Comparison of CDF midpoint with SISCone and anti-kt jet algorithms as a function of jet multiplicity in $Z/\gamma^* + \geqslant N$ jets.

SISCone and anti-kt at fixed order as the uncertainty related to the IR unsafety of the midpoint jet algorithm.

In the context of reducing the non-perturbative corrections in future Z/γ^* + jets studies, the impact of hadronization corrections and underlying event corrections have been studied for CDF midpoint, SISCone and anti-kt.

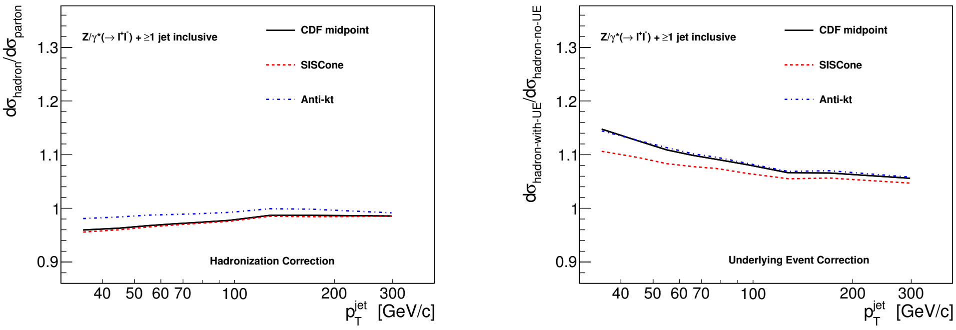

Figure 5.8: Hadronization and underlying event corrections for CDF midpoint, SISCone and anti-kt as a function of inclusive jet p_T in Z/γ^* + $\geqslant 1$ jet events.

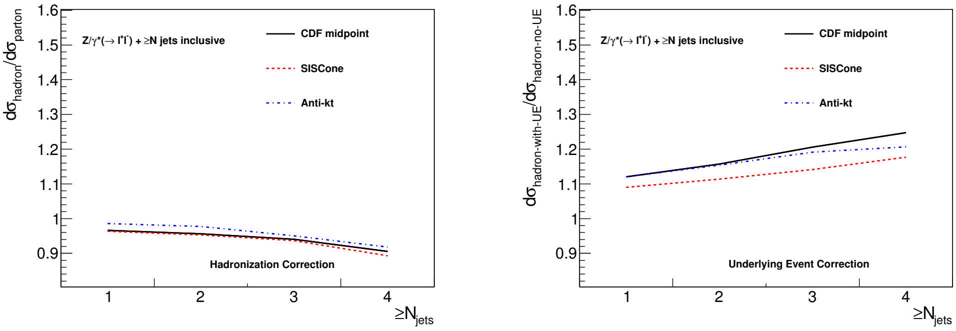

Figure 5.9: Hadronization and underlying event corrections for CDF midpoint, SISCone and anti-kt as a function of jet multiplicity in Z/γ^* + $\geqslant N$ jets.

Figures 5.8 and 5.9 show the corrections as a function of inclusive jet p_T in Z/γ^* + $\geqslant 1$ jet events and as a function of jet multiplicity in Z/γ^* + $\geqslant N$ jets. Anti-kt and midpoint have similar underlying events corrections, while SISCone has reduced contamination from multi-parton interactions. For the hadronization corrections midpoint and SISCone behave very similarly, anti-kt shows reduced corrections.

5.3 Parameters and settings of the theoretical predictions

The parameters of the different predictions have been chosen as homogeneous as possible in order to emphasize the genuine difference between the theoretical models. The MSTW2008 [67] PDF sets have been used as the default choice in all the predictions, with LO PDF analysis and 1-loop running order for α_s for the LO MCFM and BLACKHAT+SHERPA predictions, NLO PDF analysis and 2-loop running order for POWHEG, ALPGEN, NLO MCFM and NLO BLACKHAT predictions, and NNLO analysis and 3-loop running order for the $\bar{n}$NLO LOOPSIM prediction. Uncertainties of the MSTW2008NLO PDF set have been evaluated with the NLO MCFM prediction using the Hessian method [76]. PDF uncertainties are between 2% and 4% and always lower than the experimental systematic uncertainties and the theoretical uncertainty associated to the renormalization and factorization scale variations. The impact of different PDF sets have been studied in MCFM, ALPGEN and POWHEG. The variation in the predictions with CTEQ6.6 [77], NNPDF2.1 [78], CT10 [79] and MRST2001 [80] PDF sets is of the same order of the MSTW2008NLO uncertainty, as far as the same α_s running order is used. The LHAPDF v5.8.6 library [81] has been used to access PDF sets, except in ALPGEN where PDF sets are provided within the Monte Carlo program. The nominal choice for the functional form of the renormalization and factorization scale is $\mu_0 = \hat{H}_T/2 = \frac{1}{2}\big(\sum_j p_T^j + p_T^{l^+} + p_T^{l^-}\big)$ [2] where the index j run over the partons in the final state. Such choice is suggested in [10] and [9], for a further discussion on the appropriate scale for V + jets processes see also [8]. An exception to this default choice is the ALPGEN prediction, where the default scale is set to $\mu_0 = \sqrt{m_Z^2 + \sum_j p_T^j}$, the difference with respect to $\mu_0 = \hat{H}_T/2$ has been studied in this prediction and turned out to be negligible. The factorization and renormalization scale has been varied to half and twice the nominal value $\mu_0 = \mu_0/2$, $\mu_0 = 2\mu_0$, and the corresponding variation in the cross sections is considered as an uncertainty of the prediction. This is the largest uncertainty associated to the theoretical models, except for the ALPGEN+PYTHIA prediction which largest uncertainty is associated to the variation of the renormalization scale in the CKKW scale-setting procedure. In the LO and NLO MCFM predictions jets are clustered with the native MCFM *cone* algorithm with $R = 0.7$. This algorithm is referred as midpoint in the MCFM manual, but is actually a seedless cone algorithm which follows the jet clustering outlined in [61]. Parameters of merging fraction f and R_{sep} are hard-coded in MCFM, the default values of $f = 0.5$ and $R_{sep} = 1$ have been changed to $f = 0.75$ and $R_{sep} = 1.3$ following the same prescription used in the previous Z/γ^* + jets measurement at CDF [20]. The parameter $R_{sep} = 1.3$ is an ad-hoc modification for perturbative QCD level cross section which is probably not very appropriate, as discussed in [15] and [14], it has been kept in the MCFM prediction to allow comparison with the results in [20]. In order to run the LOOPSIM method on top of the MCFM calculation a different setup has been used. In this case the minimum jet p_T for the generation is set to 1 GeV/c, and the jet clustering is performed with the fastjet [82] interface to the SISCone [15] jet algorithm with parameters $R = 0.7$ and $f = 0.75$. MSTW2008NNLO PDF and 3-loop α_s running order are employed for the LOOPSIM+MCFM calculation. The LOOPSIM code and the interface to run it with MCFM are not public, they were provided by the LOOPSIM authors. The authors also provided the settings for the calculation and validated the results. In the BLACKHAT+SHERPA prediction the jet clustering is performed with fastjet, SISCone

---

[2] In BLACKHAT and POWHEG predictions the alternative definition $\mu_0 = \hat{H}'_T/2 = \frac{1}{2}\big(\sum_j p_T^j + E_T^Z\big)$ with $E_T = \sqrt{M_Z^2 + P_{T,Z}^2}$ is used.

algorithm is used and parameters are set to $R = 0.7$ and $f = 0.75$. The predictions were provided by the BLACKHAT authors. In the ALPGEN+PYTHIA prediction the value of Λ_{QCD} in the CKKW scale setting procedure is set to $\Lambda_{QCD} = 0.26$ and 1-loop running order, coherently with the setting of Λ_{QCD} in PYTHIA Tune Perugia 2011 for ISR, FSR and IFSR, following the prescription of [34]. The variation of the CKKW renormalization scale is done together with opposite variation of Λ_{QCD} in the PYTHIA tune. Variations of the renormalization and factorization scale for the matrix element generation is performed independently, this variation affect almost only the factorization scale because the renormalization scale is later reset in the CKKW procedure. The difference with the respect to the previous Tune A and Tune DW have been studied. In this case the running of α_s^{CKKW} in ALPGEN and Λ_{QCD} in PYTHIA are determined by the PDF set, which are set to CTEQ5L on both ALPGEN and PYTHIA to avoid mismatch. The POWHEG calculation is performed with the weighted events option, and the Born suppression factor for the reweight is set to 10 GeV/c, following the prescription used in [39]. The POWHEG code was modified in agreement with the authors to perform studies on the impact of different choices of the functional form of the renormalization and factorization scale. The NLO QCD $\otimes$ NLO EW prediction is evaluated with the Monte Carlo program and the setup described in [18], except for the renormalization and factorization scale which is set to $\mu_0 = \hat{H}_T/2$. NLO QCD and electroweak corrections to the LO cross section are evaluated independently and combined using a factorization ansatz. To isolate the effect of the large virtual corrections due to the Sudakov logarithms, the QED photon final state radiation has been subtracted to the NLO electroweak corrections. In such a way the full parton to particle corrections evaluated in 5.1, which includes ISR and FSR photon radiation as simulated with PYTHIA, can be applied without phase space overlap with the real part of the NLO electroweak correction. All the numerical results of the NLO QCD $\otimes$ NLO EW prediction have been provided by the authors.

5.4 $Z/\gamma^* + \geqslant 1$ jet differential cross sections

$Z/\gamma^* \geqslant 1$ jet production is an important process at hadron colliders, it can be used for instance to validate the jet energy scale by comparing the measured jet p_T against a recoiling Z/γ^*. In the context of search for new physics, a recent study [83] proved that SUSY virtual corrections to the inclusive $Z/\gamma^* \to l^+l^- + \geqslant 1$ jet cross section are small, nevertheless differential cross sections can receive some contributions at the percent level in the high p_T tails. Several theoretical predictions are available for the $Z/\gamma^* + \geqslant 1$ jet final state, the measured differential cross section are compared to ALPGEN+PYTHIA LO-ME+PS, MCFM or BLACKHAT+SHERPA LO and NLO perturbative QCD predictions, POWHEG+PYTHIA NLO+PS, LOOPSIM+MCFM approximate n̄NLO and NLO QCD $\otimes$ NLO EW factorized perturbative predictions.

Figures 5.10 and 5.11 show the leading jet and inclusive jet p_T differential cross sections for $Z/\gamma^* + \geqslant 1$ jet events. All the theoretical predictions are in reasonable agreement with the measured cross sections. In the last bin the measured cross section is slightly lower than the theoretical predictions: for leading jet p_T within $195-400$ GeV/c the ratio of the measured cross section with respect to the NLO BLACKHAT+SHERPA prediction is $0.77 \pm 0.10(\text{stat.})^{+0.12}_{-0.10}(\text{syst.})$, the ratio to n̄NLO LOOPSIM+MCFM is $0.79 \pm 0.10(\text{stat.})^{+0.12}_{-0.10}(\text{syst.})$, and the ratio to NLO QCD $\otimes$ NLO EW is $0.81 \pm 0.10(\text{stat.})^{+0.13}_{-0.10}(\text{syst.})$. The NLO electroweak corrections give a 5% negative contribution in the last Z/γ^* p_T and leading jet p_T bin, due to the large Sudakov logarithms which appears in the virtual part of the calculation. The largest theoretical uncertainty is associated to the variation of the renor-

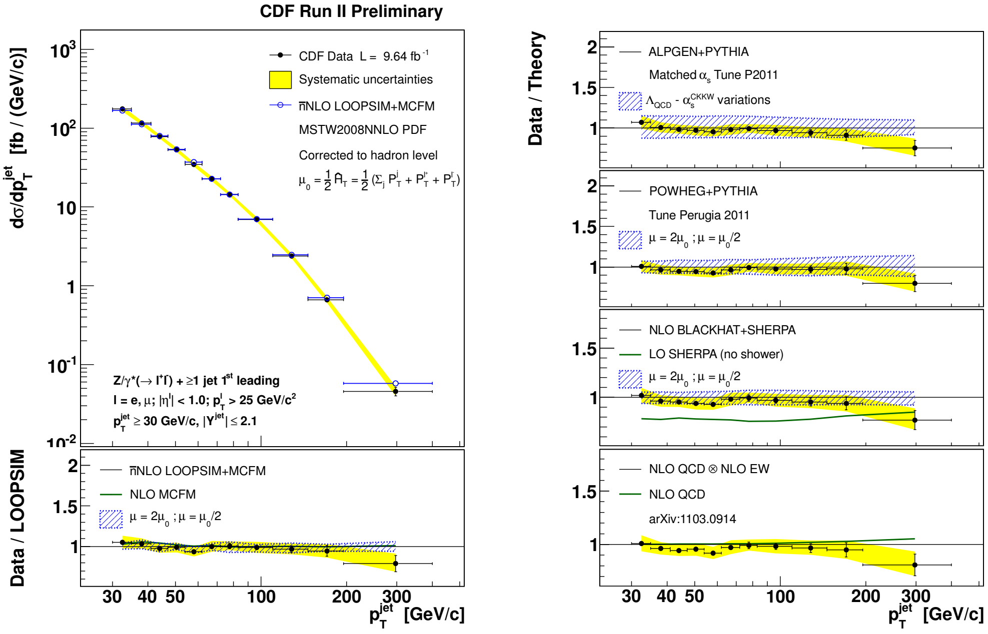

Figure 5.10: Leading jet p_T differential cross section for $Z/\gamma^* + \geqslant 1$ jet events. Measured cross section (black dots) is compared to the LOOPSIM+MCFM n̄NLO prediction (open circles). The yellow bands show the total systematic uncertainty, except for the 5.8% uncertainty on the luminosity. Lower and right boxes show data/theory ratio with respect to other theoretical predictions, the blue dashed band show the main uncertainty of each prediction generally associated to the variation of the renormalization and factorization scale μ.

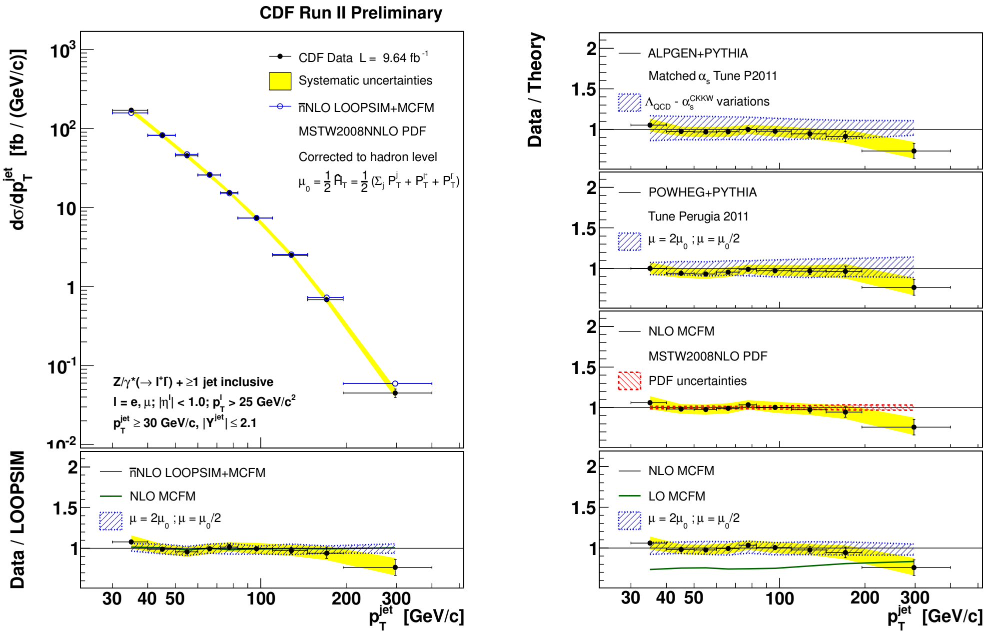

Figure 5.11: Inclusive jet p_T differential cross section for $Z/\gamma^* + \geqslant 1$ jet events. Lower and right boxes show data/theory ratio with respect to other theoretical predictions, the red dashed band show the PDF uncertainty evaluated with the MCFM prediction.

malization and factorization scale, except for the ALPGEN+PYTHIA prediction which has a larger uncertainty associated to the CKKW renormalization scale. Predictions including NLO matrix elements like BLACKHAT MCFM and POWHEG have a lower scale variation dependency with respect to ALPGEN, which normalization accuracy is only at LO. The scale uncertainty in POWHEG appears to be higher than in BLACKHAT, even if both are NLO calculations. This probably reflects a difference in how the renormalization and factorization scale are set in the two calculations: in BLACKHAT the scale is evaluated on the kinematic of the NLO event which can contain one additional parton, while in POWHEG the scale is evaluated on the underlying Born configuration before the radiation of an additional parton. The n̄NLO LOOPSIM prediction does not show any significant deviation from the NLO calculation in this variable, but the scale dependency of this prediction is slightly reduced with respect to NLO. The n̄NLO scale uncertainty is quite independent of the jet p_T and of the order of $4-6\%$. The PDF uncertainty is evaluated with the Hessian method [76] using positive and negative variations along the 20 eigenvectors of the MSTW2008NLO PDF set in the 68% confident level interval, PDF uncertainty is between 2% and 4%.

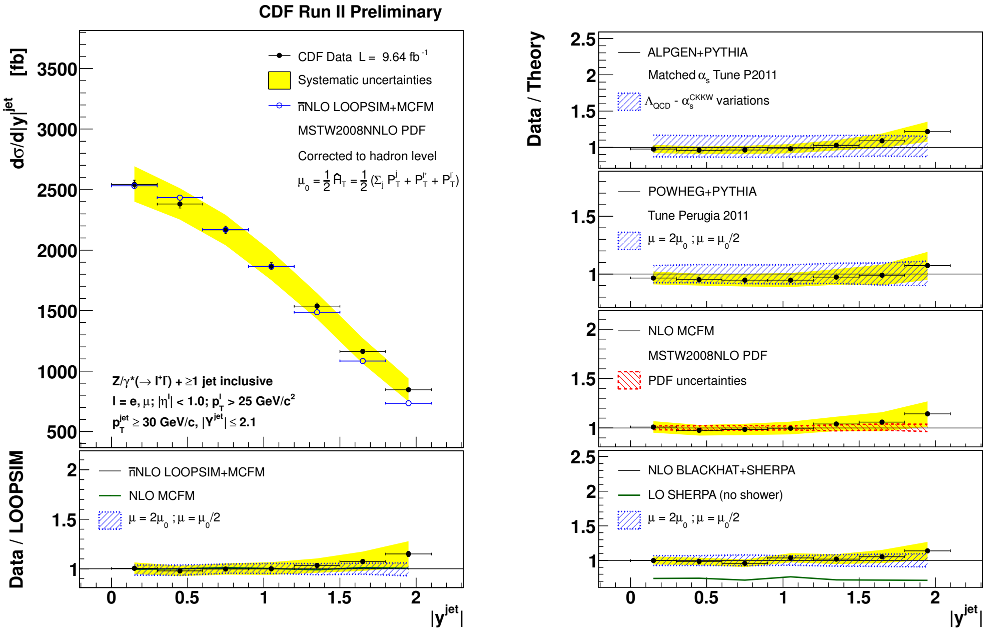

Figure 5.12: $Z/\gamma^* + \geqslant 1$ jet differential cross section as a function of inclusive jet rapidity.

Figure 5.12 shows the inclusive jet rapidity differential cross section for $Z/\gamma^* + \geqslant 1$ jet events. All the predictions correctly model this variable, in the high rapidity region the measured cross section is slightly higher than predictions, however the difference is covered by the experimental systematic uncertainty, dominated in this region by the multiple $p\bar{p}$ interaction uncertainty. The n̄NLO LOOPSIM+MCFM prediction has the lower scale variation theoretical uncertainty, which is of the order of $4-6\%$, the PDF uncertainty is between 2% and 4%. In the high rapidity tail the ALPGEN prediction is lower than other theoretical models, but the difference with data is covered by the large CKKW renormalization scale uncertainty of this prediction.

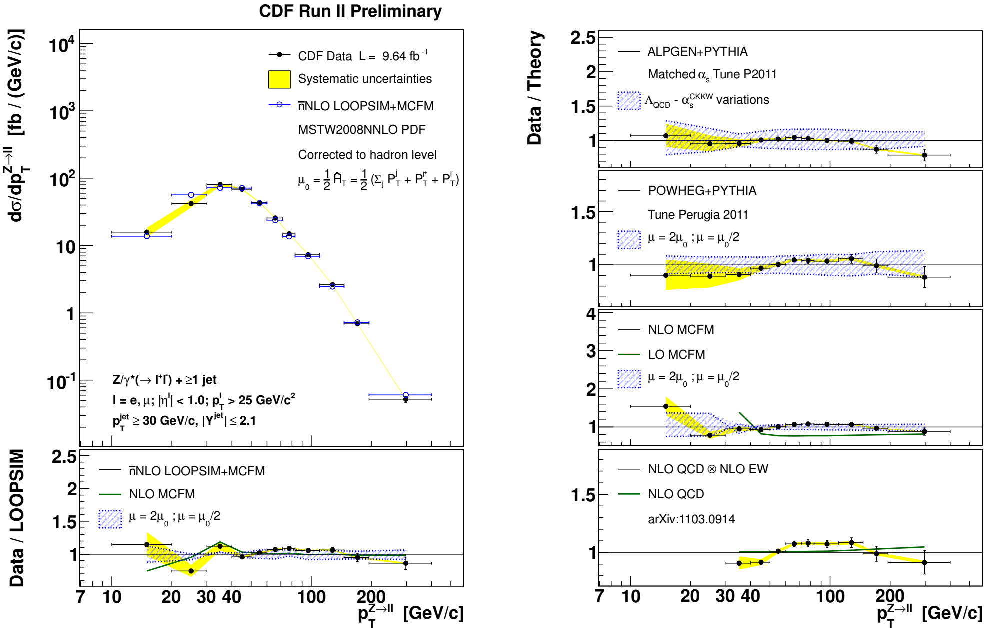

Figure 5.13: $Z/\gamma^* + \geqslant 1$ jet differential cross section as a function of Z/γ^* p_T.

Figure 5.13 shows the Z/γ^* p_T differential cross section for the $Z/\gamma^* + \geqslant 1$ jet final state. The low p_T region below the jet threshold of 30 GeV/c of this distribution is sensitive to soft jets radiation. For this reason the perturbative QCD fixed order calculations MCFM and LOOPSIM+MCFM fail in describing the region below the 30 GeV/c jet p_T threshold, even if an improvement is observed with the $\bar{n}$NLO LOOPSIM+MCFM prediction with respect to the NLO MCFM. As shown in section 5.1 the non-perturbative QCD corrections in the low Z/γ^* p_T region are of the order of 20%, which is much higher than the usual $5 - 10\%$ in the other distributions. The low Z/γ^* p_T region is better described by the ALPGEN+PYTHIA and POWHEG+PYTHIA predictions which include parton shower radiation, and in which the non-perturbative QCD corrections are applied as part of the PYTHIA Monte Carlo event evolution, while in fixed order perturbative QCD predictions the corrections are estimated separately with ALPGEN+PYTHIA Monte Carlo and applied bin-by-bin. In the intermediate Z/γ^* p_T region the ratio of data over NLO MCFM, NLO+PS POWHEG+PYTHIA and $\bar{n}$NLO LOOPSIM+MCFM predictions show a slightly concave shape which is however covered by the scale variation uncertainty. In the high Z/γ^* p_T tail the measured cross section is slightly lower than theoretical predictions, but the difference is not statistically significant; the effect is probably correlated to the one observed in the jet p_T differential cross section. The NLO electroweak corrections related to the large Sudakov logarithms are negative and of the order of 5% in the last p_T bin.

Figure 5.14 shows the differential cross section as a function of Z/γ^*-leading jet $\Delta\phi$ in $Z/\gamma^* + \geqslant 1$ jet events. Also this variable is very sensitive to hard and soft jets radiation,

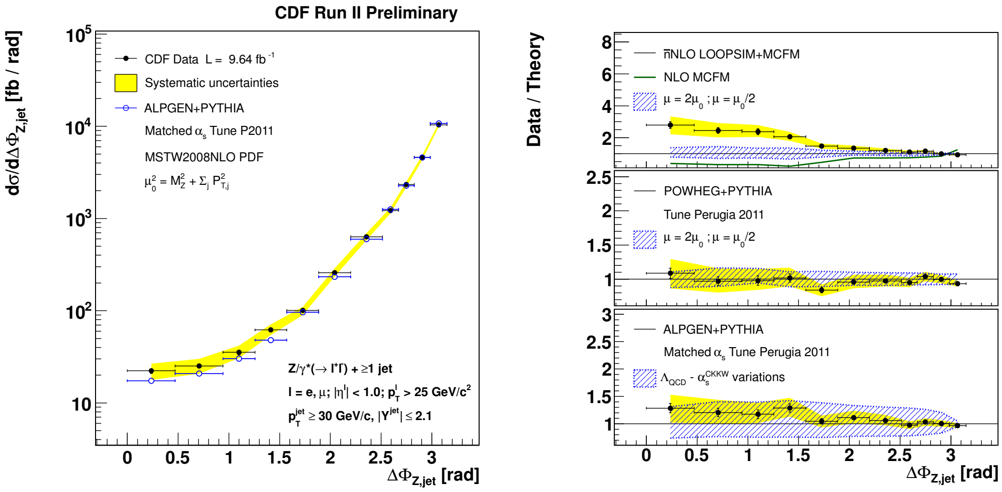

Figure 5.14: Z/γ^* + $\geqslant 1$ jet differential cross section as a function of Z/γ^*-jet $\Delta\phi$.

since Z/γ^* + exactly 1 jet configuration peaks at $\Delta\phi = \pi$. The region above $\Delta\phi = \pi/2$ is dominated by the Z/γ^* + 2 jets configuration, while in the region below $\Delta\phi = \pi/2$ almost only contributes the Z/γ^* + 3 jets configuration. In fact for transverse momentum conservation in a Z/γ^* + 2 jets event the leading jet has to be in the opposite hemisphere with respect to the Z/γ^*, leading to $\Delta\phi_{Z-jet} \geqslant \pi/2$; a Z/γ^* + 2 jets event can appear in the region below $\Delta\phi = \pi/2$ only if the real leading jet is unobserved because it exceeds the rapidity threshold of 2.1. ALPGEN+PYTHIA shows a good agreement with the measured cross section in the region above $\Delta\phi = \pi/2$. In the region below $\Delta\phi = \pi/2$ the ALPGEN+PYTHIA prediction is slightly lower than the data, but the difference is covered by the scale variation uncertainty. POWHEG+PYTHIA have a very good agreement in all the Z/γ^*-jet $\Delta\phi$ spectrum and is affected by a lower scale variation uncertainty. The difference between the ALPGEN+PYTHIA and POWHEG+PYTHIA predictions is of the same order of the experimental systematic uncertainty, which main contribution comes from the multiple p$\bar{\text{p}}$ interaction uncertainty, for this reason the measured cross section cannot be used to distinguish between the two models. NLO MCFM fails to describe the region below $\Delta\phi = \pi/2$ because it lacks the Z/γ^* + 3 jets configuration, while n̄NLO LOOPSIM+MCFM shows a considerable improvement of the perturbative QCD prediction in this region. This region is however affected by large non-perturbative QCD corrections of the order of 20 − 40% as shown in 5.1, which makes the comparison with fixed order perturbative QCD predictions not very meaningful.

5.5 Z/γ^* + $\geqslant 2$ jets differential cross sections

Z/γ^* $\geqslant 2$ jets production is an important background to the search for resonances in the Z/γ^*+X→lljj and X→ZZ→lljj channels, including the Higgs Boson. The Z/γ^* + $\geqslant 2$ jets process is also a background to searches for supersymmetry in $\not{E}_T$+ $\geqslant 2$ jets final state, when the Z/γ^* decays into neutrinos. For this reason the validation of theoretical predictions for this process is of fundamental importance in the context of Higgs and beyond the Standard Model searches. In this section the $Z/\gamma^* + \geqslant 2$ jets final state is analyzed looking at a larger set of differential cross sections, the measured cross section in $Z/\gamma^* + \geqslant 2$ jets final state are compared to ALPGEN+PYTHIA and NLO MCFM or BLACKHAT+SHERPA predictions. The LO-ME+PS ALPGEN+PYTHIA prediction is a commonly used tool to estimated the $Z/\gamma^* + 2$ jets background contribution. It includes parton shower, hadronization and multi-parton interactions, and a full detector simulation can be run on top of this Monte Carlo. On the other hand NLO perturbative QCD predictions have reduced scale variation uncertainty.

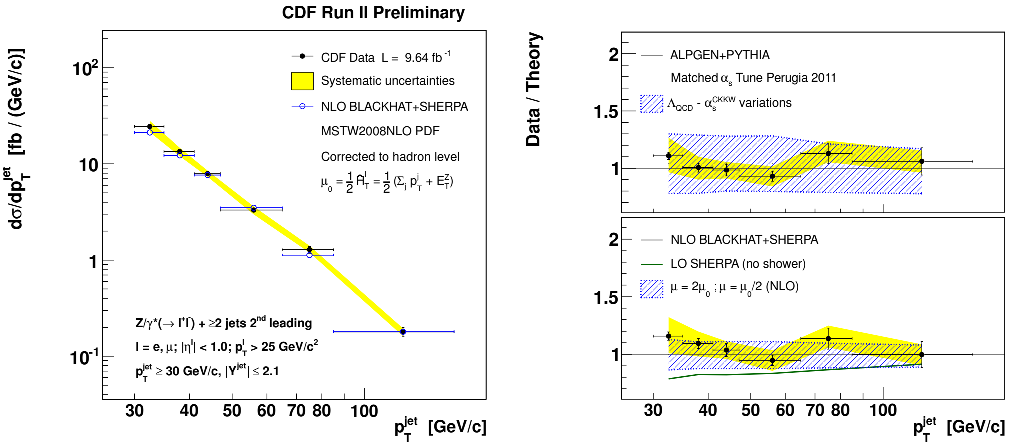

Figure 5.15: $Z/\gamma^* + \geqslant 2$ jets differential cross section as a function of 2^{nd} leading jet p_T. Measured cross section (black dots) is compared to the BLACKHAT+SHERPA NLO prediction (open circles). The yellow bands show the total systematic uncertainty, except for the 5.8% uncertainty on the luminosity. Right boxes show data/theory ratio with respect to ALPGEN+PYTHIA and BLACKHAT+SHERPA predictions, the blue dashed band show the scale uncertainty of each prediction.

Figures 5.15 and 5.16 shows the measured cross section as a function of the 2^{nd} leading jet p_T and inclusive jet rapidity compared to ALPGEN+PYTHIA and BLACKHAT+SHERPA predictions, Figure 5.17 shows the Z/γ^* p_T distribution compared to ALPGEN+PYTHIA and MCFM. All the distributions show a good agreement with the theoretical predictions.

Figures 5.18 shows the measured cross section as a function of the di-jet mass M_{jj}. The first bin at M_{jj} $40 - 60$ GeV/c^2 is overestimated by the MCFM prediction, but correctly described by the ALPGEN+PYTHIA prediction. The low M_{jj} region is probably more sensitive to soft radiation, which is better modeled by the PYTHIA parton shower than in a fixed order QCD calculation. In the high M_{jj} region above ~ 160 GeV/c^2 measured cross sections are $10 - 20\%$ higher than both predictions. Notice however that the systematic uncertainty, mainly due to the jet energy scale, is quite as large as the observed discrepancy, and that the matching scale variation uncertainty of the ALPGEN+PYTHIA prediction covers the difference between data and theory.

Figures 5.19 and 5.20 shows different PDF sets, scale choices, matching parameters and tunes for the ALPGEN+PYTHIA and MCFM theoretical predictions, but none of these

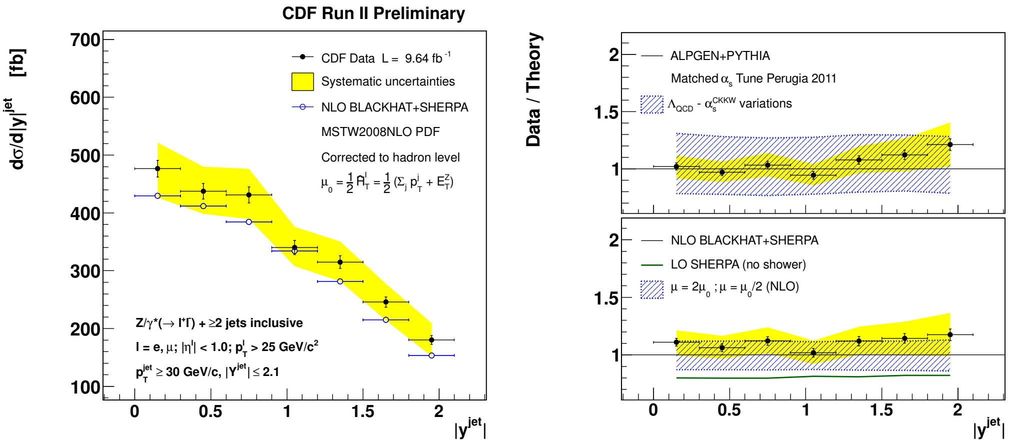

Figure 5.16: $Z/\gamma^* + \geqslant 2$ jets differential cross section as a function of inclusive jet rapidity.

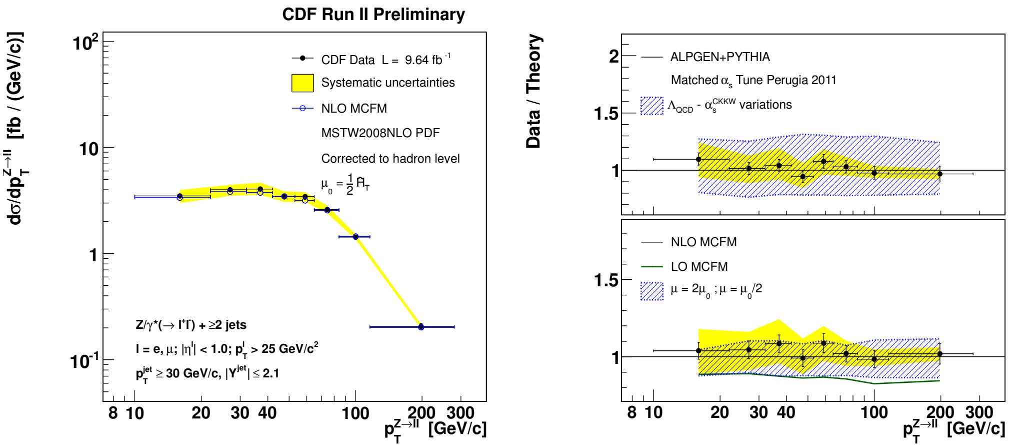

Figure 5.17: $Z/\gamma^* + \geqslant 2$ jets differential cross section as a function of Z/γ^* p_T.

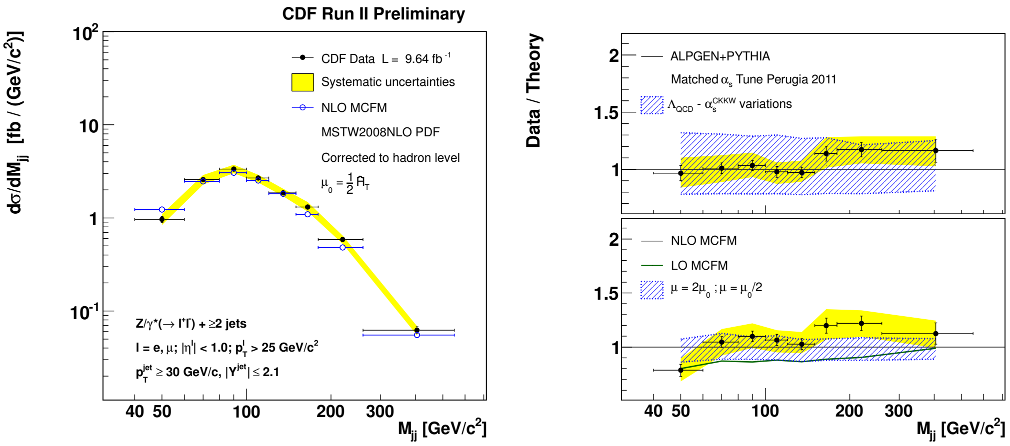

Figure 5.18: $Z/\gamma^* + \geqslant 2$ jets differential cross section as a function of di-jet mass M_{jj}.

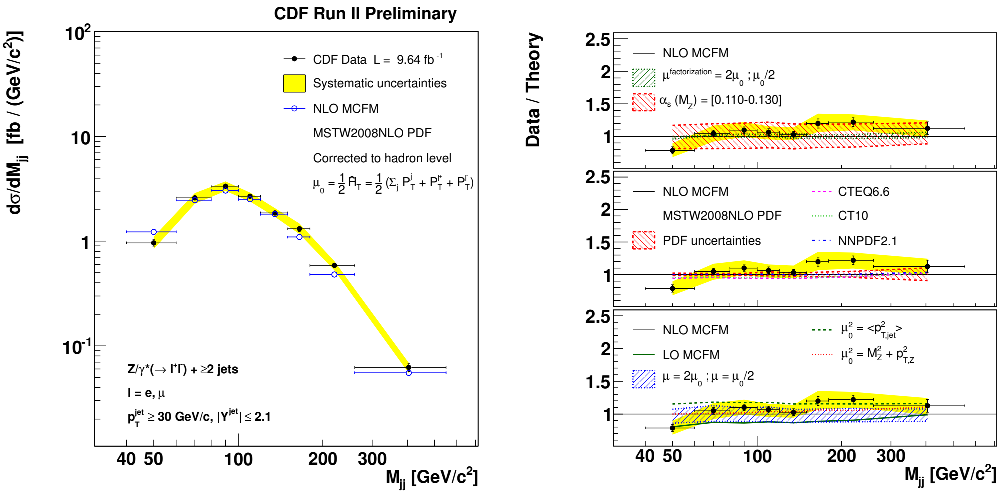

Figure 5.19: $Z/\gamma^* + \geqslant 2$ jets differential cross section as a function of di-jet mass M_{jj}. Measured cross section (black dots) is compared to the MCFM NLO prediction (open circles). Right boxes show data/theory ratio and variations of settings and parameters of the MCFM prediction: factorization scale variations, variations of $\alpha_s(M_Z)$, different PDF sets and PDF uncertainties, renormalization and factorization scale μ variations and different choices of the functional form of μ.

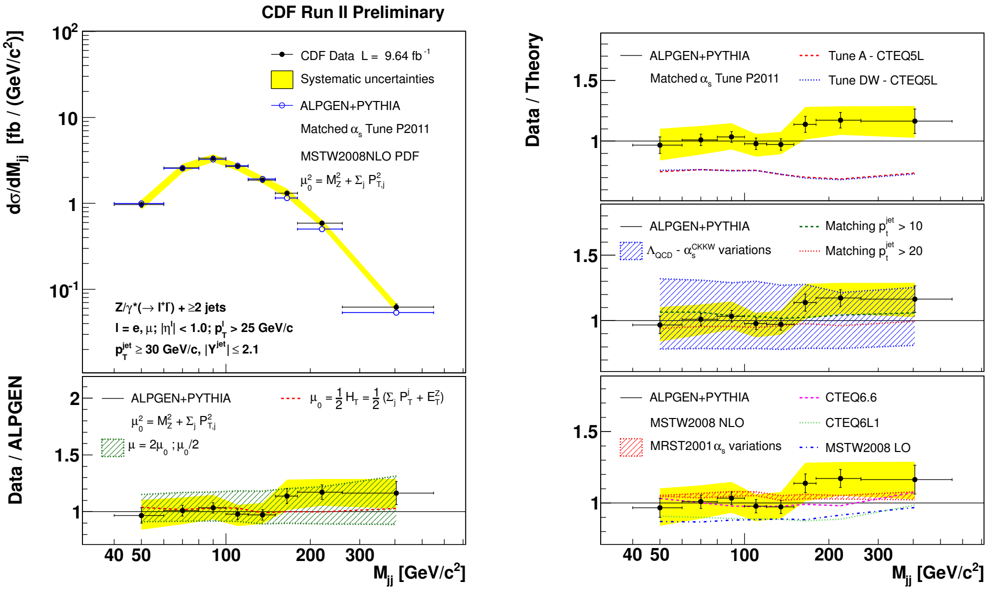

Figure 5.20: $Z/\gamma^* + \geqslant 2$ jets differential cross section as a function of di-jet mass M_{jj}. Measured cross section (black dots) is compared to the ALPGEN+PYTHIA LO-ME+PS prediction (open circles). Lower and right boxes show data/theory ratio and variations of settings and parameters of the ALPGEN+PYTHIA prediction: variations of the matrix elements renormalization and factorization scale μ in ALPGEN, different choice of the functional form of μ, different PYTHIA tunes, simultaneous variations of the CKKW renormalization matching scale in ALPGEN and Λ_{QCD} in PYTHIA parton showers, different values of the jet p_T threshold for the MLM matching, different PDF sets and $\alpha_s(M_Z)$ variations.

variations show any shape difference in the higher M_{jj} region.

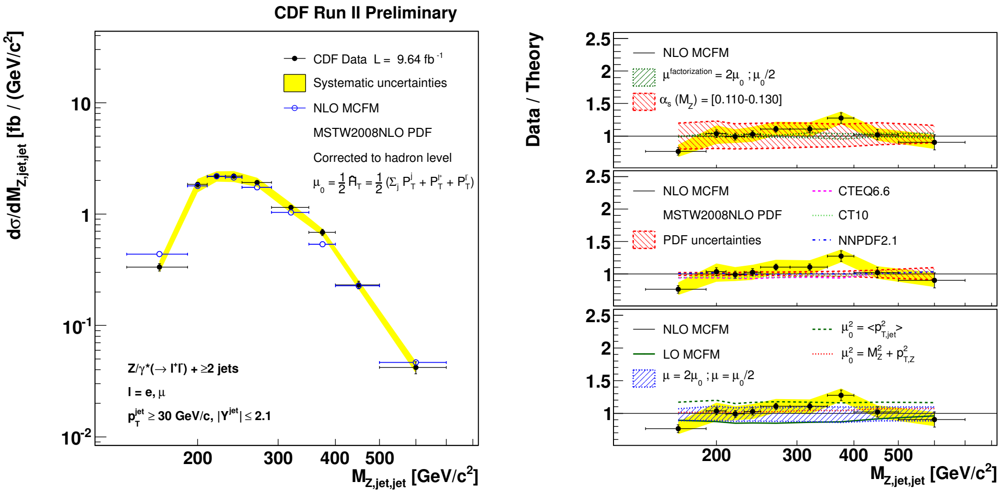

Figure 5.21: $Z/\gamma^* + \geqslant 2$ jets differential cross section as a function of Z/γ^*-jet-jet mass $M_{Z,jet,jet}$. Measured cross section (black dots) is compared to the MCFM NLO prediction (open circles), variations of settings and parameters of the MCFM prediction are shown.

Figures 5.21 and 5.22 show the measured cross section as a function of the Z/γ^*-jet-jet mass $M_{Z,jj}$. A reasonable agreement is observed within experimental and theoretical uncertainties.

Figures 5.23 shows the measured cross section as a function of the di-jet ΔR compared to ALPGEN+PYTHIA and MCFM predictions. Some disagreement is observed at high ΔR, where the measured cross section is $\sim 50\%$ higher than the theoretical predictions.

To better understand the origin of this disagreement the di-jet $\Delta\Phi$ and ΔY differential cross sections have been measured. Looking at Figures 5.24 and 5.25 the di-jet $\Delta\Phi$ appears reasonably modeled by the ALPGEN+PYTHIA and MCFM predictions, while the di-jet ΔY shows a shape discrepancy which is as large as 50% at $\Delta Y = 3 - 3.6$, and is probably related to the observed difference between data and theory at $\Delta R \gtrsim 4$.

Figures 5.26 and 5.27 show variations on the ALPGEN+PYTHIA and MCFM theoretical predictions for the di-jet ΔY distribution, none of these variations show any correlation with the observed data-theory discrepancy.

Finally Figure 5.28 shows the measured cross section as a function of the dihedral angle $\theta_{Z,jj}$ between the $Z/\gamma^* \to l^+l^-$ decay plane and the jet-jet plane. $\theta_{Z,jj}$ is defined as $\theta_{Z,jj} = \arccos \frac{(\vec{l_1} \times \vec{l_2}) \cdot (\vec{j_1} \times \vec{j_2})}{|\vec{l_1} \times \vec{l_2}||\vec{j_1} \times \vec{j_2}|}$, where $\vec{l}$ and $\vec{j}$ are the momentum 3-vectors of leptons and jets. In case a new resonance X which decays as X→ZZ→lljj is found, this variable could be used to study the spin properties of the new particle.

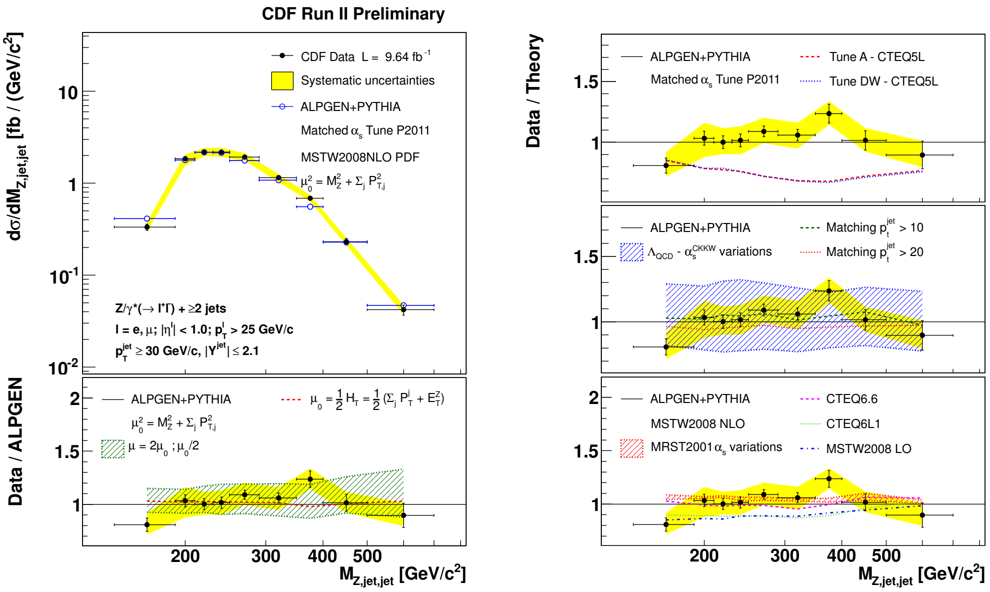

Figure 5.22: Z/γ^* + $\geqslant 2$ jets differential cross section as a function of Z/γ^*-jet-jet mass $M_{Z,jet,jet}$. Measured cross section (black dots) is compared to the ALPGEN+PYTHIA LO-ME+PS prediction (open circles), variations of settings and parameters of the ALPGEN+PYTHIA prediction are shown.

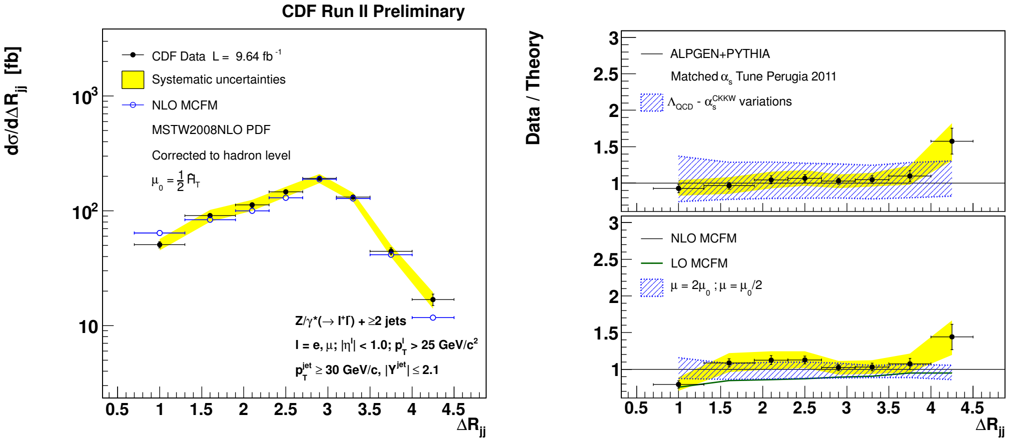

Figure 5.23: Z/γ^* + $\geqslant 2$ jets differential cross section as a function of di-jet ΔR.

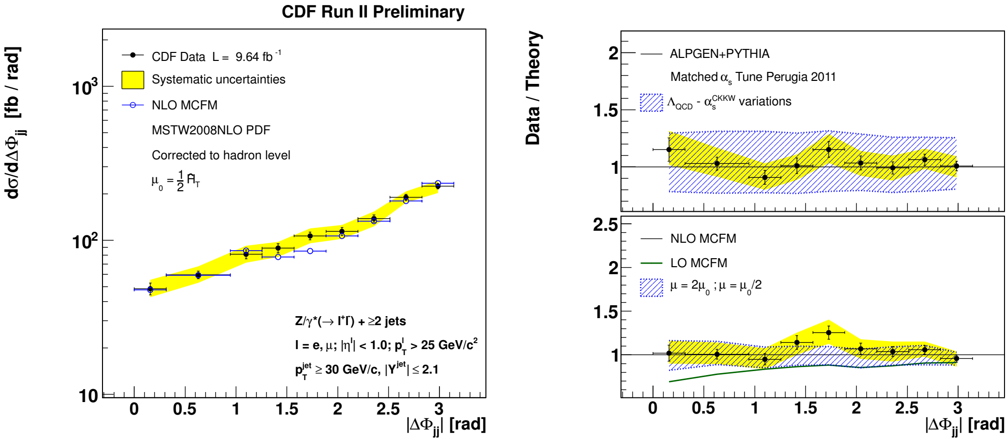

Figure 5.24: $Z/\gamma^* + \geqslant 2$ jets differential cross section as a function of di-jet $\Delta\Phi$.

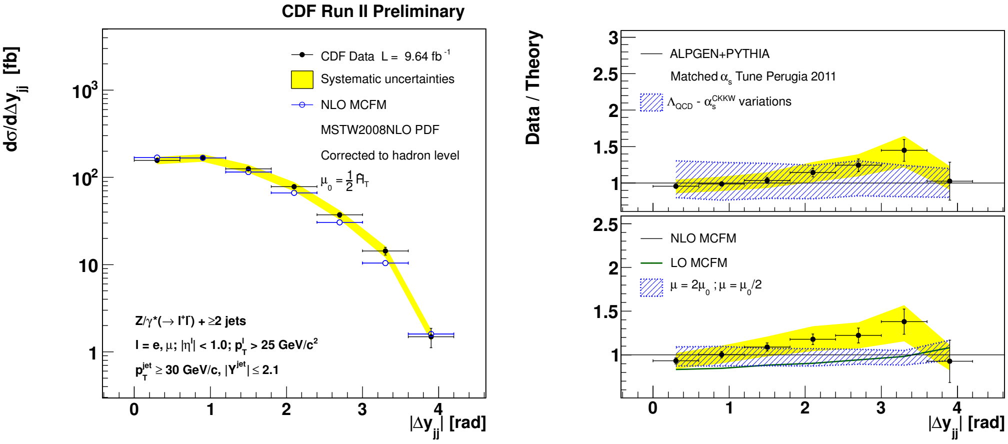

Figure 5.25: $Z/\gamma^* + \geqslant 2$ jets differential cross section as a function of di-jet ΔY.

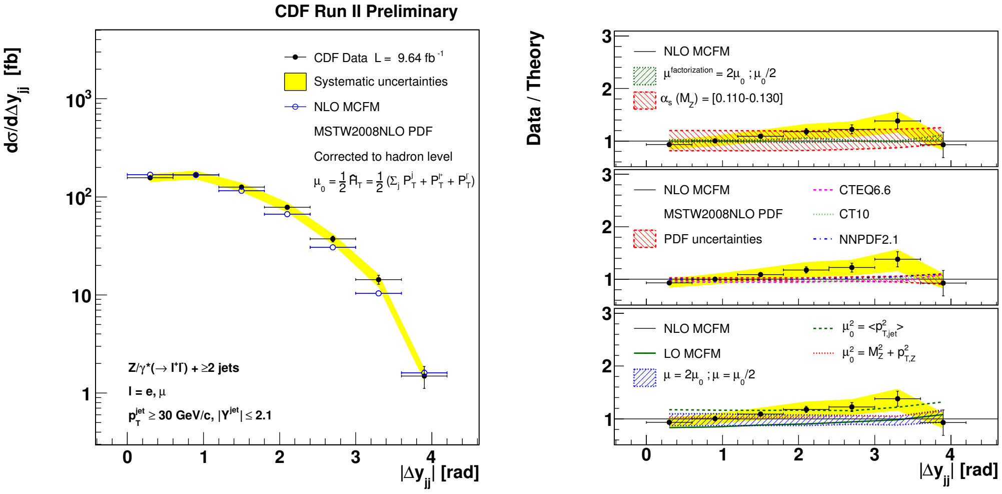

Figure 5.26: $Z/\gamma^* + \geqslant 2$ jets differential cross section as a function of di-jet ΔY. Measured cross section (black dots) is compared to the MCFM NLO prediction (open circles), variations of settings and parameters of the MCFM prediction are shown.

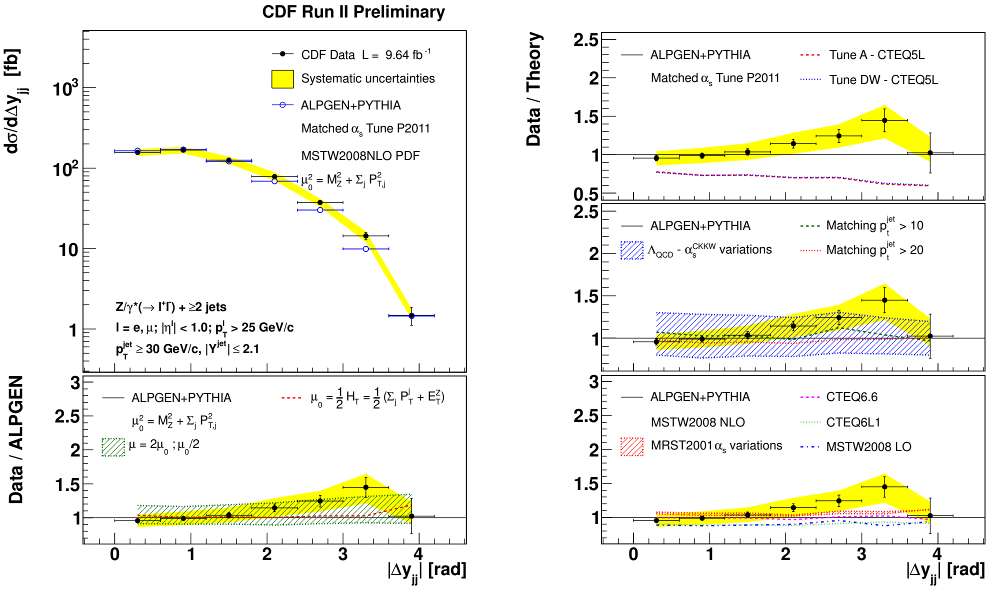

Figure 5.27: $Z/\gamma^* + \geqslant 2$ jets differential cross section as a function of di-jet ΔY. Measured cross section (black dots) is compared to the ALPGEN+PYTHIA LO-ME+PS prediction (open circles), variations of settings and parameters of the ALPGEN+PYTHIA prediction are shown.

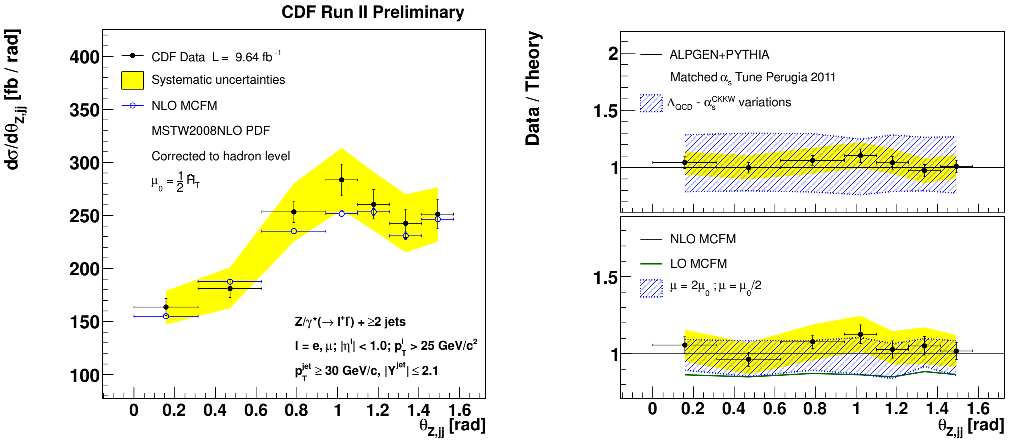

Figure 5.28: $Z/\gamma^* + \geqslant 2$ jets differential cross section as a function of the dihedral angle $\theta_{Z,jj}$.

5.6 $Z/\gamma^* + \geqslant N$ jets cross section

The $Z/\gamma^* + \geqslant N$ jets production cross sections are measured up to $Z/\gamma^* + \geqslant 4$ jets and compared to LO and NLO perturbative QCD BLACKHAT+SHERPA, LO-ME+PS ALPGEN+PYTHIA, and NLO+PS POWHEG+PYTHIA predictions. The $Z/\gamma^* + \geqslant 1$ jet cross section is compared also to the $\bar{\text{n}}$NLO LOOPSIM+MCFM prediction.

Figure 5.29 shows the inclusive cross section as a function of jet multiplicity for $Z/\gamma^* + \geqslant 1$, 2, 3 and 4 jets, the measured cross section is in general good agreement with all the predictions. The ALPGEN+PYTHIA LO-ME+PS prediction properly describes the measured cross sections, but has large theoretical uncertainty at higher jet multiplicities. BLACKHAT+SHERPA is the only available NLO perturbative QCD prediction for $Z/\gamma^* + \geqslant 3$ jets, and shows a reduced scale dependence with respect to the ALPGEN+PYTHIA LO-ME+PS prediction. The POWHEG+PYTHIA NLO+PS prediction has NLO accuracy only for $Z/\gamma^* + \geqslant 1$ jet, however it can be compared to data in all the measured jet multiplicities, where it shows a general good agreement. The LOOPSIM+MCFM $\bar{\text{n}}$NLO prediction is currently available only for $Z/\gamma^* + \geqslant 1$ jet NLO+PS, where it shows a very good agreement with the measured cross section and a reduced scale uncertainty at the level of 5%. Thanks to the improved accuracy of the $\bar{\text{n}}$NLO prediction, in this comparison the theoretical uncertainty is lower than the experimental systematic uncertainty.

The $Z/\gamma^* + \geqslant 3$ jets BLACKHAT+SHERPA NLO perturbative QCD calculation appears to be $\sim 30\%$ lower than data, with the difference covered by the scale variation uncertainty. Such difference is not observed in the comparison with LO-ME+PS ALPGEN+PYTHIA and NLO+PS POWHEG+PYTHIA predictions, and also recent measurements of $Z/\gamma^* +$ jets with the ATLAS detector using the anti-kt the jet algorithm [85] do not show any difference with the NLO predictions at high jet multiplicities.

To clarify the picture, fixed order LO and NLO BLACKHAT+SHERPA calculations have been compared to LO-ME+PS ALPGEN+PYTHIA predictions both with SISCone and anti-kt jet algorithms, results are shown in Tables 5.1 and 5.2.

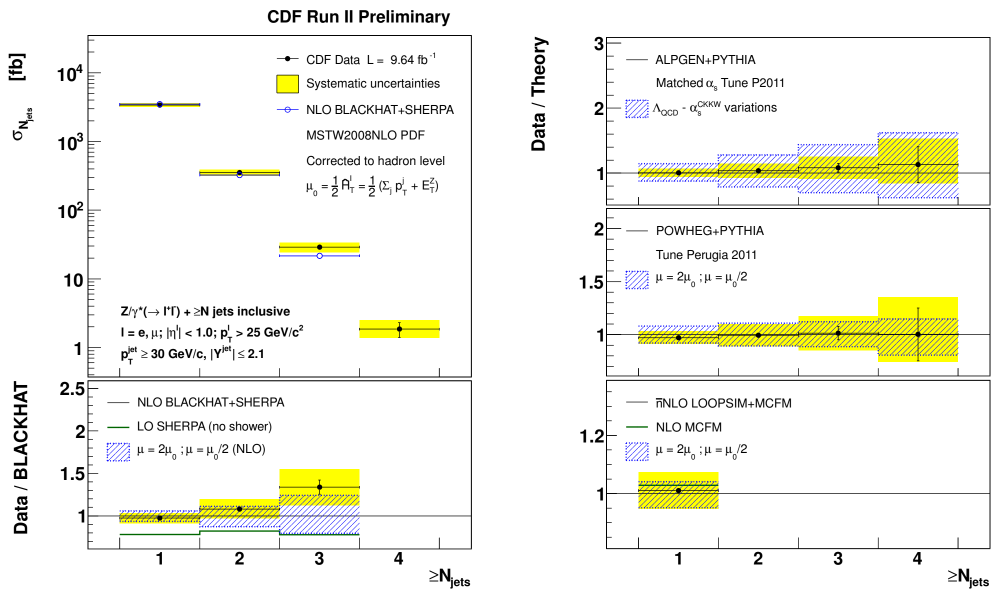

Figure 5.29: $Z/\gamma^* + \geqslant N$ jets inclusive cross section as a function of jet multiplicity. Measured cross section (black dots) is compared to the BLACKHAT+SHERPA NLO prediction (open circles). The yellow bands show the total systematic uncertainty, except for the 5.8% uncertainty on the luminosity. Lower and right boxes show data/theory ratio with respect to other theoretical predictions, the blue dashed band show the scale uncertainty of each prediction.

SISCone				
	non-pQCD	LO × non-pQCD	NLO × non-pQCD	LO-ME+PS
$Z/\gamma^* + \geqslant 1$ jet	1.032	2635	3381	3240
$Z/\gamma^* + \geqslant 2$ jets	1.051	257.4	313.5	320.6
$Z/\gamma^* + \geqslant 3$ jets	1.050	15.8	20.3	24.1
$Z/\gamma^* + \geqslant 4$ jets	1.097	0.69	/	1.50
anti-kt				
	non-pQCD	LO × non-pQCD	NLO × non-pQCD	LO-ME+PS
$Z/\gamma^* + \geqslant 1$ jet	1.086	2772	3384	3297
$Z/\gamma^* + \geqslant 2$ jets	1.113	307.3	336.5	339.3
$Z/\gamma^* + \geqslant 3$ jets	1.12	26.3	27.1	27.9
$Z/\gamma^* + \geqslant 4$ jets	1.129	1.83	/	1.87

Table 5.1: SISCone and anti-kt $Z/\gamma^* + \geqslant N$ jets cross sections in fb as predicted with LO and NLO BLACKHAT+SHERPA and LO-ME+PS ALPGEN+PYTHIA.

NLO/LO K-factor			
	$Z/\gamma^* + \geqslant 1$ jet	$Z/\gamma^* + \geqslant 2$ jets	$Z/\gamma^* + \geqslant 3$ jets
SISCone	1.28	1.22	1.28
anti-kt	1.22	1.10	1.03
LO-ME+PS/NLO ratio			
	$Z/\gamma^* + \geqslant 1$ jet	$Z/\gamma^* + \geqslant 2$ jets	$Z/\gamma^* + \geqslant 3$ jets
SISCone	0.96	1.02	1.19
anti-kt	0.97	1.01	1.03

Table 5.2: SISCone and anti-kt NLO/LO and LO-ME+PS/NLO ratios of $Z/\gamma^* + \geqslant N$ jets cross sections as predicted with LO and NLO BLACKHAT+SHERPA and LO-ME+PS ALPGEN+PYTHIA.

SISCone predictions show larger NLO/LO K-factor with respect to anti-kt, and the LO-ME+PS/NLO ratio grows up with the jet multiplicity, pointing out that SISCone is more sensitive to higher-order perturbative corrections in high jet multiplicity environment. On the other hand the anti-kt jet algorithm shows a lower NLO/LO K-factor, and the ratio of the LO-ME+PS prediction with the NLO cross section is quite independent from the jet multiplicity.

Perturbative radiation can influence the reach of a jet algorithm, that is the largest distance for two hard partons to be recombined into a single jet. SISCone and anti-kt jet algorithms have a rather different behaviour as far as the jet reach is concerned, as discussed in [14]. In the case of two particles with transverse momentum p_t^1, p_t^2 such that $p_t^2 = x \cdot p_t^1$, and angular distance ΔR_{12}, the condition for a jet algorithm to cluster them in a single jet is $\Delta R_{12} < (1+x)R$ for SISCone and $\Delta R_{12} < R$ for anti-kt. As a consequence two particles with similar p_t, for which $x \sim 1$, are clustered in the same jet by SISCone up to a distance $\Delta R_{12} \lesssim 2R$, while they end up in the same anti-kt jet only if $\Delta R_{12} < R$. The lower jet reach of the anti-kt algorithm determines higher LO cross sections at high jet multiplicity, because of the lower probability of N partons to be recombined in $n < N$ jets. The same [14] shows how higher-order perturbative radiation can influence the jet reach, for SISCone with $R = 0.4$ and $f = 0.75$ the reach of SISCone is limited at parton showered level to $\Delta R_{12} \lesssim 1.6R$, while for the anti-kt algorithm the condition $\Delta R_{12} < R$ keeps valid. Even if in most cases the reduced reach of the jet algorithm in the presence of perturbative radiation is not expected to have a large impact, in the past an artificial parameter R_{sep} was introduced for seedless cone jet algorithm to model the impact on the jet reach of higher-order and non-perturbative corrections in fixed order QCD predictions. R_{sep} modifies the reach of a seedless cone algorithm in a perturbative QCD calculation by limiting the clustering to $\Delta R_{12} < R_{sep} \cdot R$. As argued in [14] the introduction of this parameter defeats the purpose of a NLO calculation, and has not been used in the BLACKHAT+SHERPA fixed order predictions. Nevertheless in this context R_{sep} can be used to quantify the impact on the fixed order cross sections of modifying the reach of the jet algorithm. Table 5.3 shows LO and NLO predictions evaluated with the SISCone jet algorithm in BLACKHAT+SHERPA and with the seedless cone algorithm of MCFM with the additional $R_{sep} = 1.3$ parameter. While the introduction of R_{sep} has a negligible or small impact in the $Z/\gamma^* + \geqslant 1$ jet and $Z/\gamma^* + \geqslant 2$ jets cross sections, in $Z/\gamma^* + \geqslant 3$ jets LO predictions it determines a 30% variation. In conclusion the difference between data and LO-ME+PS with respect to the NLO prediction in $Z/\gamma^* + \geqslant 3$ jets final state can be explained with the presence of higher order perturbative radiation, which reduces

LO perturbative QCD		
	BLACKHAT+SHERPA SISCone	MCFM $R_{sep} = 1.3$
$Z/\gamma^* + \geqslant 1$ jet	2553	2589
$Z/\gamma^* + \geqslant 2$ jets	244.9	266.3
$Z/\gamma^* + \geqslant 3$ jets	15.0	19.6
$Z/\gamma^* + \geqslant 4$ jets	0.63	/
NLO perturbative QCD		
	BLACKHAT+SHERPA SISCone	MCFM $R_{sep} = 1.3$
$Z/\gamma^* + \geqslant 1$ jet	3276	3244
$Z/\gamma^* + \geqslant 2$ jets	298.3	307.5
$Z/\gamma^* + \geqslant 3$ jets	19.3	/

Table 5.3: LO and NLO $Z/\gamma^* + \geqslant N$ jets cross sections in fb as predicted with SISCone and MCFM native cone algorithm with $R_{sep} = 1.3$. At higher jet multiplicity the introduction of R_{sep} has a larger impact on the cross section.

the jet reach of the SISCone algorithm and increases the cross section in this particular configuration.

Finally it is important to remark that the jet radius used for the measurement $R = 0.7$ can play an important role in high jet multiplicity environments and enhance the observed difference with respect to smaller jet radius used in other measurements, like for instance the W + jets measurement performed with the D0 detector [86].

5.7 Comparison with LOOPSIM n̄NLO prediction

As discussed in [28], some Z/γ^* + jets observables show larger NLO-LO K-factor and are expected to have significant beyond NLO corrections. The most remarkable example is the H_T^{jet}, defined as $H_T^{\text{jet}} = \sum p_T^{\text{jet}}$, in $Z/\gamma^* + \geqslant 1$ jet events. Figure 5.30 shows the measured cross section as a function of H_T^{jet} compared to the available theoretical predictions. The NLO MCFM prediction fails to describe the shape of the H_T^{jet} distribution, in particular it underestimates the measured cross section in the high p_T tail where a NLO-LO K-factor $\gtrsim 2$ and a larger NLO scale variation uncertainty is observed. The LO-ME+PS ALPGEN+PYTHIA prediction is in good agreement with data, but suffers for the large LO scale uncertainty. Also the POWHEG+PYTHIA is in good agreement with data, but is still affected by the larger NLO scale uncertainty in the high p_T tail. The n̄NLO LOOPSIM+MCFM prediction properly model the data distribution, and shows a significantly reduced scale uncertainty.

Another observable which shows some significant n̄NLO correction is the leading lepton p_T in $Z/\gamma^* + \geqslant 1$ events. Figure 5.31 shows the measured cross section compared to LO and NLO MCFM prediction and to the n̄NLO LOOPSIM+MCFM prediction. In this case the NLO-LO K-factor has a minimum at ~ 65 GeV/c where it is 1.1, and the corresponding n̄NLO correction is negative.

In many other $Z/\gamma^* + \geqslant 1$ jet measured variables the LOOPSIM+MCFM n̄NLO prediction does not show significant differences with respect to the NLO prediction, anyway is has a reduced scale uncertainty, as already observed for instance in Figures 5.12 and 5.29.

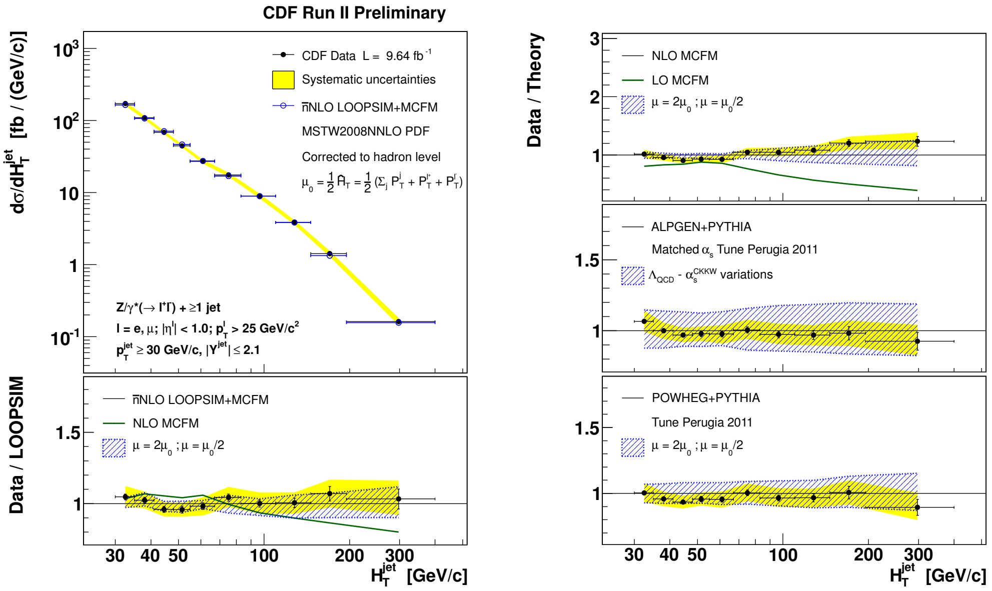

Figure 5.30: $Z/\gamma^* + \geqslant 1$ jets differential cross section as a function of $H_T^{\text{jet}} = \sum_j p_T^j$. Measured cross section (black dots) is compared to the LOOPSIM+MCFM n̄NLO prediction (open circles). The yellow bands show the total systematic uncertainty, except for the 5.8% uncertainty on the luminosity. Lower and right boxes show data/theory ratio with respect to other theoretical predictions, the blue dashed band show the scale uncertainty of each prediction.

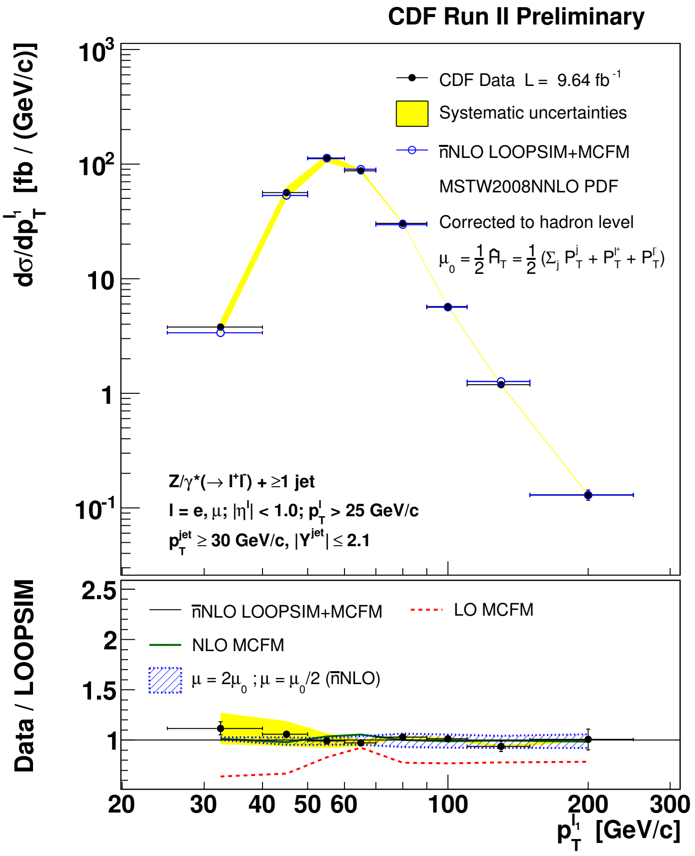

Figure 5.31: $Z/\gamma^* + \geqslant 1$ jets differential cross section as a function of leading lepton p_T.

5.8 Comparison with BLACKHAT NLO prediction

BLACKHAT+SHERPA is the only available NLO perturbative QCD prediction for $Z/\gamma^* + \geqslant 3$ jets.

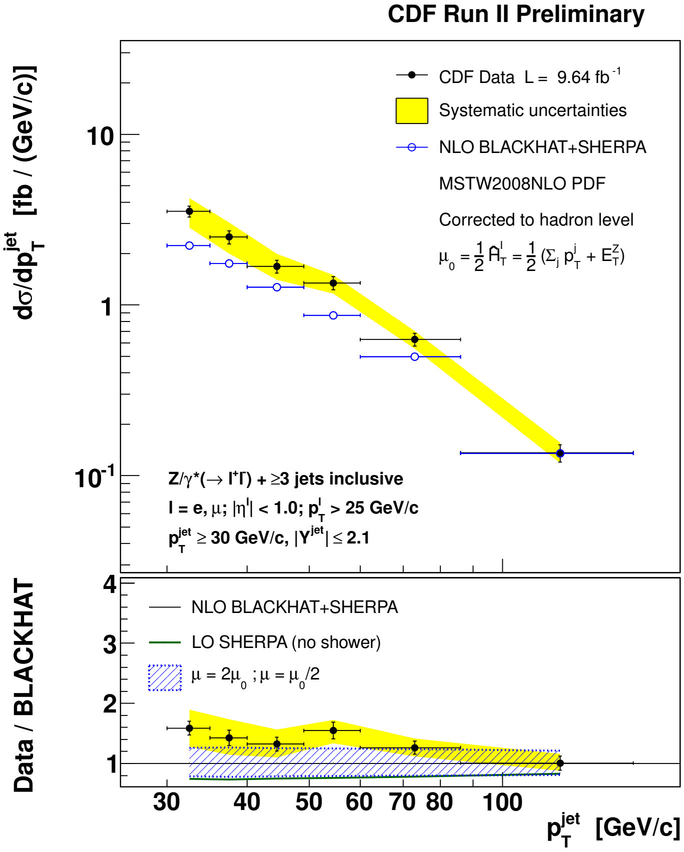

Figure 5.32: $Z/\gamma^* + \geqslant 3$ jets differential cross section as a function of inclusive jet p_T. Measured cross section (black dots) is compared to the BLACKHAT+SHERPA NLO prediction (open circles).

Figures 5.32 and 5.33 show the differential cross sections as a functions of inclusive jet and 3^{rd} leading jet p_T in events with a reconstructed $Z/\gamma^* \to l^+l^-$ and at least 3 jets, Figures 5.34 and 5.35 show the inclusive jet rapidity and the H_T^{jet} differential cross sections. As already discussed in section 5.6 the NLO BLACKHAT+SHERPA prediction is $\sim 30\%$ lower than the measured cross sections for $Z/\gamma^* + \geqslant 3$ jets events, however data and predictions are still compatible within the large scale variation uncertainty which is of the order of 25%, and the experimental systematic uncertainty which is $\sim 15\%$ and dominated by the jet energy scale. Apart from the difference in the normalization, the shape of the measured differential cross sections is in good agreement with the NLO BLACKHAT+SHERPA prediction.

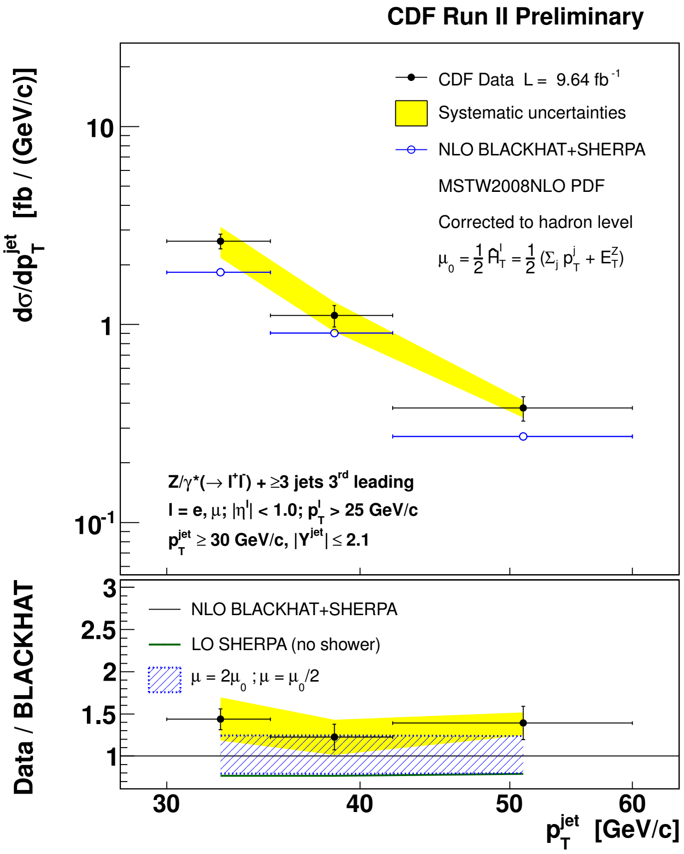

Figure 5.33: $Z/\gamma^* + \geqslant 3$ jets differential cross section as a function of 3rd leading jet p_T. Measured cross section (black dots) is compared to the BLACKHAT+SHERPA NLO prediction (open circles).

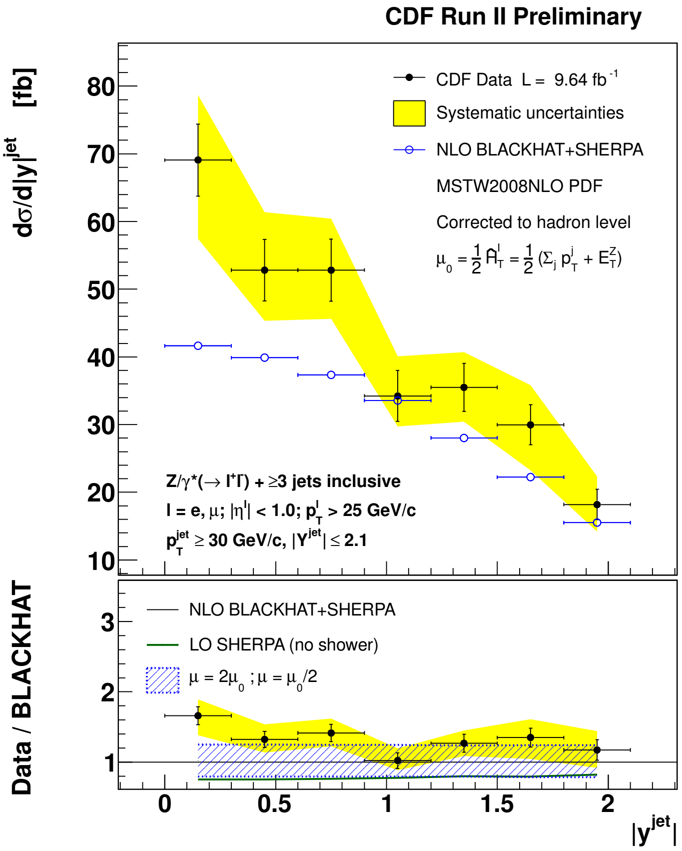

Figure 5.34: Z/γ^* + $\geqslant$ 3 jets differential cross section as a function of inclusive jet rapidity. Measured cross section (black dots) is compared to the BLACKHAT+SHERPA NLO prediction (open circles).

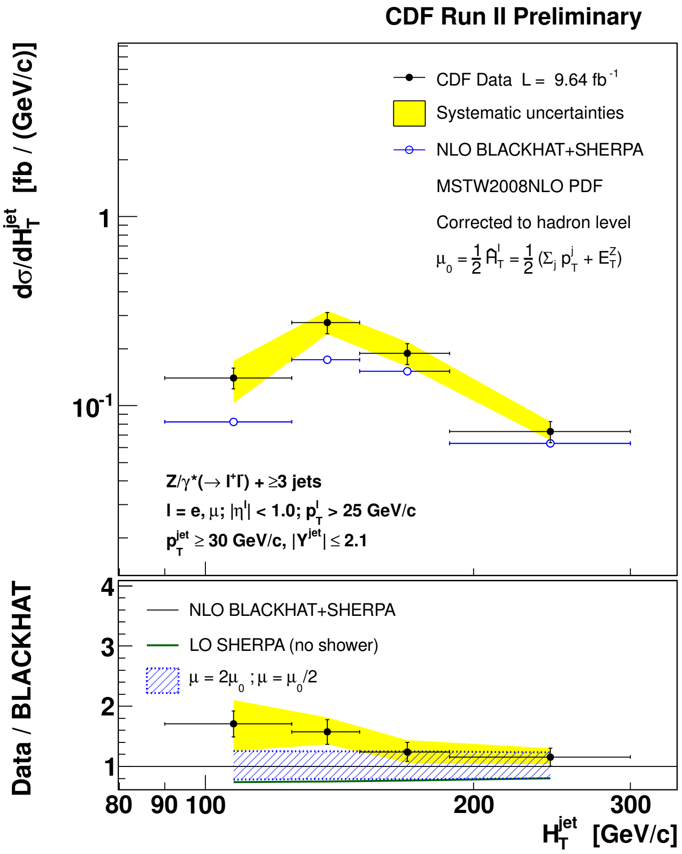

Figure 5.35: $Z/\gamma^* + \geqslant 3$ jets differential cross section as a function of $H_T^{\text{jet}} = \sum_j p_T^j$. Measured cross section (black dots) is compared to the BLACKHAT+SHERPA NLO prediction (open circles).

5.9 Comparison with ALPGEN LO-ME+PS matched prediction

The ALPGEN+PYTHIA prediction is a fundamental ingredient for the current $Z/\gamma^* +$ jets analysis, it is used to unfold the measurement at particle level and to evaluate the non-perturbative QCD corrections which are applied to the perturbative QCD predictions. This prediction is also commonly used at CDF and in other experiments to estimate the $Z/\gamma^* +$ jets background in Higgs boson and beyond the Standard Model searches. Therefore it is crucial to validate the ALPGEN+PYTHIA Monte Carlo modeling of $Z/\gamma^* +$ jets data, and thoroughly study the effects of generation parameters variations and the uncertainties of this prediction. The prediction has been evaluated with different PYTHIA tunes, the virtuality-ordered Tune A and Tune DW and the new p_T-ordered Tune Perugia 2011. The jet p_T threshold for the matrix elements generation has been varied to 10 GeV/c and 20 GeV/c with respect to the nominal values of 15 GeV/c, together with the corresponding MLM matching jet p_T threshold which is always set 5 GeV/c higher than the matrix elements generation jet threshold. An important feature of Tune Perugia 2011 is that values of Λ_{QCD} for the ISR, FSR and IFSR showers in PYTHIA are all set to the common values of $\Lambda_{QCD} = 0.26$ and 1-loop running order. The ALPGEN α_s-matched prescription set the same value of Λ_{QCD} and the same 1-loop running order also in the CKKW α_s reweight procedure. In this way the running of α_s is almost independent from the particular PDF used for the matrix elements generation in ALPGEN, and it is possible to test different PDF sets on the ALPGEN side. This was not possible with the previous PYTHIA tunes and ALPGEN settings, since in that case the α_s running was determined by the PDF set both in ALPGEN and in PYTHIA, and it was necessary to use the same PDF in both programs to avoid mismatch. Several PDF variations have been tested on top of the α_s-matched Tune Perugia 2011 settings, NLO 2-loop PDF sets like MSTW2008NLO, CTEQ6.6 and MRST2001 with α_s variations, and also LO 1-loop PDF sets as MSTW2008LO and CTEQ6L1 [84]. In the new α_s-matched setting the variation of the CKKW renormalization scale has to be performed together with the variation of Λ_{QCD} in PYTHIA, this variation generally leads to the larger uncertainty. Finally the variation of the renormalization and factorization scale for the ME generation has been studied, due to the later renormalization scale CKKW reweight this variation affects mostly the factorization scale.

Figure 5.36 shows the leading jet p_T in $Z/\gamma^* + \geqslant 1$ jet events. The α_s-matched Tune Perugia 2011 shows an improved agreement in the normalization with respect to previous Tune A and Tune DW, and the NLO 2-loop PDF sets better model the measured cross section than the LO 1-loop PDF. The red dashed band in the lower right box shows $\alpha_s(M_Z)$ variations of the MRST2001 PDFs in the range $0.117 - 0.121$, as expected the variation of α_s in the PDF set barely affect the prediction in the α_s-matched ALPGEN setting.

The ALPGEN+PYTHIA prediction provides a good modeling of Z/γ^* p_T distribution in the intermediate and low p_T region, as shown in Figure 5.37. The Z/γ^* p_T below the jet threshold of 30 GeV/c is sensitive to soft radiation, and the Tune Perugia 2011, which implements p_T-ordered parton showers, give an improved shape and normalization agreement in this region with respect to the virtuality-ordered Tune A and Tune DW. The factorization and renormalization scale variations show a larger uncertainty in the high p_T tails of Z/γ^* and leading jet distributions. A possible explication of such behaviour was suggested by the authors of the ALPGEN Monte Carlo. The factorization scale is passed as the hardest scale to the parton shower, and radiation above it is vetoed. Changing the factorization scale can affect the amount of ISR, and this can influence the jet-rejection

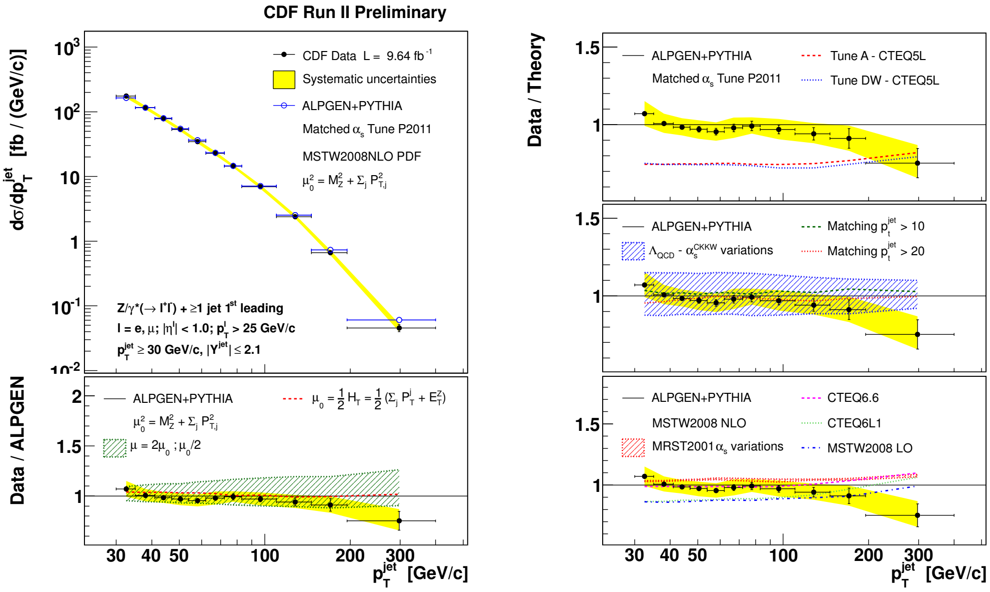

Figure 5.36: $Z/\gamma^* + \geqslant 1$ jets differential cross section as a function of leading jet p_T. Measured cross section (black dots) is compared to the ALPGEN+PYTHIA LO-ME+PS prediction (open circles). Lower and right boxes show data/theory ratio and variations of settings and parameters of the ALPGEN+PYTHIA prediction: variations of the matrix elements renormalization and factorization scale μ in ALPGEN, different choice of the functional form of μ, different PYTHIA tunes, simultaneous variations of the CKKW renormalization matching scale in ALPGEN and Λ_{QCD} in PYTHIA parton showers, different values of the jet p_T threshold for the MLM matching, different PDF sets and $\alpha_s(M_Z)$ variations.

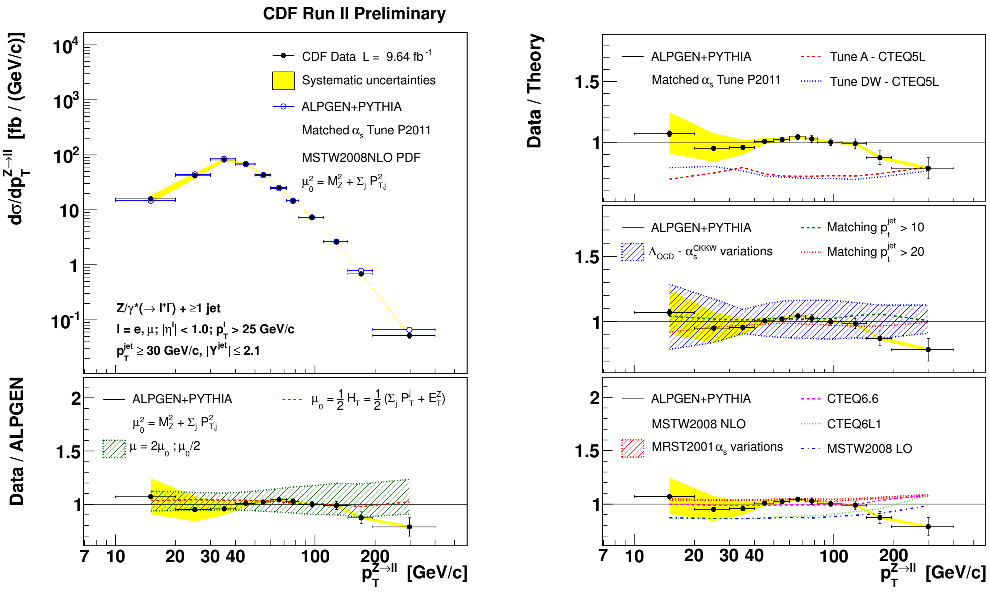

Figure 5.37: $Z/\gamma^* + \geqslant 1$ jets differential cross section as a function of Z/γ^* p_T. Measured cross section (black dots) is compared to the ALPGEN+PYTHIA LO-ME+PS prediction (open circles).

rate in the MLM matching algorithm. Higher values of the factorization scale give higher ISR jet activity, thus higher jet vetoing, and eventually smaller cross section rates.

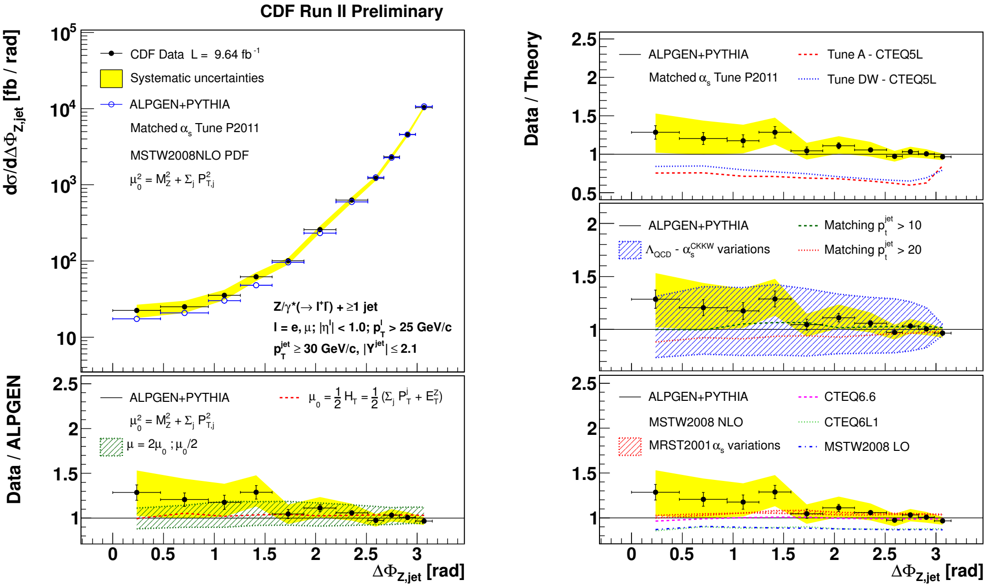

Figure 5.38: $Z/\gamma^* + \geqslant 1$ jets differential cross section as a function of Z/γ^*-jet $\Delta\phi$. Measured cross section (black dots) is compared to the ALPGEN+PYTHIA LO-ME+PS prediction (open circles).

Figure 5.38 shows the differential cross section as a function of Z/γ^*-leading jet $\Delta\phi$ in $Z/\gamma^* + \geqslant 1$ jet events compared to the ALPGEN+PYTHIA prediction. The α_s-matched Tune Perugia 2011 shows a significant improvement in the shape of this distribution with respect to Tune A and Tune DW.

Figure 5.39 shows the measured cross section as a function of inclusive jet rapidity in $Z/\gamma^* + \geqslant 1$ jet events compared to ALPGEN+PYTHIA prediction. The high rapidity tail of this distribution is the only notable disagreement with respect to other predictions, however the deviation is covered by the renormalization and α_s^{CKKW} scale variation uncertainty, which is the largest uncertainty associated to the ALPGEN+PYTHIA prediction.

Figure 5.40 shows the measured cross section as a function of inclusive jet p_T in $Z/\gamma^* + \geqslant 3$ jet events. The ALPGEN+PYTHIA prediction is found to give a general good agreement in all the distributions of $Z/\gamma^* + \geqslant 1$, 2 and 3 jets. In particular the new α_s-matched tune Perugia 2011 also provide the right normalization and a correct modeling of the measured cross section as a function of the jet multiplicity as shown in Figure 5.41.

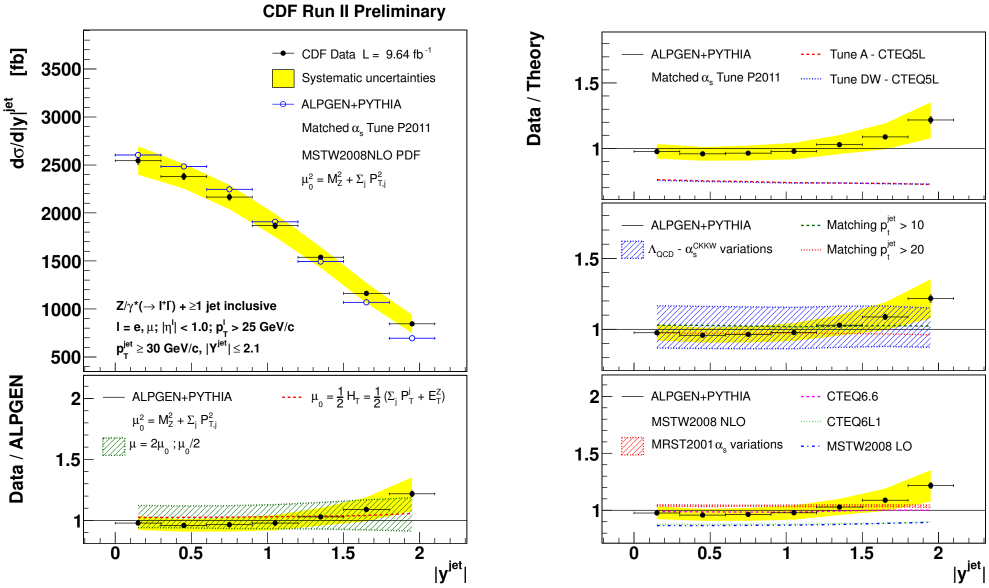

Figure 5.39: $Z/\gamma^* + \geqslant 1$ jets differential cross section as a function of inclusive jet rapidity. Measured cross section (black dots) is compared to the ALPGEN+PYTHIA LO-ME+PS prediction (open circles).

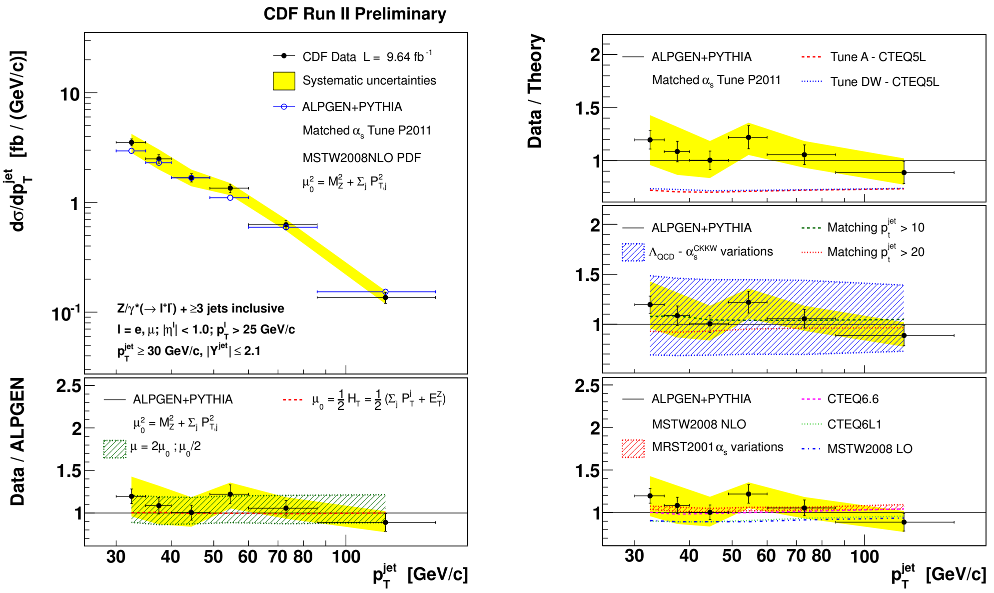

Figure 5.40: $Z/\gamma^* + \geqslant 3$ jets differential cross section as a function of inclusive jet p_T. Measured cross section (black dots) is compared to the ALPGEN+PYTHIA LO-ME+PS prediction (open circles).

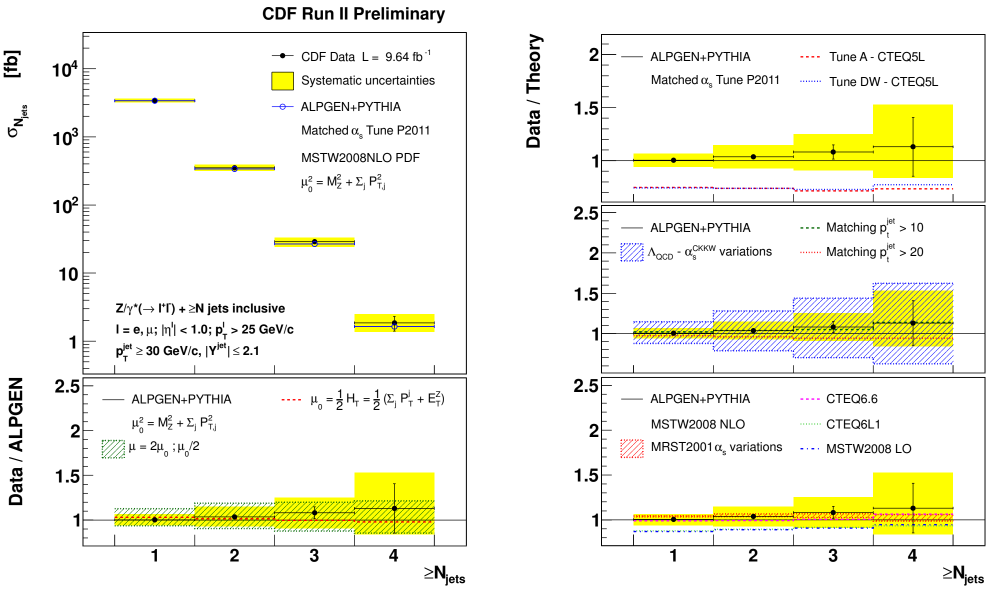

Figure 5.41: $Z/\gamma^* + \geqslant N$ jets inclusive cross section as a function of jet multiplicity. Measured cross section (black dots) is compared to the ALPGEN+PYTHIA LO-ME+PS prediction (open circles).

5.10 Comparison with POWHEG NLO+PS prediction

POWHEG is a method to interface a NLO perturbative QCD prediction to a parton shower Monte Carlo. The POWHEG NLO cross section was conceived to be independent from the particular parton shower Monte Carlo used, nevertheless parton shower tools are usually tuned on top of LO prediction, and it has been suggested by the authors that a tuning of the parton shower parameters on top of a NLO calculation could further improve the performance of the NLO+PS POWHEG prediction. The great advantage of the POWHEG approach is that hadronization and multi-parton interactions can be added to the NLO+PS prediction and a full detector simulation can be run on top of it. The resulting Monte Carlo can be used to estimate Z/γ^* + jets background contribution with NLO accuracy. The prediction has been evaluated with different PYTHIA tunes, the virtuality-ordered Tune A and Tune DW and the new p_T-ordered Tune Z1 and Tune Perugia 2011. MSTW2008NLO and CTEQ6.6 PDF sets have been used, and the impact of different choices of the renormalization and factorization scale has been studied. This last variation is not an option of the POWHEG release, but was introduced in the context of this measurement in agreement with the authors. Finally the variation of the factorization scale alone and of both the renormalization and factorization scales have been studied, the latter giving the most important source of uncertainty in the theoretical prediction.

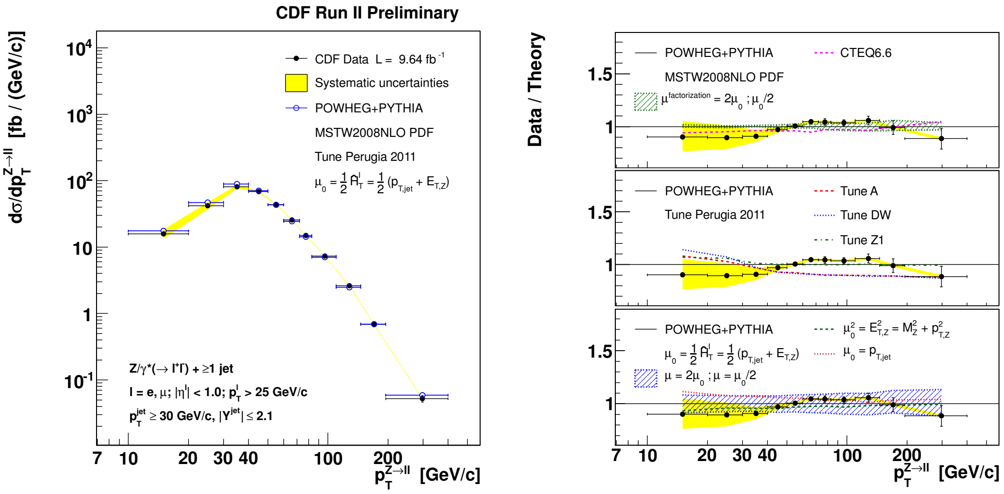

Figure 5.42: Z/γ^* + $\geqslant$ 1 jets differential cross section as a function of Z/γ^* p_T. Measured cross section (black dots) is compared to the POWHEG+PYTHIA NLO+PS prediction (open circles). Right boxes show data/theory ratio and variations of settings and parameters of the POWHEG+PYTHIA prediction: variations of the factorization scale, different PDF set, different PYTHIA tunes, variations of the renormalization and factorization scale μ and different choices of the functional form of μ,

Figure 5.42 shows the Z/γ^* p_T differential cross sections for Z/γ^* + $\geqslant$ 1 jet events compared to the POWHEG+PYTHIA prediction. Good agreement is observed in the low and intermediate p_T region, the disagreement at high p_T is common to all the prediction and was already discussed in section 5.4. The variation associated to different PYTHIA tunes is much lower than in the ALPGEN+PYTHIA prediction, this is a consequence of the independence of the POWHEG cross section from the particular parton shower employed, and an important advantage of the method.

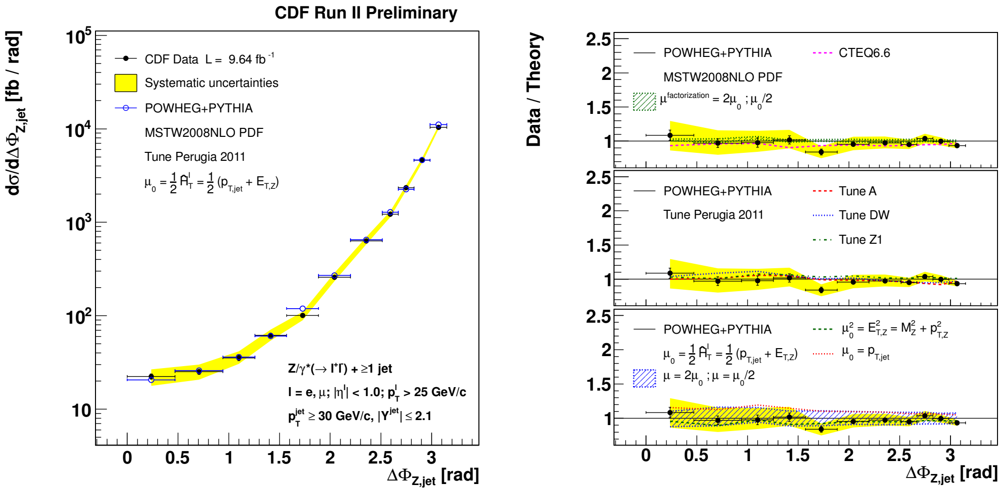

Figure 5.43: $Z/\gamma^* + \geqslant 1$ jets differential cross section as a function of Z/γ^*-jet $\Delta\phi$. Measured cross section (black dots) is compared to the POWHEG+PYTHIA NLO+PS prediction (open circles).

Figure 5.43 shows the differential cross section as a function of Z/γ^*-leading jet $\Delta\phi$ in $Z/\gamma^* + \geqslant 1$ jet events. Good agreement is observed both above and below $\Delta\phi = \pi/2$, and a reduced scale uncertainty with respect to the ALPGEN+PYTHIA prediction shown in Figure 5.38. Figure 5.44 shows the measured cross section as a function of leading jet p_T in $Z/\gamma^* + \geqslant 1$ jet events.

5.11 Comparison with NLO QCD ⊗ NLO EW prediction

The virtual part of the NLO electroweak calculation can give significant corrections to the $Z/\gamma^* + 1$ jet differential cross section when high center-of-mass energy is involved. Such condition occurs in the highest p_T bin of leading jet, Z/γ^* and leptons differential distributions, where the NLO electroweak corrections are of the order of 5%. Even with the full dataset collected with the CDF detector in Run II the statistical uncertainty in the high p_T tails of the distributions is about double this value. Nevertheless the $\bar{n}$NLO LOOPSIM+MCFM QCD prediction, nowadays the most accurate, has a theoretical uncertainty of $\sim 5 - 6\%$, dominated by the variation of the renormalization and factorization scale, which is of the same order of the NLO electroweak corrections. For the level of precision of current and future QCD predictions it is therefore necessary to account for electroweak contributions, such corrections are especially important when searching for new physics in the high p_T tails of leptons, Z/γ^* and jets associated to Z boson production.

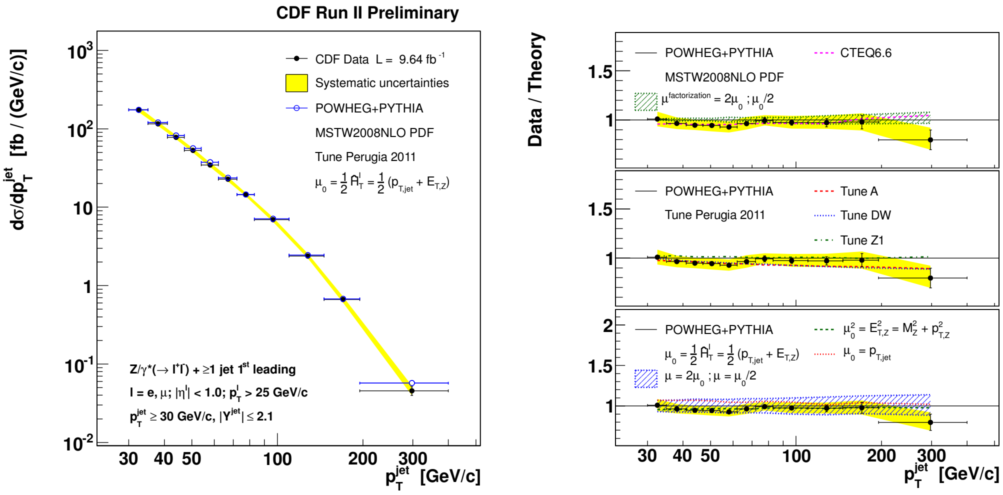

Figure 5.44: $Z/\gamma^* + \geqslant 1$ jets differential cross section as a function of leading jet p_T. Measured cross section (black dots) is compared to the POWHEG+PYTHIA NLO+PS prediction (open circles).

Figures 5.45 and 5.46 show the leading jet p_T and the Z/γ^* p_T for $Z/\gamma^* + \geqslant 1$ jet events. In Figure 5.46 the comparison with the LOOPSIM+MCFM prediction shows that in the last p_T bin the NLO electroweak correction is of the same order of the $\bar{\text{n}}$NLO scale uncertainty.

Figures 5.47 and 5.48 show the leading lepton and second lepton p_T for $Z/\gamma^* + \geqslant 1$ jet events. These differential distributions receive significant contributions both from $\bar{\text{n}}$NLO QCD and from the NLO electroweak corrections.

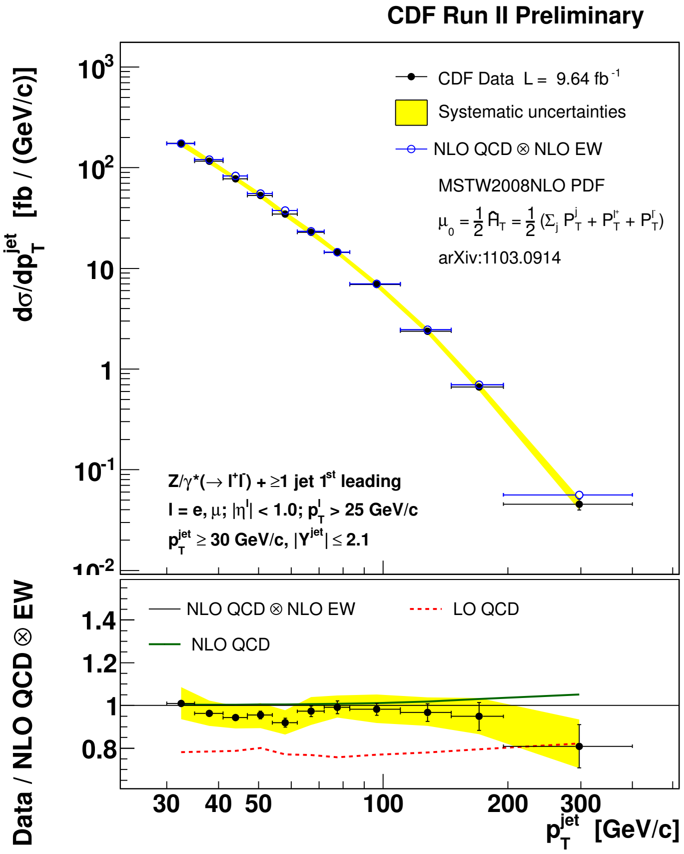

Figure 5.45: Z/γ^* + ⩾ 1 jets differential cross section as a function of leading jet p_T. Measured cross section (black dots) is compared to the NLO QCD ⊗ NLO EW prediction (open circles). The yellow bands show the total systematic uncertainty, except for the 5.8% uncertainty on the luminosity.

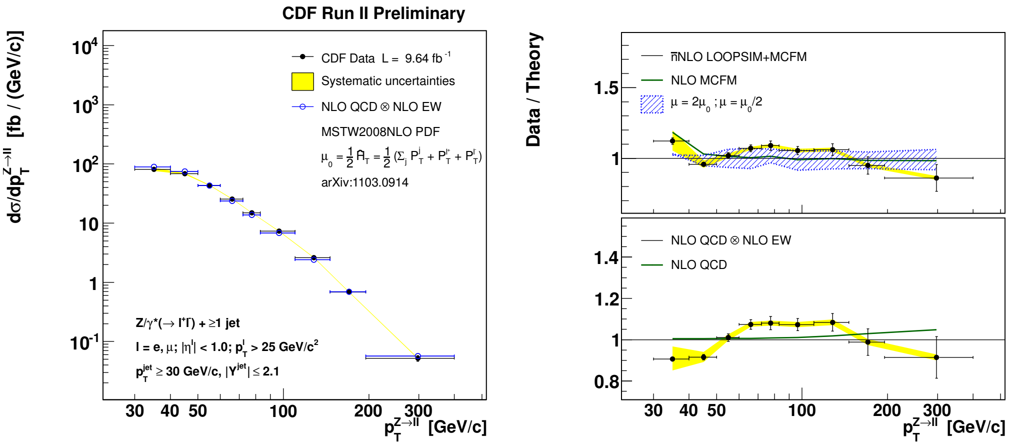

Figure 5.46: $Z/\gamma^* + \geqslant 1$ jets differential cross section as a function of Z/γ^* p_T. Measured cross section (black dots) is compared to the NLO QCD $\otimes$ NLO EW prediction (open circles). Right boxes show data/theory ratio with respect to NLO QCD $\otimes$ NLO EW and LOOPSIM+MCFM predictions, the blue dashed band show the scale uncertainty of the $\bar{n}$NLO LOOPSIM+MCFM prediction.

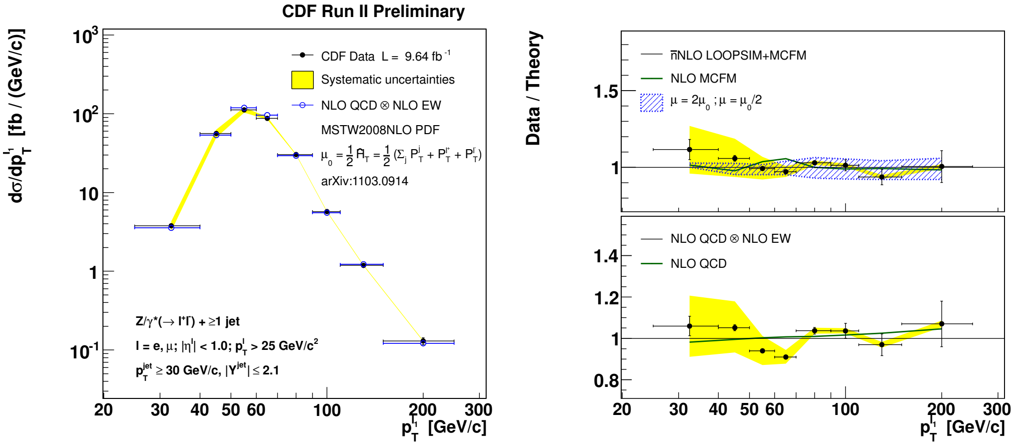

Figure 5.47: $Z/\gamma^* + \geqslant 1$ jets differential cross section as a function of leading lepton p_T. Measured cross section (black dots) is compared to the NLO QCD $\otimes$ NLO EW prediction (open circles).

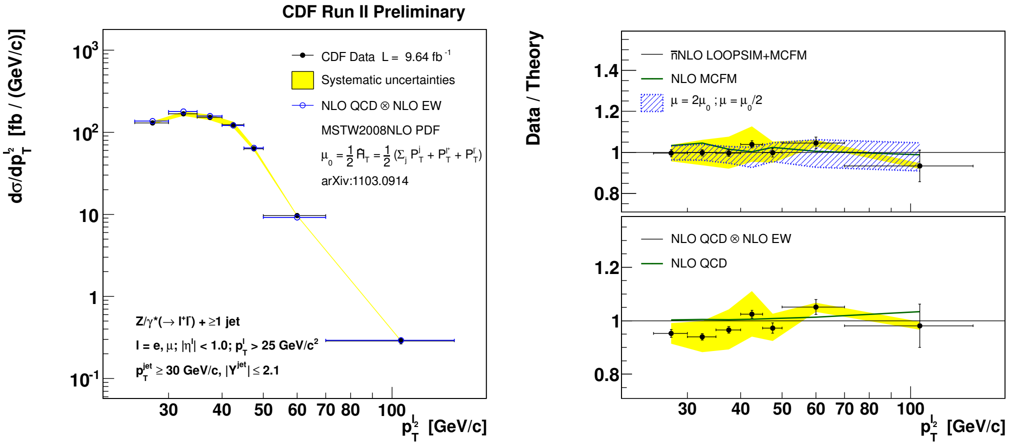

Figure 5.48: $Z/\gamma^* + \geqslant 1$ jets differential cross section as a function of second lepton p_T. Measured cross section (black dots) is compared to the NLO QCD ⊗ NLO EW prediction (open circles).

Chapter 6

Summary and Conclusions

The analysis of about 10 fb^{-1} of integrated luminosity, corresponding to the full dataset collected with the CDF detector in Run II, allows for precise measurement of $Z/\gamma^* +$ jets inclusive and differential cross sections, which constitutes an important legacy of the Tevatron physics program. The understanding of vector boson + jets processes is fundamental in the search for new physics, the results presented in this thesis validate the modeling of $Z/\gamma^* +$ jets currently employed in Higgs and beyond the Standard Model searches.

$Z/\gamma^* \to e^+e^-$ and $Z/\gamma^* \to \mu^+\mu^-$ decay channels are combined to achieve the best experimental precision. Cross sections are unfolded to particle level and measured in the kinematic region $p_T^{\mu} \geqslant 25$ GeV/c, $E_T^{e} \geqslant 25$ GeV/c^2, $|\eta^{l=e,\mu}| \leqslant 1$, $66 \leqslant M_{Z/\gamma^* \to l^+l^-} \leqslant 116$ GeV/c^2, $p_T^{\mathrm{jet}} \geqslant 30$ GeV/c, $|y^{\mathrm{jet}}| \leqslant 2.1|$, with jets reconstructed using the midpoint algorithm in a radius $R = 0.7$.

Results have been compared with most recent theoretical predictions, which properly model the measured differential cross sections in $Z/\gamma^* + \geqslant 1$, 2 and 3 jets final states. The main experimental uncertainty is related to the jet energy scale, while the largest uncertainty of the theoretical predictions is generally associated to the variation of the renormalization and factorization scale.

Among pertubative QCD predictions LOOPSIM+MCFM shows the lowest scale variation uncertainty and is the most accurate prediction for the $Z/\gamma^* + \geqslant 1$ jet final state, while BLACKHAT+SHERPA is the only available prediction with NLO accuracy for the $Z/\gamma^* + \geqslant 3$ jets final state. The ALPGEN+PYTHIA prediction provides a proper modeling of differential distributions in all the jets multiplicity, and is therefore an essential tool for the simulation of $Z/\gamma^* +$ jets processes as a background in searches for new physics; the agreement of ALPGEN+PYTHIA with the measured cross sections has been thoroughly validated. The POWHEG+PYTHIA prediction, thanks to the NLO accuracy of the matrix elements and to the inclusion of non-perturbative QCD effects, provides precise modeling of $Z/\gamma^* + \geqslant 1$ jet final state both in the low and high p_T kinematic regions. The effect of NLO electroweak virtual corrections to the $Z/\gamma^* +$ jet production has been studied and included in the comparison with the measured cross sections, in the high p_T kinematic region corrections are of the order of 5%, which is comparable with the accuracy of beyond NLO predictions.

Improved experimental accuracy is expected from the analysis of data already collected at the LHC experiments. Future developments and improvements of theoretical predictions, in particular the forecoming completion of a NNLO $Z/\gamma^* +$ jet prediction, could provide more accurate theoretical modeling of $Z/\gamma^* +$ jets processes.

Aknowledgements

The circumstances in which I began my personal involvement in Z bosons, jets and other QCD or EW stuff are more related to casualness, or at least to reasons extraneous to physics, than to an a priori interest on the subject. Nevertheless I am grateful to those circumstances and in some ways to life for placing me on an interesting and fruitful path. I would like to thank Matteo Cavalli Sforza for the welcome at IFAE, Mario Martinez for supporting my work, Monica D'Onofrio for supervising the first part of my PhD. Many thanks to Veronica for supervising my thesis and especially for bearing my "last minute" working style. Thanks to Lorenzo for sharing difficulties and "issues", and for being able to deal with my lunatic character. I am grateful to Lance Dixon, Zvi Bern, Gavin Salam, Carlo Oleari, Emanuele Re, Simone Alioli, for useful and interesting discussions, and especially to Sebastian Sapeta, Fernando Febres Cordero and Alexander Mück for their effort in providing predictions for my measurement. The work presented in this thesis was supported by a grant *Formación del Profesorado Universitario (FPU)* of the Spanish *Ministerio de Educación y Cultura*.

A parte de la física muchas personas han contribuido a que cuatro años de mi vida tuviesen el sabor único que tuvieron. Daniela y Rubén con quien he compartido un largo "Erasmus", Margherita que no se como aún me aguanta, todos los socios del Social Club, Garius, Turre, Jennifer, Ronald, Lydie, Guillaume, Jéssica, Bebe, Edu, Esther, Daniel, sin olvidar Hugo, Kay y mucha otra gente que ha pasado por los cuatro muros que el viento fuerte del Eixample azota al cruzar el límite meridional de la Vila de Gracia. Y Leti, que aunque última en llegar no tardó nada en aportar su matiz especial al dibujo.

Mamma e papà non hanno mai smesso di essermi vicino, e Martina mi ha addirittura seguito in alcune delle mie avventure.

Grazie anche a chi è stata la causa contingente che mi ha fatto imbarcare in questo viaggio di cui serberò caro ricordo per gli anni a venire.

Il mio legno
risponde al mare, la mia vela al vento.
Al soffio più lieve, alla minima onda
li sento palpitare
come il mio cuore che tende verso l'alto,
dimentico del porto, senza chiedersi
se la rotta sarà di pace o di tempesta
e senza chiedersi neppure
se vi sarà ritorno.[87]

List of Tables

List of Figures

Bibliography

[1] J. Alcaraz Maestre et al., *The SM and NLO Multileg and SM MC Working Groups: Summary Report*, `arXiv:1203.6803` [hep-ph].

[2] Gavin P. Salam, *Perturbative QCD for the LHC*, `arXiv:1103.1318` [hep-ph].

[3] Mangano, Michelangelo L, *QCD and the physics of hadronic collisions*, *Usp. Fiz. Nauk.* **180** (2010) 113.

[4] Gavin P. Salam, *Elements of QCD for hadron colliders*, `arXiv:1011.5131` [hep-ph].

[5] H. Fritzsch and M. Gell-Mann, *Proceedings of the XVI^{th} International Conference on High energy Physics*, Batavia, IL, Vol. 2, p. 135 (1972); H. Fritzsch, M. Gell-Mann and H. Leutwyler, *Advantages of the Color Octet Gluon Picture*, *Phys. Lett.* **B 47** (1973) 365.

[6] Michael E. Peskin, Daniel V. Schroeder, *An Introduction to Quantum Field Theory*, Westview Press.

[7] Siegfried Bethke, *The 2009 World Average of* α_s, *Eur. Phys. J.* **C 64** (2009) 689, `arXiv:0908.1135` [hepph].

[8] Christian W. Bauer, Bjorn O. Lange, *Scale setting and resummation of logarithms in* $pp \to V + jets$, `arXiv:0905.4739` [hep-ph].

[9] C. F. Berger, Z. Bern, L. J. Dixon, F. Febres Cordero, D. Forde, T. Gleisberg, H. Ita, D. A. Kosower, D. Maitre *Next-to-Leading Order QCD Predictions for W+3-Jet Distributions at Hadron Colliders*, *Phys. Rev.* **D 80**, 074036 (2009), `arXiv:0907.1984` [hep-ph].

[10] C. F. Berger, Z. Bern, L. J. Dixon, F. Febres Cordero, D. Forde, T. Gleisberg, H. Ita, D. A. Kosower, D. Maitre, *Next-to-Leading Order QCD Predictions for* Z,γ^**+3-Jet Distributions at the Tevatron*, *Phys. Rev.* **D 82**, 074002 (2010), `arXiv:1004.1659` [hep-ph].

[11] V. N. Gribov, L. N. Lipatov, *Deep inelastic e p scattering in perturbation theory*, *Sov. J. Nucl. Phys.* **15** (1972) 438; G. Altarelli, G. Parisi, *Asymptotic Freedom in Parton Language*, *Nucl. Phys.* **B 126** (1977) 298; Y. L. Dokshitzer, *Calculation of the Structure Functions for Deep Inealstic Scattering and* e^+e^- *Annihilation by Perturbation Theory in Quantum Chromodynamics*, *Sov. Phys. JETP* **46** (1977) 641;

[12] T. Sjöstrand, *Monte Carlo Generators*, CERN-LCGAPP-2006-06; `hep-ph/0611247`.

[13] R. K. Ellis, W. J. Stirling, B. R. Webber, *QCD and Collider Physics*, Cambridge Monographs on Particle Physics, Nuclear Physics and Cosmology (No. 8) Cambridge University Press (1996).

[14] Gavin P. Salam, *Towards Jetography*, `arXiv:0906.1833v2` [hep-ph].

[15] Gavin P. Salam, Gregory Soyez, *A practical Seedless Infrared-Safe Cone jet algorithm*, *J. High Energy Phys.* **0705** (2007) 086, `arXiv:0704.0292` [hep-ph].

[16] J. E. Huth, et al., *Toward a standardization of jet definitions*, Published in Snowmass 1990, Proceedings, Research directions for the decade, FERMILAB-CONF-90-249-E.

[17] J.H. Kuhn, A. Kulesza, S. Pozzorini, M. Schulze, *One-loop weak corrections to hadronic production of Z bosons at large transverse momenta*, *Nucl. Phys.* **B 727** (2005) 368, [`hep-ph/0507178`].

[18] Ansgar Denner, Stefan Dittmaier, Tobias Kasprzik, Alexander Mück, *Electroweak corrections to dilepton + jet production at hadron colliders*, *J. High Energy Phys.* **1106** (2011) 069, `arXiv:1103.0914` [hep-ph].

[19] John Campbell, R. K. Ellis, *Next-to-leading order corrections to W+2 jet and Z+2 jet production at hadron colliders*, *Phys. Rev.* **D 65**, 113007 (2002), [`hep-ph/0202176`].

[20] The CDF Collaboration, *Measurement of Inclusive Jet Cross Sections in Z/g* (→ ee)+jets Production in ppbar Collisions at* $\sqrt{s} = 1.96$ *TeV*, *Phys. Rev. Lett.* **100** (2008) 102001, `arXiv:0711.3717` [hep-ex].

[21] The D0 Collaboration, *Measurements of differential cross sections of* Z/γ^**+jets+X events in proton anti-proton collisions at* $\sqrt{s} = 1.96$ *TeV*, *Phys. Lett.* **B 678** (2009) 45, `arXiv:0903.1748` [hep-ex].

[22] H. Ita, Z. Bern, L. J. Dixon, F. Febres Cordero, D. A. Kosower, D. Maitre, *Precise Predictions for Z + 4 Jets at Hadron Colliders*, `arXiv:1108.2229` [hep-ph].

[23] Z. Bern, L. Dixon, D.C. Dunbar, D.A. Kosower, *One-Loop n-Point Gauge Theory Amplitudes, Unitarity and Collinear Limits*, *Nucl. Phys.* **B 425** (1994) 217, [`hep-ph/9403226`].

[24] T. Gleisberg, S. Hoeche, F. Krauss, M. Schoenherr, S. Schumann, F. Siegert, J. Winter, *Event generation with SHERPA 1.1*, *J. High Energy Phys.* **0902** (2009) 007, `arXiv:0811.4622` [hep-ph].

[25] E. W. N. Glover, Joao Pires, *Antenna subtraction for gluon scattering at NNLO*, *J. High Energy Phys.* **1006** (2010) 096, `arXiv:1003.2824` [hep-ph]; Aude Gehrmann-De Ridder, E. W. N. Glover, Joao Pires, *Real-Virtual corrections for gluon scattering at NNLO*, *J. High Energy Phys.* **1202** (2012) 141, `arXiv:1112.3613` [hep-ph].

[26] Thomas Becher, Christian Lorentzen, Matthew D. Schwartz, *Resummation for W and Z production at large pT*, *Phys. Rev. Lett.* **108** (2012) 012001, `arXiv:1106.4310` [hep-ph].

[27] Nikolaos Kidonakis, Richard J. Gonsalves, *Two-loop corrections to W and Z boson production at high pT*, `arXiv:1109.2817` [hep-ph].

[28] Mathieu Rubin, Gavin P. Salam, Sebastian Sapeta, *Giant QCD K-factors beyond NLO*, *J. High Energy Phys.* **1009** (2010) 084, `arXiv:1006.2144` [hep-ph].

[29] T. Sjöstrand, L. Lönnblad, S. Mrenna, *PYTHIA 6.2 Physics and Manual*, LU TP 01-21, [`hep-ph/0108264`]; T. Sjöstrand, S. Mrenna, P. Skands, *PYTHIA 6.4 Physics and Manual*, *J. High Energy Phys.* **0605** (2006) 026, [`hep-ph/0603175`].

[30] Rick Field, R. Craig Group, *Pythia Tune A, Herwig, and Jimmy in Run 2 at CDF*, `hep-ph/0510198`.

[31] P. Z. Skands, *Tuning Monte Carlo Generators: The Perugia Tunes*, *Phys. Rev.* **D 82**, 074018 (2010), `arXiv:1005.3457` [hep-ph].

[32] R. Field, *CDF Run 2 Monte-Carlo Tunes*, FERMILAB-PUB-06-408-E; The CDF Collaboration, *Studying the Underlying Event in Drell-Yan and High Transverse Momentum Jet Production at the Tevatron*, *Phys. Rev.* **D 82**, 034001 (2010), `arXiv:1003.3146` [hep-ex].

[33] T. Sjöstrand, P. Skands, *Transverse-Momentum-Ordered Showers and Interleaved Multiple Interactions*, *Eur. Phys. J.* **C 39** (2005) 129, [`hep-ph/0408302`].

[34] B.Cooper, J.Katzy, M.L.Mangano, A.Messina, L.Mijovic, P.Skands, *Monte Carlo tuning in the presence of Matching*, CERN-PH-TH/2011-228, DESY 11-124, `arXiv:1109.5295` [hep-ph].

[35] M.L. Mangano, M. Moretti, F. Piccinini, R. Pittau, A.D. Polosa, *ALPGEN, a generator for hard multiparton processes in hadronic collisions*, *J. High Energy Phys.* **0307** (2003) 001, [`hep-ph/0206293`].

[36] F. Caravaglios, M.L. Mangano, M. Moretti, R. Pittau, *A New approach to multijet calculations in hadron collisions*, *Nucl. Phys.* **B 539** (1999) 215, `hep-ph/9807570`.

[37] Michelangelo L. Mangano, Mauro Moretti, Roberto Pittau, *Multijet matrix elements and shower evolution in hadronic collisions: W b bbar + n jets as a case study*, *Nucl. Phys.* **B 632** (2002) 343, `hep-ph/0108069`; J. Alwall et al., *Comparative study of various algorithms for the merging of parton showers and matrix elements in hadronic collisions*, *Eur. Phys. J.* **C 53** (2008) 473, `arXiv:0706.2569` [hep-ph].

[38] S. Frixione, P. Nason and C. Oleari, *Matching NLO QCD computations with Parton Shower simulations: the POWHEG method*, *J. High Energy Phys.* **0711** (2007) 070, `arXiv:0709.2092` [hep-ph].

[39] S. Alioli, P. Nason, C. Oleari and E. Re, *Vector boson plus one jet production in POWHEG*, *J. High Energy Phys.* **1101** (011) 095, `arXiv:1009.5594` [hep-ph].

[40] Frank Krauss, Andreas Schaelicke, Steffen Schumann, Gerhard Soff, *Simulating W/Z+jets production at the Tevatron*, `hep-ph/0409106`, *Phys. Rev.* **D 70**, 114009 (2004);

[41] S. Frixione, B.R. Webber, *Matching NLO QCD computations and parton shower simulations*, *J. High Energy Phys.* **0206** (2002) 029, `hep-ph/0204244`.

[42] Jeppe R. Andersen, Jennifer M. Smillie, *Constructing All-Order Corrections to Multi-Jet Rates*, *J. High Energy Phys.* **1001** (2010) 039, `arXiv:0908.2786` [hep-ph]; *Multiple Jets at the LHC with High Energy Jets*, *J. High Energy Phys.* **1106** (2011) 010, `arXiv:1101.5394` [hep-ph].

[43] Keith Hamilton, Paolo Nason, *Improving NLO-parton shower matched simulations with higher order matrix elements*, *J. High Energy Phys.* **1006** (2010) 039, `arXiv:1004.1764` [hep-ph].

[44] Stefan Hoeche, Frank Krauss, Marek Schonherr, Frank Siegert, *NLO matrix elements and truncated showers*, `arXiv:1009.1127` [hep-ph].

[45] Simone Pagan Griso, *Searches for a High mass Higgs boson produced in* $p\bar{p}$ *collisions at* $\sqrt{s} = 1.96$ *TeV*, FERMILAB-THESIS-2010-62.

[46] Fermilab, *Accelerator Concepts*, 2010, `http://www-bdnew.fnal.gov/operations/rookie_books/Concepts_v3.6.pdf`.

[47] The CDF Collaboration, *CDF Run II: Technical Design Report*, FERMILAB-PUB-96-390-E (1996).

[48] Fermilab, *Run II Handbook*, 2003, `http://www-ad.fnal.gov/runII/index.html`.

[49] F. B. Division, *The Linac rookie book*, 2012, `http://www-bdnew.fnal.gov/operations/rookie_books/LINAC_RB_v2_3.pdf`.

[50] F. B. Division, *The Booster rookie book*, 2009, `http://www-bdnew.fnal.gov/operations/rookie_books/Booster_V4.1.pdf`.

[51] F. B. Division, *The Main Injector rookie book*, 2010, `http://www-bdnew.fnal.gov/operations/rookie_books/Main_Injector_v1.1.pdf`.

[52] F. B. Division, *The Antiproton Source rookie book*, 2011, `http://www-bdnew.fnal.gov/operations/rookie_books/Pbar_v2.2.pdf`.

[53] F. B. Division, *The Recycler Injector rookie book*, 2010, `http://www-bdnew.fnal.gov/operations/rookie_books/Recycler_RB_v1.42.pdf`.

[54] F. B. Division, *The Tevatron rookie book*, 2009, `http://www-bdnew.fnal.gov/operations/rookie_books/Tevatron_v2.3.pdf`.

[55] A. Sill for the CDF collaboration, *CDF Run II Silicon Tracking Projects*, *Nucl. Instrum. Meth.* **A447** (2000) 1.

[56] T. Affolder et al., *Central Outer Tracker*, *Nucl. Instrum. Meth.* **A526** (2004) 249.

[57] A. Artikov et al., *Design and construction of new central and forward muon counters for CDF II*, *Nucl. Instrum. Meth.* **A538** (2005) 358, [`physics/0403079`].

[58] D. Acosta et al., *The CDF Cherenkov luminosity monitor*, *Nucl. Instrum. Meth.* **A461** (2001) 540.

[59] F. Abe et al. *Measurement of the antiproton-proton total cross section at* $\sqrt{s} = 546$ *and 1800 GeV*, *Phys. Rev.* **D 50**, 5550 (1993).

[60] S. Klimenko, J. Konigsberg and T. Liss, *Averaging of the Inelastic Cross Sections Measured by the CDF and the E811 Experiments*, FERMILAB-FN-0741 (2003).

[61] G.C. Blazey et al., *Run II Jet Physics: Proceedings of the Run II QCD and Weak Boson Physics Workshop*, [`hep-ex/0005012`].

[62] S.D. Ellis, J. Huston, M. Toennesmann, *On Building Better Cone Jet Algorithms*, eConf C010630 (2001) P513, [`hep-ph/0111434`].

[63] A. Bhatti *et al*, *Determination of the jet energy scale at the Collider Detector at Fermilab*, *Nucl. Instrum. Meth.* **A566** (2006) 375, [`hep-ex/0510047`].

[64] Guenter Grindhammer, M. Rudowicz, S. Peters, *The Fast Simulation Of Electromagnetic And Hadronic Showers*, *Nucl. Instrum. Meth.* **A290** (1990) 469.

[65] G.Corcella, I.G.Knowles, G.Marchesini, S.Moretti, K.Odagiri, P.Richardson, M.H.Seymour, B.R.Webber, *HERWIG 6.5: an event generator for Hadron Emission Reactions With Interfering Gluons (including supersymmetric processes)*, *J. High Energy Phys.* **0101** (2001) 010, `hep-ph/0011363`.

[66] R. Brun, et al., *GEANT: Simulation program for particle physics experiments. User guide and reference manual*, CERN-DD-78-2-REV (1978); *GEANT: Detector description and simulation tool*, Cern Program Library Long Writeup W5013, (1993).

[67] A.D. Martin, W.J. Stirling, R.S. Thorne, G. Watt, *Parton distributions for the LHC*, *Eur. Phys. J.* **C 63** (2005) 189, `arXiv:0901.0002` [hep-ph].

[68] H.L. Lai et al, *Global QCD Analysis of Parton Structure of the Nucleon: CTEQ5 Parton Distributions*, *Eur. Phys. J.* **C 12** (2000) 375, [`hep-ph/9903282`].

[69] O. Saltó, *Measurement of Inclusive Jet Cross Sections in* Z/γ $(\rightarrow e{+}e)$ *+ jets Production in* $\mathrm{p\bar{p}}$ *Collisions at* $\sqrt{s} = 1.96$ *TeV with the CDF Detector*, Ph.D. Thesis, U.A.B., Barcelona (2008), FERMILAB-THESIS-2008-17.

[70] Mrinal Dasgupta, Lorenzo Magnea, Gavin P. Salam, *Non-perturbative QCD effects in jets at hadron colliders*, *J. High Energy Phys.* **0802** (2008) 055, `arXiv:0712.3014` [hep-ph].

[71] The CDF Collaboration, *First Measurements of Inclusive W and Z Cross Sections from Run II of the Tevatron Collider*, *Phys. Rev. Lett.* **94** (2005) 091803, `hep-ex/0406078`; The CDF Collaboration, *Measurements of Inclusive W and Z Cross Sections in p-pbar Collisions at* $\sqrt{s} = 1.96$ *TeV*, *J. Phys.* **G 34** (2007) 2457, `hep-ex/0508029`.

[72] C. Buttar et al., *Standard Model Handles and Candles Working Group: Tools and Jets Summary Report*, `arXiv:0803.0678` [hep-ph].

[73] L. Lyons, D. Gibaut and P. Clifford, *How To Combine Correlated Estimates Of A Single Physical Quantity*, *Nucl. Instrum. Meth.* **A270** (1988) 110.

[74] The CDF Collaboration, *Measurement of the Single Top Quark Production Cross Section at CDF*, *Phys. Rev. Lett.* **101** (2008) 252001, `arXiv:0809.2581` [hep-ex].

[75] The D0 Collaboration, *Double parton interactions in photon+3 jet events in ppbar collisions sqrts=1.96 TeV*, *Phys. Rev.* **D 81**, 052012 (2010), `arXiv:0912.5104` [hep-ex].

[76] J. Pumplin, D. Stump, R. Brock, D. Casey, J. Huston, J. Kalk, H.L. Lai, W.K. Tung, *Uncertainties of predictions from parton distribution functions II: the Hessian method*, *Phys. Rev.* **D 65**, 2001 (014013), [`hep-ph/0101032v3`].

[77] P. M. Nadolsky, H.-L. Lai, Q.-H. Cao, J. Huston, J. Pumplin, D. Stump, W.-K. Tung, C.-P. Yuan, *Implications of CTEQ global analysis for collider observables*, *Phys. Rev.* **D 78**, 013004 (2008), `arXiv:0802.0007` [hep-ph].

[78] Richard D. Ball, Valerio Bertone, Francesco Cerutti, Luigi Del Debbio, Stefano Forte, Alberto Guffanti, Jose I. Latorre, Juan Rojo, Maria Ubiali, *Impact of Heavy Quark Masses on Parton Distributions and LHC Phenomenology*, *Nucl. Phys.* **B 849** (2011) 296, `arXiv:1101.1300` [hep-ph].

[79] Hung-Liang Lai, Marco Guzzi, Joey Huston, Zhao Li, Pavel M. Nadolsky, Jon Pumplin, C.-P. Yuan, *New parton distributions for collider physics*, *Phys. Rev.* **D 82**, 074024 (2010), `arXiv:1007.2241` [hep-ph].

[80] A.D. Martin, R.G. Roberts, W.J. Stirling, R.S. Thorne, *MRST2001: partons and* $alpha_S$ *from precise deep inelastic scattering and Tevatron jet data*, *Eur. Phys. J.* **C 23** (2002) 73, `hep-ph/0110215`.

[81] M.R.Whalley, D.Bourilkov, R.C.Group, *The Les Houches Accord PDFs (LHAPDF) and Lhaglue*, `hep-ph/0508110`.

[82] Matteo Cacciari, Gavin P. Salam, Gregory Soyez, *FastJet user manual*, CERN-PH-TH/2011-297, `arXiv:1111.6097` [hep-ph].

[83] Ryan Gavin, Maike K. Trenkel, *SUSY QCD corrections to electroweak gauge boson production with an associated jet at the LHC*, *J. High Energy Phys.* **1201** (036) 2012, `arXiv:1109.3445` [hep-ph]

[84] J. Pumplin, D.R. Stump, J. Huston, H.L. Lai, P. Nadolsky, W.K. Tung, *New Generation of Parton Distributions with Uncertainties from Global QCD Analysis*, *J. High Energy Phys.* **0207** (2002) 012, `hep-ph/0201195`.

[85] The ATLAS Collaboration, *Measurement of the production cross section for Z/gamma* in association with jets in pp collisions at sqrt(s) = 7 TeV with the ATLAS detector*, *Phys. Rev.* **D 85**, 032009 (2012), `arXiv:1111.2690` [hep-ex].

[86] The D0 Collaboration, *Measurements of inclusive W+jets production rates as a function of jet transverse momentum in ppbar collisions at* $\sqrt{s} = 1.96$ *TeV*, *Phys. Lett.* **B 705** (2011) 200, `arXiv:1106.1457v2` [hep-ex].

[87] M. Guidacci *Il mio legno risponde al mare*, in *Inno alla gioia*, p.48 Centro Internazionale del Libro, Firenze 1983